ELECTRICAL DETECTION OF SPIN-ORBIT TORQUE IN ANTIFERROMAGNETS

by
Cemal İlkin Göksal
B.Sc., Physics Engineering, Istanbul Technical University, 2018

Submitted to the Institute for Graduate Studies in
Science and Engineering in partial fulfillment of
the requirements for the degree of
Master of Science

Graduate Program in Master of Science in Physics
Boğaziçi University
2022

ACKNOWLEDGEMENTS

I would like to start with mentioning how grateful I am to Prof. Ozhan Ozatay, for giving me this life changing opportunity and teaching me the art of learning from mistakes. His point of views, way of thinking and advising personality have become something that I will proudly carry through all my life. BUSPIN was the game changer of my academic life, and where ever I land, it will always remain as my home,where I learnt baby steps of science.

I would like to thank Can Koscaz, Ilmar Gahramanov, Hakan Erkol, Levent Akant and Ersan Demiralp for their efforts of teaching me physics and helping out for various kind of troubles I have faced during my studies. I would like to thank also Dr. Yılmaz Şimşek and Dr. Başak Kayıtmazer for becoming by jury for thesis defense. I want to thank TUBITAK for its support under contract number 118F116, Boğaziçi University Research Fund Grant (BAP) under contract number 12420 and Sabancı University for allowing us use their cleanroom facilities in Nanotechnology Research and Application Center for making my research activities possible and feasible during extraordinary times.

During this period, words are not enough to describe how supportive my lab mates were, I am so glad that I can show my gratitude to Ege, Koral, Doğukan, Enes, Bayram, Kutay, Emre and previous members of BUSPIN for their efforts to create such an environment and culture.

From the first day of this project, Dr. Hasan Pişkin was the one who thought nearly everything that I practically perform in lab, answer my questions patiently, fixing the problems I face in lab, but most importantly share his dearest friendship with me all the way to here. I would be stuck somewhere in half of it if he wasn't there for me. His presence and efforts were priceless, so that I can't even express how important he was both for me and this thesis to be written. I will never forget what a ride we had in this two years and will always try to be a helpful and trustworthy superior like you after my PhD.

All the way from high school,through ITU, now BUSPIN and further to my PhD period, I was incredibly lucky to have my friends supporting and motivating me no matter how hard times I've been through. Can't thank enough Mert, Ozan, Müjdat, Anıl TT, Çakmak brothers, Hazar, Taylan, Ismail, my band mates in stage and in real life Cihan, Burak and Ender, Simge & Şevval and many more I am not able to fit in one paragraph. I also want to thank Elifsu, making the hardest part, homestretch for completing this thesis transform into best time of my life. It wouldn't be same without you.

Most importantly, anything I achieved and succeeded may have my signature on it. But the makers of this stories and making me able to put that signature on them are no one but Nilgün and Erhan Göksal, my parents, my best friends and my companions through this tough path I have chosen in life. There wasn't even one moment that they haven't put their trust on me, even when I was not confident. I know that the only way I can pay their efforts back is becoming a better scientist. I will do my best for this purpose in the future.

ABSTRACT

ELECTRICAL DETECTION OF SPIN-ORBIT TORQUE IN ANTIFERROMAGNETS

Ferromagnetic spintronics has been a game changer for memory technologies, until it has been understood that at some point ferromagnetic properties of these devices won't be able to compensate for the demand on volume and performance. At this point, antiferromagnetic (AFM) spintronics emerged as the most promising alternative and this accelerated the research and investment on AFM spintronics. AFM materials are known with their magnetic toughness due to zero net magnetization in bulk and promising bit per volume ratio thanks to their two spin lattices pointing in opposite directions.

In this study, our aim is to achieve current induced manipulation of antiferromagnetic moments. Though there are multiple suggested ways for AFM magnetization manipulation, we study DC electrical transport experiments where by we utilize spin-orbit torque (SOT) effect on metallic AFM materials ($IrMn_4$,$IrMn_3FeMn$). The underlying mechanism for spin manipulation is a mixture of Spin Hall Effect (SHE) and interfacial Rashba effect (IRE). We start our investigation with bi-layers of high SOC heavy metals (Pt,Ta) and AFM metal($IrMn_4$,FeMn) hetero structures of [HM/AFM].

Following these experiments, we also investigate the cumulative properties of SOT effect by demonstrating DC electrical transport experiments on HM/AFM/HM trilayer hetero structures and stacks of [HM/AFM/HM] $\times$ n, (where n=2,3,4 etc.). These results will help to improve understanding of the nature of electrical manipulation of AFM spin and determine the conditions to use them as spintronic devices.

ÖZET

ANTİFERROMANYETİK MALZEMELERDE SPİN-YÖRÜNGE TORKUNUN ELEKTRİKSEL ÖLÇÜMLERLE GÖZLENMESİ

Yeni nesil manyetik bilgi işleme teknolojilerinden olan Ferromanyetik malzeme temelli spintronik cihazlar hafıza cihazlarında uzun bir süre oldukça kritik bir rol oynadı ve ihtiyaçları karşıladı. Ancak hızla artan hacim ve performans gereksinimleri bir noktada ferromanyetik yapıların sınırlarını zorlamaya başladı. Bu noktada antiferromagnetler güncel cihazlardaki bu sorunları çözmek için en önemli aday olarak görülmektedir. Antiferromanyetik (AFM) malzemelerin zıt yönlü spin örgüsü, malzemenin net manyetizasyonunu yok etmesi sayesinde dışarıdan uygulanan manyetik alanlara karşı oldukça dayanıklı olması bu malzemeleri potansiyel cihaz teknolojileri için kaçınılmaz bir aday kılmaktadır.

Çalışmamızda AFM cihazlar için manyetik momentlerin DC elektrik akımı kullanılarak manipüle edilmesi ve bunun için kullanılabilecek farklı fiziksel mekanizmalar araştırılmıştır. AFM momentlerin manipüle edilmesi için önerilen birden fazla yöntem olmakla birlikte, bu çalışmada spin-yörünge torku (SOT) kullanılarak elektriksel manipülasyon mekanizması üzerine çalışılmıştır. Bu noktada SOT oluşumu yüksek spin-yörünge etkileşimli ağır metaller (Pt, Ta) kullanılarak elde edilmiştir. Yüksek spin-yörünge etkileşimli(SOC) ağır metal tabakaları(HM) kullanılarak oluşturulan etkide tetikleme mekanizmaları spin Hall etkisi (SHE) ve ara yüzeysel Rashba etkisi (IRE) olup, bu etkilerin AFM yapılarda (IrMn,FeMn) oluşturduğu manyetik manipülasyon araştırılmıştır. İlk olarak bu etkinin fiziksel özelliklerini ve limitlerini test edebilmek adına ikili yapı halinde HM/AFM elektriksel taşınım ölçümleri yapılmış olup, buradan aldığımız donelerle HM/AFM/HM üçlü yapı deneyleri ve [HM/AFM/HM] $\times$ n (n=2,3,4..) çoklu yapı deneyleriyle bu etkinin toplanabilirlik özellikleri araştırılmıştır.

TABLE OF CONTENTS

ACKNOWLEDGEMENTS . . . iii
ABSTRACT . . . v
ÖZET . . . vi
LIST OF FIGURES . . . ix
LIST OF TABLES . . . xvii
LIST OF SYMBOLS . . . xviii
LIST OF ACRONYMS/ABBREVIATIONS . . . xix
1. INTRODUCTION . . . 1
2. ANTIFERROMAGNETIC SPINTRONICS . . . 5
2.1. Introduction to Antiferromagnets . . . 5
2.1.1. History of Antiferromagnets . . . 6
2.1.2. Characterization of Antiferromagnets . . . 7
2.1.2.1. Neutron Scattering . . . 7
2.2. Magnetic Manipulation of Antiferromagnets . . . 10
2.2.1. Anisotropic Magnetoresistance . . . 11
2.2.2. Manipulation with Magnetic Field . . . 12
2.2.3. Spin-Orbit Coupling . . . 13
2.2.4. Spin Hall Effect & Rashba Effect . . . 14
2.2.4.1. Spin Hall Effect . . . 15
2.2.4.2. Rashba & Edelstein Effect . . . 17
2.2.5. Spin-Orbit Torque . . . 18
2.2.6. Detection of Spin-Orbit Torque . . . 22
2.2.6.1. Non-Local Spin Valve . . . 22
2.2.6.2. DC Current Switching . . . 23
3. FABRICATION TECHNIQUES . . . 25
3.1. Photolithography . . . 25
3.1.1. Hall Bar Fabrication . . . 25
3.1.2. Contact Fabrication . . . 27
3.2. Chemical Procedures . . . 29
3.2.1. Lift-Off . . . 29
3.2.1.1. First Lift-Off . . . 29
3.2.1.2. Second Lift-Off . . . 29

3.2.2. GeVarnish Procedure 30
3.3. Magnetron Sputtering 30
3.4. E-Beam Evaporation 32
4. MATERIAL CHARACTERIZATIONS 34
4.1. Deposition Rate Calibrations 34
4.1.1. Thickness Calibrations 34
4.1.2. Roughnes Characterizations 36
4.1.3. XRD Measurements 39
4.2. Magnetic Characterizations 44
4.3. Resistivity Measurements 48
4.4. Electro-Resistance Measurements 50
4.4.1. Important Points of Electro-resistance Measurements 53
4.4.1.1. Compliance Problem 53
4.4.1.2. Exact Current Applied from Source 53
4.4.1.3. Heating of Sample 53
4.4.1.4. Preventing Electrical Spikes 55
5. EXPERIMENTS AND RESULTS 56
5.1. Experiments on Bilayer Structures 58
5.1.1. $Fe_{50}Mn_{50}$ Bilayer Experiments 59
5.1.2. $IrMn_4$ Bilayer Experiments 60
5.1.2.1. Pt/$IrMn_4$ Experiments 60
5.1.2.2. Ta/$IrMn_4$ Experiments 63
5.2. Experiments on Trilayer Structures 65
5.2.1. $Fe_{50}Mn_{50}$ Trilayer Experiments 66
5.2.2. $IrMn_4$ Trilayer Experiments 68
5.3. Multistack Experiments 70
5.3.1. FeMn Multistack Experiments 71
5.3.2. $IrMn_4$ Multistack Experiments 73
6. CONCLUSION AND DISCUSSION 75
REFERENCES 86

LIST OF FIGURES

Figure 1.1. The response of ferromagnetic ordered spins work to an external magnetic field. 2

Figure 1.2. The response of antiferromagnetic ordered spins work to an external magnetic field. 3

Figure 1.3. Working principle of an STT structure in FM. 4

Figure 2.1. Neutron beams being scattered when two magnetic moments are one under other, single type of magnetic lattices, which occurs when MnO is over critical temperature. 8

Figure 2.2. Regular scattering mechanism for a single lattice system. 8

Figure 2.3. Scattering mechanism of a two spin sub-lattice system. 9

Figure 2.4. Neutron diffraction data for MnO, up is 80 K, down side is room temperature 9

Figure 2.5. Neutron diffraction data for MnO, up is 80 K, down side is room temperature. 10

Figure 2.6. Detection of anisotropic magnetoresistance behaviour occuring in FeRh sample 11

Figure 2.7. Schematic of how spin-orbit interaction takes place in orbital electrons. 14

Figure 2.8. Illustration for the some of the members of Hall effect family. From top to bottom; ordinary Hall effect, anomalous Hall effect, spin Hall effect. 16

Figure 2.9. Comparing ISHE properties of $IrMn_4$ and Pt shows $IrMn_4$ can be used as a pure spin current source in an AFM spin lattice. 17

Figure 2.10. Illustration of applied torques on magnetic moment, induced by current in a FM/HM structure. 19

Figure 2.11. Schematic comparison of inducing SOT on a ferromagnet by using (a) spin Hall effect, (b) Rashba effect. 20

Figure 2.12. Anatomy of spin Hall effect induced spin-orbit torque on Heavy Metal/Antiferromagnet bilayers. (a) If the antiferromagnetic order is in-plane. (b) If the antiferromagnetic order is out of plane. . . 21

Figure 2.13. Expected physical mechanism of a sandwich structure. 21

Figure 2.14. (a) SEM image combined with illustration of non-local spin valve mechanism, (b) SHE and ISHE measurements performed with given device. 23

Figure 2.15. (a) Schematic of the DC current switching device. (b) Resistance against field in long axis. Inset data belongs to magnetic major loop of device. (c) Resistance behaviour against applied current to MTJ. (d) Switching currents as a function of ramping rates. . . . 24

Figure 3.1. Hall Bar mask design in Layout Editor. First picture shows bars with different widths, second picture shows arrays of bars. 26

Figure 3.2. Illustration of Hall bar patterns after first lithography step. . . . 27

Figure 3.3. Result of contact lithography. 28

Figure 3.4. First Lift off process (a) before deposition of metallic films, (b) after deposition of metallic films, (c) after first lift-off. 30

Figure 3.5. Magnetron sputtering mechanism. Black dots represent Ar atoms, red dots present metallic atoms, small blue dots present electrons. 31

Figure 3.6. Schematic for an example usage of e-beam evaporation technique. 32

Figure 3.7. Picture and microscope image of samples after Cr & Au evaporation. 33

Figure 4.1. Sputtering rate measurement procedure. From left to right, one single calibration grating, and partial images of gratings to be measured. 35

Figure 4.2. Atomic force microscopy data from Pt thin film roughness measurements. 37

Figure 4.3. Atomic force microscopy data for roughness measurements from top to bottom; Ta, FeMn, IrMn. 38

Figure 4.4. Si/SiO_2 substrate samples for XRD investigation. 40

Figure 4.5. Bragg rule and the working principle of XRD. X-rays create constructive interference only when Bragg law is satisfied,where n is the number of atoms, d is the lattice constant and θ is the incoming angle. 40

Figure 4.6. Si/SiO_2 substrate samples XRD results; orange data belongs to sample prepared with magnetic stage, on Pt layer. Blue data shows IrMn sputtered on 5 nm Ti layer with magnetic stage. Green data shows IrMn sputtered on 5 nm Ti layer without magnetic field. . 41

Figure 4.7. MgO substrate samples XRD results; green data shows $MgO/IrMn_3$ sample, orange data shows only MgO(100) XRD measurements. . 42

Figure 4.8. $IrMn_3$ deposition on different substrates. (a) MgO (002), (b) R cut Al_2O_3, (c) M cut Al_2O_3, (d) Si/SiO_2 42

Figure 4.9. $IrMn_3$ XRD data on different substrates. (a) Amorphous Si/SiO_2, (b) M-cut Al_2O_3, (c) R cut Al_2O_3 43

Figure 4.10. Samples prepared for VSM measurements. 44

Figure 4.11. VSM measurements with reference 5 nm $Ni_{81}Fe_{19}$ layer. (a)Hysteresis in room temperature, (b)hysteresis behaviours in different temperatures. 46

Figure 4.12. VSM measurement for $Ni_{81}Fe_{19}/IrMn_4$ stack. (a) Magnetization versus applied field hysteresis at 50 K (b) The same data for changing temperature (c) H_C and H_{Ex} values for each temperature for $Ni_{81}Fe_{19}(5)/IrMn_4(15)$. 47

Figure 4.13. VSM measurement for $Ni_{81}Fe_{19}$ (5)/FeMn stack. (a) Magnetization versus applied field hysteresis at 50 K (b) The same data for with changing temperature (c)H_C and H_{Ex} values for each temperature for $Ni_{81}Fe_{19}(5)$/FeMn (15). 47

Figure 4.14. VSM results overview. (a) blocking temperatures for different thicknesses of FeMn (b) blocking temperatures for different thicknesses of $IrMn_4$ (c) changes in H_C and H_{Ex} of FeMn samples (d) H_C and H_{Ex} of $IrMn_4$ samples in an alternative representation. 48

Figure 4.15. JANIS low temperature measurement system from different views; (a) JANIS cryostat. (b) Holder for inserting sample inside. (c) Electrical connections and pressure screen. (d) PCB insertion for measurements. 49

Figure 4.16. Resistivity measurement for Pt, red data for 10 nm and blue data for 50 nm. 49

Figure 4.17. Resistivity measurement for Ta,Ti,FeMn and $IrMn_4$ red data for 10 nm and blue data for 50 nm. 50

Figure 4.18. Three different cases of field cooling the Hall bars. (a) Parallel to the injected current. (b) In-plane perpendicular to injected current. (c) Out-of-plane perpendicular to injected current. 51

Figure 4.19. Rotator system elements. (a) Rotator bar. b)Mounting in-plane PCB on rotator. (c) Controlling head of rotator with rotating angle adjustment. (d) Sample on out-of-plane PCB. (e) In-plane sample mounted on rotator. (f) LEMO power plugs. 52

Figure 4.20. Schematic drawings of a cut prism to inject current. h is the height, L is the longitudinal length and w is the width. A is the area of surface that a current to be injected into. 54

Figure 4.21. Make-before-break switch. Two rotary switches are used, first one is for voltage drop, second one is for creating short and disabling the current. 55

Figure 5.1. Comparative study on HM/AFM bilayer for (a) Pt as HM layer with high-SOC, (b) Al as HM layer with low-SOC on $Fe_{50}Mn_{50}$. AFM layer shows the differences in current scan trends. (c) Schematics for field cooling process. 56

Figure 5.2. (a) Resistance versus temperature behaviour of two samples in the interval of field cooling process. (b) Current scan at the upper limit of field cooling process, in order to compare the trend to low temperature field cooling trends. 57

Figure 5.3. Schematic of bilayer structures of (a) and (b) $IrMn_4$, (c) and (d) $Fe_{50}Mn_{50}$. 58

Figure 5.4. Current scan data from FeMn bilayer samples with different HM layers with $t_{FeMn} = 5$ nm. 59

Figure 5.5. Current scan data from Pt/IrMn samples with (a) AFM Thickness is $t_{IrMn_4} = 1$ nm, (b) 1.5 nm, (c) 2 nm, (d) 3 nm green data shows field cooling parallel to current (case I), red data in-plane perpendicular (case II) and blue data out-of-plane to current (case III). 61

Figure 5.6. Change in resistance fit for (a) AFM Thickness is $t_{IrMn_4} = 1$ nm, (b) 1.5 nm, (c) 2 nm, (d) 3 nm green data shows field cooling parallel to current (case I), red data in-plane perpendicular (case II) and blue data out-of-plane to current (case III). 62

Figure 5.7. Change in resistance with rising temperature for each thickness of t_{IrMn_4} samples. (a) t_{IrMn_4}=1 nm (b) 1.5 nm (c) 2 nm (d) 3 nm. . . 62

Figure 5.8. Cases fitted and offset depending on their amount of resistance drop for Pt(2)/$IrMn_4$(1.5) sample at 40 K where resistance makes a dip at temperature scan. 63

Figure 5.9. Current scan data from Ta/$IrMn_4$ samples with (a) AFM Thickness is $t_{IrMn_4} = 1$ nm (b) 1.5 nm (c) 2 nm, (d) 3 nm. 64

Figure 5.10. Change in resistance fitted for (a) AFM Thickness is $t_{IrMn_4} = 1$ nm (b) 1.5 nm (c) 2 nm , (d) 3 nm. 64

Figure 5.11. Change in resistance with rising temperature for each thickness ofTa/$IrMn_4$ samples. (a) t_{IrMn_4}=1, (b) 1.5 (c) 2 (d) 3 nm. 65

Figure 5.12. Current scan data from $Fe_{50}Mn_{50}$ tri-layers; (a) Ta/$Fe_{50}Mn_{50}$/Ta, (b)Ta/$Fe_{50}Mn_{50}$/ Pt (c) Pt/$Fe_{50}Mn_{50}$/Pt. 66

Figure 5.13. Current scan offset data from $Fe_{50}Mn_{50}$ tri-layers; (a) Ta/$Fe_{50}Mn_{50}$/Ta, (b)Ta/$Fe_{50}Mn_{50}$/ Pt (c) Pt/$Fe_{50}Mn_{50}$/Pt. 67

Figure 5.14. Resistance behaviour of samples with increasing temperature (a)Ta sandwich, (b)Ta/Pt,(c)Pt sandwich. 67

Figure 5.15. Current scan data from $IrMn_4$ tri-layer samples. with different HM combinations. (a) $IrMn_4$ without HM layer (b) Pt/$IrMn_4$/Pt, (c) Ta/$IrMn_4$/Pt , (d) Ta/$IrMn_4$/Ta. 69

Figure 5.16. Offset current scan data from $IrMn_4$ tri-layer samples. with different HM combinations. (a)$IrMn_4$ without HM layer (b) Pt/$IrMn_4$/Pt, (c) Ta/$IrMn_4$/Pt , (d) Ta/$IrMn_4$/Ta. 69

Figure 5.17. Temperature scan data from $IrMn_4$ tri-layer samples. with different HM combinations. (a)$IrMn_4$ without HM layer (b) Pt/$IrMn_4$/Pt, (c) Ta/$IrMn_4$/Pt , (d) Ta/$IrMn_4$/Ta. 70

Figure 5.18. Current scan data from FeMn multi-stack samples. (a) Single repeat of Ta/FeMn/Pt stack (b) Double repeat of Ta/FeMn/Pt stack (c)Triple repeat of Ta/FeMn/Pt stack. 71

Figure 5.19. Current scan data fit from FeMn multi-stack samples. (a) Single repeat of Ta/FeMn/Pt stack (b) Double repeat of Ta/FeMn/Pt stack (c)Triple repeat of Ta/FeMn/Pt stack. 72

Figure 5.20. Temperature scan data from FeMn multi-stack samples.(a) Single repeat of Ta/FeMn/Pt stack (b) Double repeat Ta/FeMn/Pt stack (c) Triple repeat of Ta/FeMn/Pt stack. 72

Figure 5.21. Current scan data from $IrMn_4$ multi-stack samples. (a) Single repeat of Ta/$IrMn_4$/Pt stack (b) Double repeat of Ta/$IrMn_4$/Pt stack (c)Triple repeat ofTa/$IrMn_4$/Pt stack. 73

Figure 5.22. Current scan data fit from $IrMn_4$ multi-stack samples. (a) Single (b) Double (c) Triple repeat of Ta/$IrMn_4$/Pt stack. 74

Figure 5.23. Temperature scan data from Ta/$IrMn_4$/Pt multi-stack samples.(a) Single (b) Double (c) Triple repeat of Ta/$IrMn_4$/Pt stack. 74

Figure 6.1. Expected effect on FeMn trilayer measurements. 77

Figure 6.2. Expected effect on $IrMn_4$ trilayer measurements. 77

Figure 6.3. Expected effect on FeMn multistack measurements. 80

Figure 6.4. Expected effect on $IrMn_4$ multistack measurements. 81

Figure 6.5. Circuitry scheme of a bilayer structure. Each element of circuit is given as variable resistances, since by thermal and magnetic effects alter the resistance values for each one. 82

Figure 6.6. Effect of contact damages on a sample after two wirebonding process in a row. 84

Figure 6.7. An experiment data to test the effectiveness of field cooling procedure. Red data represents the 1 T field cooled sample from second case measurement of $Pt(2)/IrMn_4(1.5)$ and blue data represents the current scan after cooling the same sample without a magnetic field. 85

LIST OF TABLES

Table 4.1. Deposition Calibration Measurements. 35

Table 4.2. Atomic Force Microscopy measurements. 36

Table 6.1. Percentage of Injected current into each layer. 83

LIST OF SYMBOLS

A	Area
H_C	Coercive field of material
H_{Ex}	Exchange field of material
H_{Ext}	Applied magnetic field
I	Current
$\mathbf{J_{ij}}$	Exchange Interaction between magnetic moments i and j
K	Magnetic anisotropy energy
$\tilde{L}$	Orbital angular momentum
L	Length
M_s	Saturation magnetization
R	Resistance
R_S	Anomalous Hall effect coefficient
$\tilde{S}$	Spin angular momentum
T_B	Blocking temperature
T_C	Currie temperature
T_N	Néel temperature
t_x	Thickness of material layer
V	Voltage
w	Width
γ	Gyromagnetic ratio
λ	Wavelength
θ_i	Spin Hall Angle of Material i
ρ	Resistivity
ρ_H	Hall resistivity

LIST OF ACRONYMS/ABBREVIATIONS

AFM	Antiferromagnet
AMR	Anisotropic magnetoresistance
DC	Direct current
DL	Damping-like
FEM	Finite element Method
FC	Field cooling
FL	Field-like
FM	Ferromagnet
GMR	Giant magnetoresistance effect
HM	Heavy metal
IRE	Inter-facial Rashba effect
LLG	Landau Lifshitz Gilbert
MRAM	Magneto-resistive random access memory
MTJ	Magnetic tunnel junction
NLSV	Non-local spin valve
NM	Non-magnetic
PPMS	Physical property measurement system
SHE	Spin Hall effect
SOC	Spin-orbit Coupling
SOT	Spin-orbit Torque
STT	Spin-transfer Torque
VSM	Vibrating sample magnetometer
XRD	X-ray diffraction

1. INTRODUCTION

Advancements in software technology and developing information technology shaping our daily lives, necessitate new technologies for developing feasible hardware solutions. There are limitations in the scaling such as inevitable heating of the devices due to scattering during charge transport and bits of silicon technology.These challenges led manufacturers to invest on exploration of new hardware technologies [1].

Quantum mechanics was the leading element of semi-conductor technology. Solutions to all obstacles in electronics lie in the realm of quantum mechanics. In order to fix all problems and step up the current consumer electronics, idea of "Spintronics" has been put forth. Instead of using charge transport properties of materials, it was an exciting idea to offer using spin degree of freedom of electrons and manipulating magnetic orientations of materials to enhance the operation of electronic devices. This way, it would be possible to store more information per cell with lesser heating due to charge scattering.

Following the realisation of magnetic manipulation ought to electronic technology with giant magneto resistance effect [2,3], research in magnetic materials has intensified. At this point, magnetically soft ferromagnetic (FM) materials were investigated in order to observe the benefits of magnetic manipulation by different physical mechanisms such as applied field, current and temperature [4]. At the final stage, it is commercially possible to manipulate spin lattices even by using spin angular momentum itself by spin transfer torque (STT). This technology revealed that polarized spin currents can be used to manipulate spin lattices of a FM layer and shift it's magnetization direction [5]. Relationship between current and magnetization was studied well over the years, since it's discovery by Lord Kelvin, named anisotropic magneto-resistance (AMR). Most important property of FM materials is having a single spin order parameter and non-zero magnitude of total magnetization, which leads to an advantage of inducing a potential energy term $U = -\vec{\mu}.\vec{H}$ when a single magnetic moment coupled with an external magnetic field H, as it can be seen in Figure 1.1.

Magnetic materials, find applications in data storage technology, where one needs to separate reading and writing schemes. An important task of the ferromagnetic recording technology is performing these tasks while mimicking traditional elements with higher performance. Though various mechanisms [4] have been engineered to process FM spintronic devices, in order to replace electronic ones, there were issues caused easily neighbouring bit disturbance of soft magnetic material media during operation. Not only stray field and disturbance, but also bits and complementary metal-oxide semiconductor (CMOS) integration was part of the problems that showed up during engineering phase of FM devices. At this point, researchers focused on efforts to develop alternative technologies.

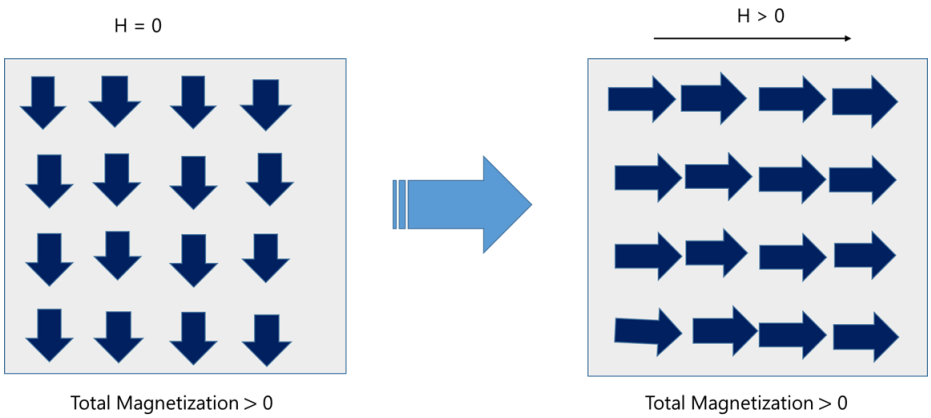

Figure 1.1. The response of ferromagnetic ordered spins work to an external magnetic field.

The first real candidate to replace FM materials in order to enhance the performance was anti ferromagnetic (AFM) materials [6]. These materials are not only non-responsive to magnetic disturbances and better thermal stability compared to FM materials (Figure 1.2), but also promise a new approach for bit/volume ratio, energy consumption and scaling. However, AFM materials are not easy to conduct research on, due to challenges in their characterization. Therefore, it's quite tempting to investigate exotic physics to discover new ways to characterize and utilize AFMs in commercial ground. AFM materials have two spin sub-lattices with same magnitude but in opposite directions, makes their total magnetization zero. Since magnetization induced by spin lattices will cancel each other, there will be no net magnetic alignment on material and won't be sensitive to stray fields unless there is a very high effect.

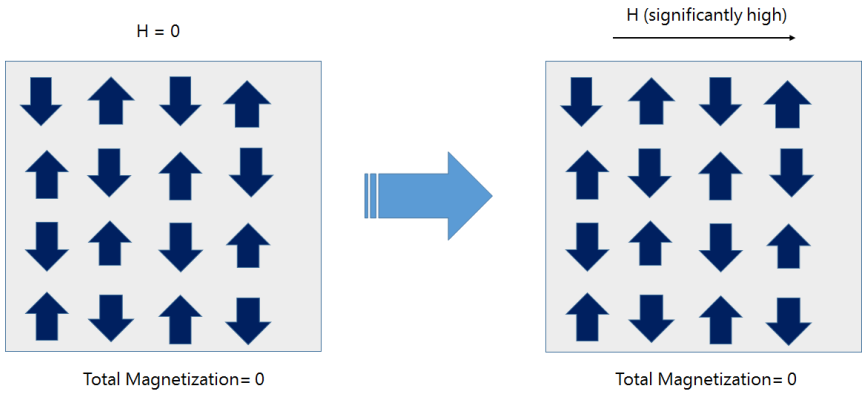

Figure 1.2. The response of antiferromagnetic ordered spins work to an external magnetic field.

The more exotic properties are, harder it becomes to investigate the AFM materials. In order to engineer this class of materials, the first step should be understanding the magnetic manipulation mechanism for spintronic applications. When considered as a replacement to FM spintronic devices, which are optimized for traditional STT technology, it was theoretically predictable that there will be problems on STT switching of AFM moments. Since there is not any bulk magnetization, it was not logical to expect a transfer torque to apply on distinct spin lattices like conventional FM materials, with no coupling to an external magnetic field. At this point, search for an alternative method to recruit AFM moments has begun.

Considering the traditional STT mechanism, which corresponds to perpendicular-to-plane injection of electrons and transfer of one quantum unit of spin angular momentum, there was a need for a polarization layer and a spacer to prevent magnetic interactions between layers, as shown in the Figure 1.3. Spacer can be selected as an insulator (MgO, SiO_2) [7] or a conductor with high spin diffusion lenght (Cu) [8]. In commercial use, breakdown of this insulator spacer method causes shorter life time of devices. Another tool for applying torque to distinct spin lattices could've solve the issue and build a promising framework for AFM spintronic technology. Necessity of influencing all spin sub-lattices at once gives hint about this tool needs to be an inter-facial effect. Another type of spin-torques, spin-orbit torque (SOT), induced by relativistic SOC effect promises a wide range of new applications to spintronics technology [9].

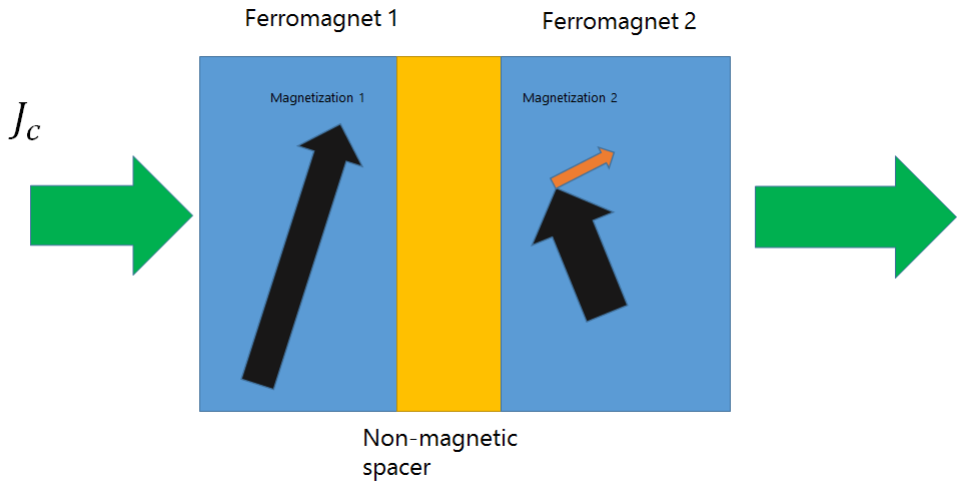

Figure 1.3. Working principle of an STT structure in FM.

In this work, interaction of AFM Néel order parameter with pure spin current induced by spin Hall effect (SHE) and interfacial Rashba effect (IRE) have been investigated. Experiments to observe interaction of antiferromagnetic spin lattices and pure spin current is performed. This investigation is performed by using regular electro-resistance effects, in order to understand the effect of SOT induced magnetic effects on resistance of materials. Layers with different spin conversion properties (spin Hall angles) are used in experiments to understand how charge-to-spin conversion mechanisms effect the torques on AFM layer. As the first phase, observation of SOT by resistance measurements are performed, followed by tri-layer and multilayer stacks of [HM/AFM] structure to understand the cumulative behaviour of this effect. Fundamental properties aside, various conditions also effecting the phenomena such as field cooling parameters, current density in layers, measurement system, artifacts and crystal orientation of AFM layer.

2. ANTIFERROMAGNETIC SPINTRONICS

2.1. Introduction to Antiferromagnets

Regarding the technological impact of GMR, magnetic materials play an important role in industry, as the crucial component of developing field spintronics. Since the field is an exclusive alternative to low-cost electronics, researchers are on a quest to reproduce electronic systems on spintronic devices. As it is easily understandable from it's name, spintronics uses the spin angular momentum of electrons and local moments in magnetic materials.

Since the early stage of 20 century, magnetic materials have been investigated and explored to replace electronic structures. Materials with specific magnetic properties, such as ferromagnets have already been used in magnetic read heads, magnetic sensors etc [4]. During this period, another important phenomenon which is observed by Néel, antiferromagnetism, has been also investigated and became a challenge to predict it's potential for future applications, as even the founder of the research Néel said, "They are extremely interesting from the theoretical viewpoint, but do not seem to have any applications."

Years after this comment, it was understood that antiferromagnetic materials were not near that being useless, in contrary, it has remarkable thermal and magnetic properties can be used in the spintronics field. Starting with magnetic hardening of ferromagnets by exchange bias, a lot of useful techniques to manipulate and use the magnetic moments of antiferromagnets have been developed and offering future applications.

2.1.1. History of Antiferromagnets

After the introduction of Weiss' molecular field theory as an explanation to ferromagnetism in 1906, series of experiments were run in order to obtain the correlations between theory and experimental data. Temperature dependence of magnetic susceptibility of Mn, Cr and alloys Co-Fe, Fe-Mn, Fe-Cr and chlorides $FeCl_2$, $CrCl_3$ and $NiCl_2$ were investigated. Since those materials' magnetic properties were quite exotic for that time, it took quite an amount of time to realize their potential.

While this phenomenon remained in shadow for years, Néel came up with the idea of combining Heisenberg's quantum mechanical exchange energy concept and Weiss' molecular field theory, resulting in the "local molecular field". When Weiss' theory applied to magnetic system, there was no room for collinear antiparallel magnetic moments. By applying exchange energy theory to current Weiss model, it was now possible to talk about a magnetic system with two antiparallel spin sublattices intertwine, first called "generalized ferromagnet", which was required to explain temperature dependence of magnetic susceptibility of alloy PtCo [10] and anomalously large temperature independent magnetic susceptibility of Cr. With this new theory, Néel claimed that there should be a peak on susceptibility/temperature data with a spontaneous occurrence at a pre-determined temperature, which will be known as Néel Temperature in future.

Meanwhile in Kharkov, Landau and Shubnikov were focused on the magnetic properties of layered anhydrous crystals of the chlorides of iron, cobalt, nickel, and chromium. The main motivation behind their study was an apparent awkwardness that occurred in susceptibility measurements. These compounds were performing slightly faster increase in susceptibility, inversely proportional to temperature, compared to Curie-Weiss law for FM materials in the paramagnetic domain. On the contrary, when the compounds were cooled down below the Curie temperature, there was not any ferromagnetic behaviour observed. In addition to this contradiction, after cooling off, susceptibility turned out to be dependent on the strength of applied magnetic field.

After those findings, Landau developed a theory built it on exchange interaction between magnetic ions. Assuming the exchange energy for parallel magnetic moments, which creates a spin sublattice, is positive and for antiparallel magnetic moments,

belongs to two different spin sub-lattices, is negative. He used this idea in order to explain anomalies mentioned above, and predicted two layered spin sub-system promote two sub lattices with anti-parallel alignments. Another important addition by Landau was the interaction of magnetic moments with lattice, which is the physical reason behind the mechanism "magnetic anisotropy" [11]. He stated that the minimum energy level of the system should be that when the magnetic moments are anti-parallel to each other, known as antiferromagnetic. His model explained the anomalies on temperature dependence of susceptibility and cooperative magnetic ordering without zero magnetic moment over crystal, with non-zero magnetic moments in the sub systems.

2.1.2. Characterization of Antiferromagnets

2.1.2.1. Neutron Scattering. After building a promising theory, it requires an experimental proof to turn theory into a law. In 1949, Shull and Smart designed and performed a neutron scattering experiment [12] in order to prove the theory of two anti-parallel spin layers intertwine. As the physical aspect of this experiment, Bragg equation was used to determine different waves scattered from different objects or scattered with a phase difference. When it came to understanding and identifying the antiferromagnetic spin structure, scattering properties of neutrons had used, since neutrons have magnetic moments, enabling scattering by electrons' magnetic moment. We can create an analogy to X-ray diffraction, where X-rays are scattered by electron density.

This structure is based upon the fact that magnetic ordering of material has only one lattice. In the antiferromagnetic aspect, which can be seen in Figure 2.3 [13], it is expected to obtain two different spin lattices intertwined, with anti parallel moments. This structure is expected to invoke another peak in crystal structure, in addition to the (100) peak in first experiment. Then an additional (111) body centered plane is expected to appear as an intensity peak when the temperature is reduced until a certain temperature, as a thought experiment. When the physical mechanism of an antiferromagnet is considered, it is expected to see that the scattered intensity of neutrons will result in different values for two different planes, since one plane is up spin and other plane is down spin. This variety results with one outcome, unlike the scattering from ferromagnetic structure, scattered waves will have different amplitudes and different phases, which makes it unlikely to cancel each other out.

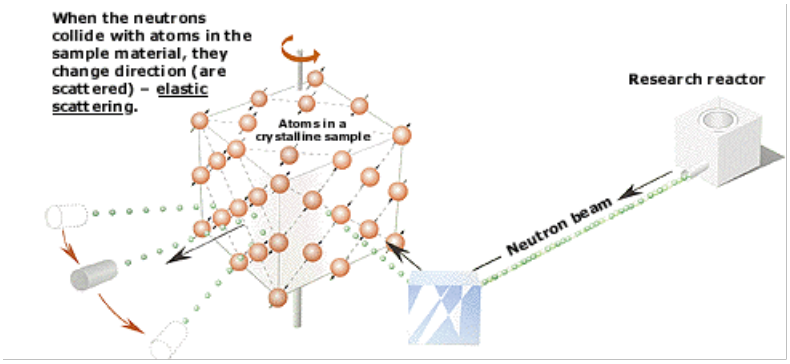

Figure 2.1. Neutron beams being scattered when two magnetic moments are one under other, single type of magnetic lattices, which occurs when MnO is over critical temperature.

The experiment shown in Figure 2.1 [12] had been performed by using MnO, a material displays antiferromagnetic properties under a critical temperature. In order to understand this nature, scattering experiments had repeated under and over a certain temperature. Before analyzing data, we need a brief elaboration on Bragg's law. Figure 2.2 [13] shows hen a ferromagnetic system is exposed to neutron scattering experiment, same and periodic lattice structure makes neutrons scatter simultaneously.

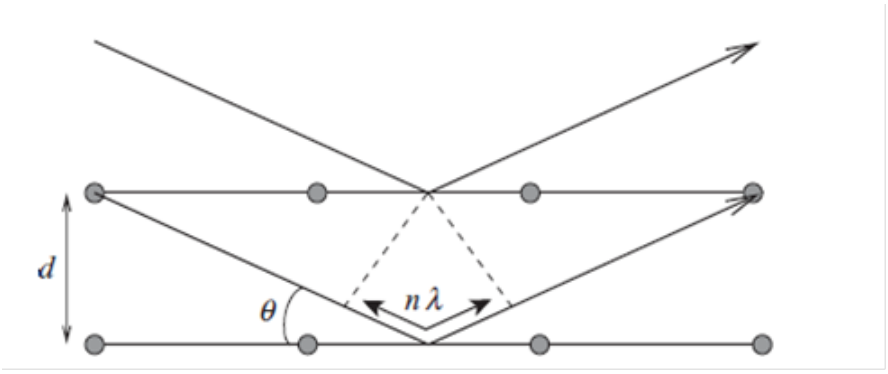

Figure 2.2. Regular scattering mechanism for a single lattice system.

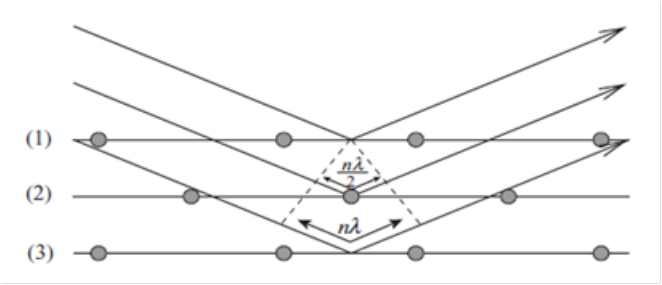

Figure 2.3. Scattering mechanism of a two spin sub-lattice system.

While considering the data, we should also remember the Bragg equation, which ends up with the required parameter to calculate the intensity of the scattered waves; wave length. Equation is;

$$n\lambda = 2d \sin\theta, \tag{2.1}$$

where λ is wavelength, d is distance between planes and θ is the angle between incoming light and plane. After the series of experiments, resulting data proves the theoretical predictions in a convincing way.

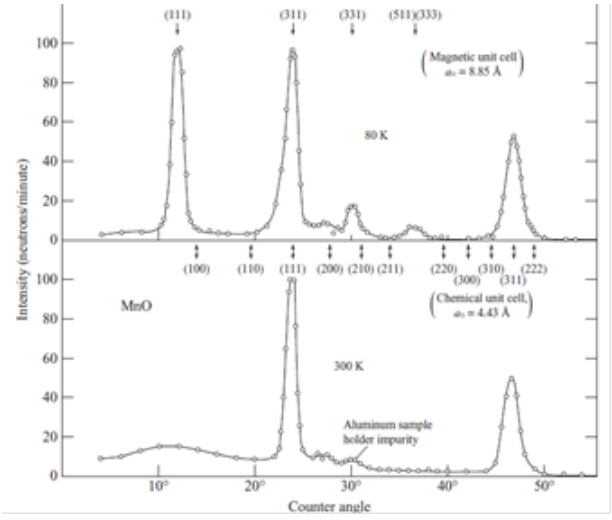

Figure 2.4. Neutron diffraction data for MnO, up is 80 K, down side is room temperature .

Data presented above for MnO [13], which has a crystal form of face centered cubic form, it is easily observed that the additional peak when temperature is reduced to 80 K, which is in a different direction (311) than the peak when at room temperature, the domain where the material is expected to lose it's antiferromagnetic properties. This difference is basically due to change of magnetic unit cell of system under Néel phase transition temperature, which is presented in Figure 2.4. Following this experiment, antiferromagnetic structure was proven and archived as the first experimental observation of magnetic phase transition from a single type of magnetic alignment to collective of two anti-parallel magnetic alignments. Crystal structure of this behaviour is presented in Figure 2.5 [13].

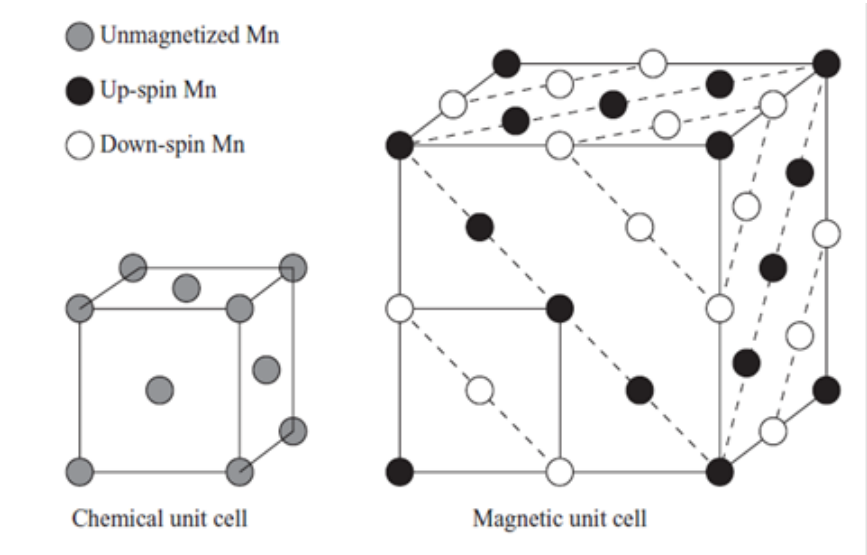

Figure 2.5. Neutron diffraction data for MnO, up is 80 K, down side is room temperature.

2.2. Magnetic Manipulation of Antiferromagnets

Regarding unconventional nature of AFM materials, it is quite necessary to understand the limits of their magnetic toughness and different mechanisms to manipulate it. There are various suggested techniques for manipulating AFM moments, but in this section we will mention two important mechanisms for our aim to observe the interaction of field cooled AFM layers and pure spin currents.

2.2.1. Anisotropic Magnetoresistance

Anisotropic magnetoresistance was first observed by Lord Kelvin, 1857. At first, it was all about the angle between magnetization of the material and current direction. After years of research, interesting properties and components of AMR effect have been observed, such as invariance of magnetization reversal, componential structure of crystalline and non-crystalline counterparts and that it's foundation actually lies beneath spin-orbit interaction [14].

One of the most important studies on AMR effect at room temperature antiferromagnet is on FeRh. What makes this material unique is phase transition from ferromagnet to antiferromagnetic state at room temperature and by cooling in field, desired antiferromagnetic order can be obtained. Data in Figure 2.6 [15] shows that, depending on the direction of the cooling field arranging the antiferromagnetic moments, resistance values measured by an in plane current, remained sustainable and reproducible at room temperature domain . This report also gives hint about measuring antiferromagnetic spin lattice transformations by using AMR effect.

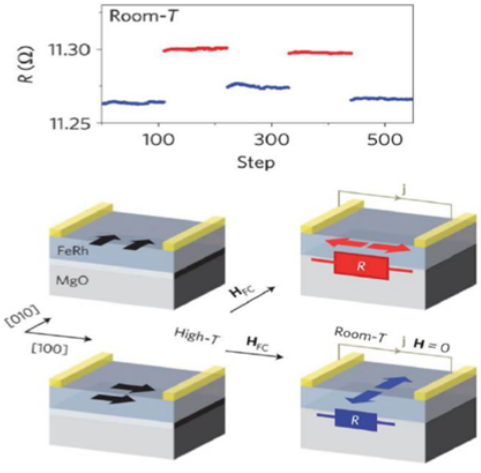

Figure 2.6. Detection of anisotropic magnetoresistance behaviour occuring in FeRh sample .

2.2.2. Manipulation with Magnetic Field

Antiferromagnets are not-so-sensitive to external magnetic fields in contrast to ferromagnets, which does not necessarily mean that their magnetic moments can not be manipulated by an external field. Depending on the magnetic anisotropy, magnetic moments of antiferromagnets can be canted or even flipped by an applied external field. Since the saturation fields for required Zeeman energy which compensates the exchange energy between AFM moments is generally high, configuring the AFM moments by an applied field is not the first choice to perform a spintronic application.

Interestingly, this solid behaviour and magnetic hardness makes them even more attractive for non-volatile memory applications in high-magnetic field circumstances such as space applications. One should approach to Stoner-Wolfarth model to understand the magnetization properties of an antiferromagnet under an applied field. Relationship can be expressed as

$$E = \mu_0 H_{ext} M_s \cos(2\Phi) + K \cos(\Phi)^2 - \mu_0 M_s \cos(\Phi), \tag{2.2}$$

where Φ is the angle between applied magnetic field and magnetic moments and

$$\mu_0 H_{ext} = J_{Af} S^2/(\mu B), \tag{2.3}$$

where J_{Af} is exchange energy, H_{ext} is applied external field, μ_0 is vacuum permeability, K is magnetic anisotropy energy, E is the total energy of the system and M_s is the saturation magnetization of each sub-lattice. When H_{ext} is perpendicular to the easy axis of magnetization, magnetic moments on sub-lattices cant and a net magnetization M gradually builds up depending on H_{ext}. M_{net} saturates when system reaches the saturation field such that Zeeman energy equals to sum of exchange energy and anisotropy energy.

When an external field is applied parallel to it's easy axis, if the anisotropy energy is small compared to exchange energy, sub-lattice magnetization remains in it's easy axis with zero net magnetization until Zeeman energy compensates the anisotropy. After the compensation sub-lattice magnetization is now free to rotate in directions perpendicular to the easy axis with consuming no energy, which is called spin flop transition.

Another interesting case is where the anisotropy is not small compared to Exchange energy, things slightly alter. Once again there has to be a saturation, but this time magnetic moments jump to saturation level directly from zero magnetization, which is called spin flip transition.

2.2.3. Spin-Orbit Coupling

Condensed matter systems and electronic devices are based on electrons moving in trajectories surrounded with various boundaries inside the material. There are various effects and interactions that alter these trajectories and influence the electron motion inside the matter. Electron interactions have always been a promising aspect in physics and with advancing condensed matter technologies it plays a crucial role in daily life electronic devices as well. One of the most fundamental interaction of electrons is coupling of orbital angular momentum and spin angular momentum, since this effect promises a huge revolution in electronics.

Spin-orbit interaction is a relativistic effect, which creates an additional energy term in system's Hamiltonian. Briefly, taking a Hydrogen atom with single proton and single electron in the orbit would be enough to explain this mechanism (Figure 2.7). If we assume we have the proton's reference frame, it is easy to imagine proton is standing still in the nucleus and an electron is moving around, with orbital angular momentum and it's spin.

When the reference frame is changed to electron's reference frame, the proton is moving with it's spin and the electron is the one stands still. Which means that, by the rules of special relativity, the electron is under an influence of a magnetic field, aside from electric field of nucleus. Electron carries spin, which will have an energy term when there is an external magnetic field, hence this mechanism create an additional energy term of $\vec{L} \cdot \vec{S}$ where is the orbital angular momentum of electron and is the spin angular momentum of electron.

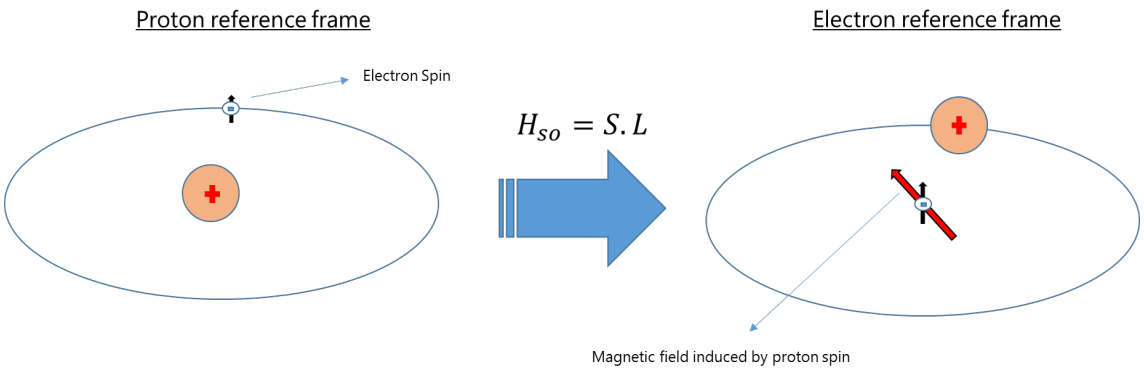

Figure 2.7. Schematic of how spin-orbit interaction takes place in orbital electrons.

As one can imagine, not only electrons in atomic orbitals but also electrons moving inside the material are also influenced by this effect. Including the electron-electron, electron-lattice and spin-orbit interactions into transport of electrons empirically showed very interesting results on ground breaking physics. Regarding the interaction of spin angular momentum and orbital angular momentum, it was even possible to manipulate the conduction properties of magnetic materials and design them by using external sources.

2.2.4. Spin Hall Effect & Rashba Effect

Starting with discovery of AMR by Lord Kelvin in 1856, the relation between injected current and magnetic properties of material was at great interest to a wide range of scientists. One of them was Edwin Hall, who discovered the behaviour of electrical current when mixed up by an external magnetic field. When Edwin Hall made the discovery of this relativistic effect, which causes electrons to move towards a non-regular path, there seemed to be a lot of room to further investigate this subject. When Hall effect measurements are performed with a magnetic material, some extra contributions in the equation appear as

$$\rho_H = R_0 H_{Ext} + 4\pi R_S M, \tag{2.4}$$

where the terms are; R_0 is ordinary Hall coefficient, R_S anomolous Hall coefficient, M is there magnetization of ferromagnet,H_{Ext} is the applied external field and ρ_H is the Hall resistivity. These terms in the equation can be investigated as first and second ones.

First term is directly coming from a regular Hall effect measurement, second term is the contribution from interacting current and magnetization of the material, which is a part of spin-orbit interaction. This contribution is called anomalous Hall effect (AHE).

Considering spin-degree of freedom, it is not hard to imagine how AHE causes a scattering between magnetization and upcoming electron's spin angular momentum. If we perform a simple mind experiment and exclude all magnetic properties of the material and include only spin-orbit interactions, we may expect a spin dependent scattering, which cancels all Hall voltages caused by other scattering mechanisms. In this context, what to expect is , observing two distinct currents where up and down spin electrons are accumulated into opposite directions. This phenomenon that occurs in a non-magnetic high spin orbit coupled material is called the spin Hall effect (SHE).This mechanism enables us to convert electrical current with mixed spin electrons into pure spin current with up spin electrons and down spin electrons moving towards opposite directions, orthogonal to the applied charge current.

2.2.4.1. Spin Hall Effect. Spin hall effect is enabled by the spin-orbit coupling. It induces a pure spin current orthogonal to the incoming current density. When the reverse order happens as the pure spin current is converted to charge current, the process is named Inverse spin Hall effect (ISHE). Spin Hall effect is generally used for pure spin current generation from strong spin orbit coupling materials, such as heavy metals. As it is an alternative for spin pumping for pure spin current generation, it has also been investigated to apply to antiferromagnetic devices. When the strong spin orbit coupling is recalled, first idea to apply this on would be antiferromagnetic metals with strong spin-orbit coupling, such as $IrMn_4$. An important study on feasibility of metallic AFM $IrMn_4$ as a replacement of a heavy metal in a spin Hall system have been investigated by Mendes et al at 2014 [16]. Main philosophy behind the study is injecting spins with two different ways to the both AFM layer and heavy metal layer and measure the potential induced by current density formed over the inverse spin Hall effect, then compare the potentials in order to obtain their spin Hall angles, which is the ratio of injected spin current density to induced charge current density. Data in Figure 2.9 [16] shows that heavy metal AFM $IrMn_4$ shows similar spin Hall angle properties with Pt.

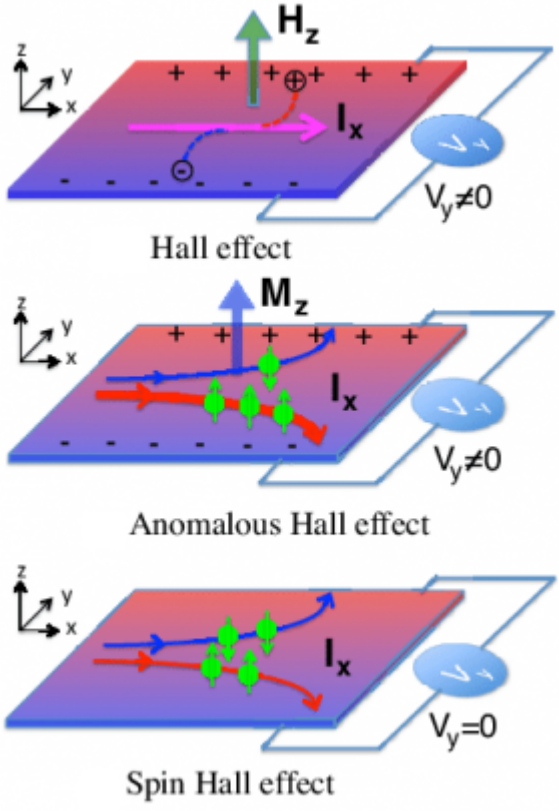

Figure 2.8. Illustration for the some of the members of Hall effect family. From top to bottom; ordinary Hall effect, anomalous Hall effect, spin Hall effect.

2.2.4.2. Rashba & Edelstein Effect. Another important mechanism for our study is interfacial Rashba & Edelstein effect (IRE),which is caused by the lack of inversion symmetry of magnetic structure and momentum scattering of free electrons. When we consider a structure with multiple layers, a possible lattice mismatch on interface causes an additional spin polarization mechanism beside SHE. Since these two mechanisms both may occur in our ultra-thin metallic structures, we could expect both phenomena to contribute to the charge-to-spin current conversion. While SHE occurs on the bulk of material, IRE is invoked at the interface. This phenomenon promises a new application of current switching of antiferromagnetic moments as well, since it creates an additional contribution to generated pure spin current in system.

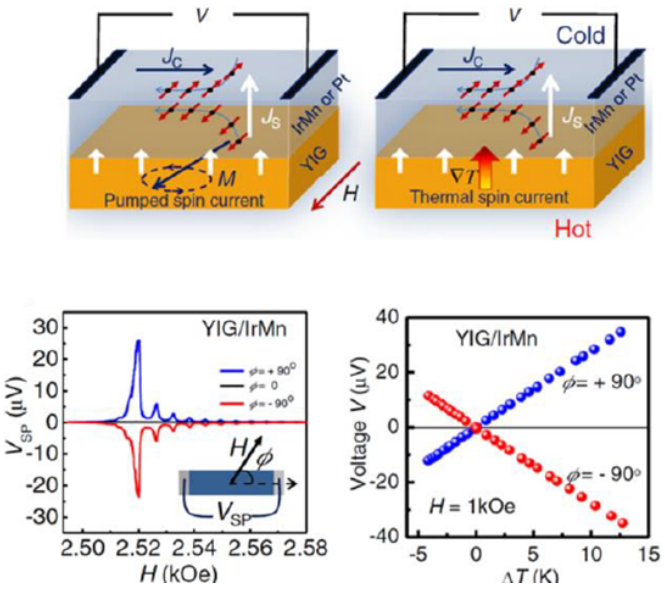

Figure 2.9. Comparing ISHE properties of $IrMn_4$ and Pt shows $IrMn_4$ can be used as a pure spin current source in an AFM spin lattice.

2.2.5. Spin-Orbit Torque

In magnetic systems lacking inversion symmetry (globally or locally) and possessing sizable spin-orbit coupling, the transfer of angular momentum between the orbital angular momentum of carriers and the spin angular moment of the localized electrons result in so-called spin-orbit torques [17]. As mentioned above, spin-orbit torque is a promising effect for magnetic manipulation. Since the nature of this effect consists of inter-facial influences, it makes even more sense to adapt it into manipulation of antiferromagnetic moments, where the sample has no net magnetization.

Comparing SOT and STT as two different torques acting on spin lattices, it could make more sense to take a look at it's mathematical identification. Using regular LLG equation for manipulation of magnetic moments is the right way to understand the differences of these two phenomena. As we already know two types of torques, SOT should be investigated for it's applied torque behaviour. Investigation can be performed by using relationship

$$m'(t) = \gamma m_M + \alpha m \times m'(t) + \frac{\gamma}{M_s} T. \tag{2.5}$$

Relationship above known as LLG equation, where

$$m = \frac{M}{M_s}. \tag{2.6}$$

M_s is saturation magnetization, m unit magnetization vector, α is dimensionless Gilbert damping parameter, T represents all non-energy derivative torques and γ is absolute gyromagnetic ratio ($\gamma > 0$).

In order to understand the full scope, LLG equaiton can be investigated in three divisions, each contribution is separated by summations. First contribution comes from the precession of magnetic moment, under the influence of and effective field B_M,which corresponds to the functional of magnetic energy density $\frac{\partial \epsilon}{\partial M}$. Second term represents the contribution from relaxation of magnetic moment towards it's equilibrium. At the last term, contribution from torques other energy derivatives is given.

Comparing the torques applied to a single magnetic moment requires describing the geometrical trajectories of torques and how they are grouped. Torques on system is divided into two parts as shown in Figure 2.10 [18], field like torques (τ_{FL}) and damping like torques (τ_{DL}).

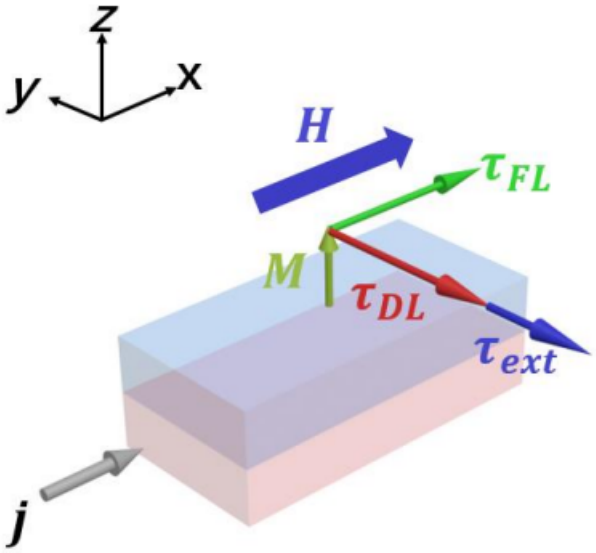

Figure 2.10. Illustration of applied torques on magnetic moment, induced by current in a FM/HM structure.

Different torques on magnetic moments have different parameters. Brief breakdown of these torques can be shown as

$$T = (\tau_{FL}) \times \xi + (\tau_{DL})(m \times \xi). \tag{2.7}$$

Combinations of these torques are the most important tools for manipulating magnetic moments. Theoretical framework of this mechanism is based on injecting pure spin current induced by SHE and IRE into magnetic layer, as shown in Figure 2.11 [19]. This injection can be performed by any kind of high-SOC material, such as heavy metals [20], topological insulators [21] etc. Manipulation of FM materials by SOT have been studied and verified multiple times [17]. How ever,it is confusing to understand which phenomena originates from this torque, IRE or SHE. Various studies have been performed [22] for describing what kind of torques they are inducing, in the end SOT induced on a materials is sum of these two effects.

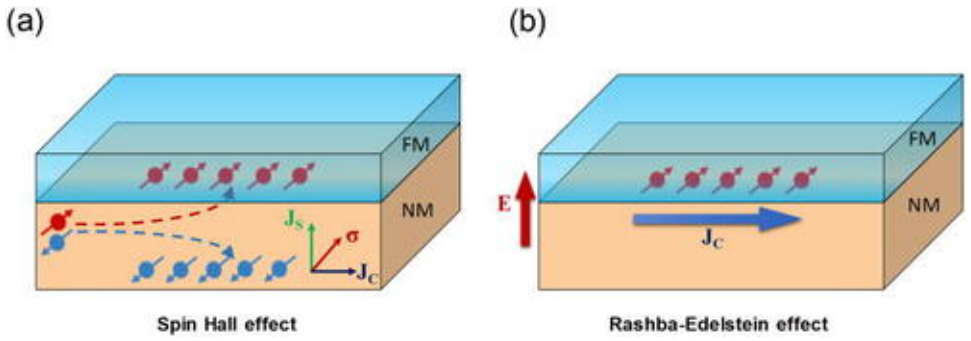

Figure 2.11. Schematic comparison of inducing SOT on a ferromagnet by using (a) spin Hall effect, (b) Rashba effect.

Analyzing these two effects with the torques they are responsible of, understanding the AFM switching is quite crucial. Fundamental difference between τ_{FL} and τ_{DL} for the case of manipulating AFM moments is that one aligns on the cross product of the magnetization of single magnetic moment and spin polarization vector, while other is another additional cross product of magnetization of the magnetic moment. This picture tells us that applying a τ_{FL} induces the same mechanism of applying an external magnetic field on material, which is insufficient on switching mechanisms. When considering τ_{DL}, it is possible to achieve different torque alignment for different magnetization, which makes sense for obtaining a reliable magnetization switching. Regarding this, it is safe to say τ_{FL} induced by IRE will be insufficient in AFM magnetization switching, while τ_{DL} is more capable of triggering a switching.

Given the circumstances, realizing the SOT by current injection depends on many parameters. In this case, manipulating the AFM order with a pure spin current injected to the AFM layer from a non-magnetic HM layer should be investigated for not only spin manipulation, but also interaction of pure spin current and AFM spin lattices. One of the most fundamental techniques for describing the magnetic variations of a material would be the AMR effect. As we have mentioned above, it has been shown that AMR capabilities exists in AFM materials as well. Hence, the recipe for interacting pure spin current with AFM moments would be pure spin current dominated by SHE rather than IRE and making sure observing resistance change in AFM layer. Prominent studies shown that it was possible to obtain AFM switching by current injection [23].

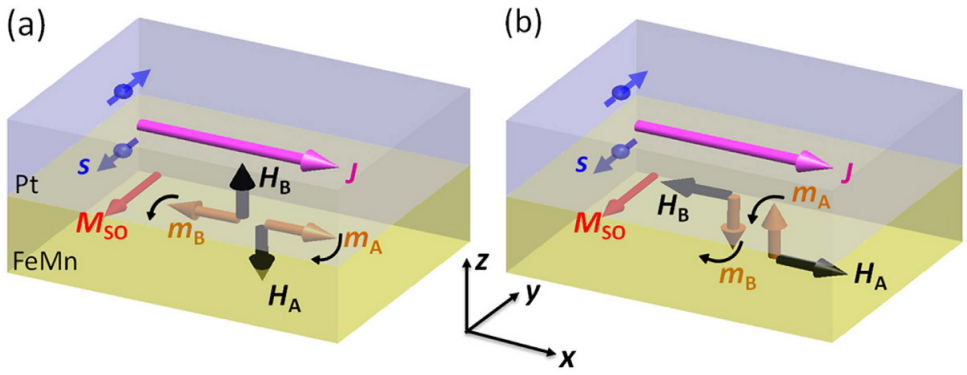

Figure 2.12. Anatomy of spin Hall effect induced spin-orbit torque on Heavy Metal/Antiferromagnet bilayers. (a) If the antiferromagnetic order is in-plane. (b) If the antiferromagnetic order is out of plane.

Regarding the antiferromagnetic order in AFM materials, SOT promise a great approach to replace STT for manipulating AFM moments. Inter-facial torque invoked by SOT is capable of influencing a whole spin lattice of antiferromagnetic material and create a torque to interact with each magnetic moment at once, as shown in Figure 2.12 [24]. One of the most important question addressed by this study is, would it be possible to use these inter-facial effects to enhance the torque in AFM layer. Placing an AFM layer sandwiched with opposite spin Hall angle materials promises a mechanism for this purpose. Regarding the spin Hall angle definition, engineering the current density is also crucial for given mechanism. Hence, it is important to optimize the injected current and current density due to parameters such as thermal effects caused by Joule heating, artifacts and field cooling process, each stack of HM/AFM/HM (Figure 2.14a) requires another set of optimization in terms of applied current and Hall bar width to engineer such a physical mechanism.

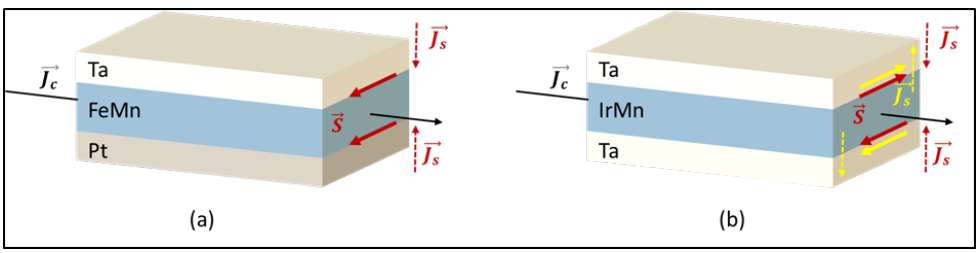

Figure 2.13. Expected physical mechanism of a sandwich structure.

2.2.6. Detection of Spin-Orbit Torque

Research focused on SOT phenomena brought various sensing mechanisms for different SOT inducing systems. This mechanisms heavily depends on the source of SOT and induction criteria. Before detailed explanation of our study, in this section a brief discussion for some of the most well-known practices of SOT observation is given. Experimental techniques in this section are sorted as the current induced SHE and IRE based magnetic systems. While it is important to acknowledge the reader on whole scope of SOT detection methods, regarding the scope of our study, only the DC influenced methods are taken into account.

From it's experimental discovery, SHE induced SOT studies are mostly based on FM materials, relying on their soft magnetic properties. Altering the fundamental parameters for pure spin current and measuring different behaviours effecting on magnetization and SOT is the main idea behind these techniques. In order to obtain a theoretical framework for the mechanism, spin Hall relationship is used;

$$J_s = \frac{\hbar}{2e}\theta_{SH}(\vec{\sigma} \times J_c). \tag{2.8}$$

Relationship between pure spin current and current density is given in the equation above [25], where J_s is accumulated spin current density, J_c is injected current density, $\vec{\sigma}$ is spin polarization unit vector, $\hbar$ is Planck's constant and e is the charge of electron. Here the term θ_{SH} describes the identity of how efficient charge current density accumulates the pure spin current, called spin Hall angle. All methods discussed here are based on this relationship and extended to understand complex dependence between many variables.

2.2.6.1. Non-Local Spin Valve. One of the first techniques to identify SOT is the non-local spin valve technique (NLSV) [26]. It is based on transport of accumulated spin current by using a conductor with high spin diffusion length to FM layer [27]. The method consists three nano-strips, SH nano-strip for pure spin current accumulation, FM nano-strip for magnetization switching and a good conductor with high spin diffusion length for conduction of spin current [8]. This method is feasible for both SHE and ISHE measurements all due to its working principle. However, since it is crucial to optimize the thicknesses for all layers and obtain a reliable spin-diffusion length

for materials, this method may not be feasible and demanding for some exotic transport studies. Experimental study verified that it is possible to observe SOT effects by using NLSV experiment setup, which can be found in Figure 2.14 with detailed explanation [28].

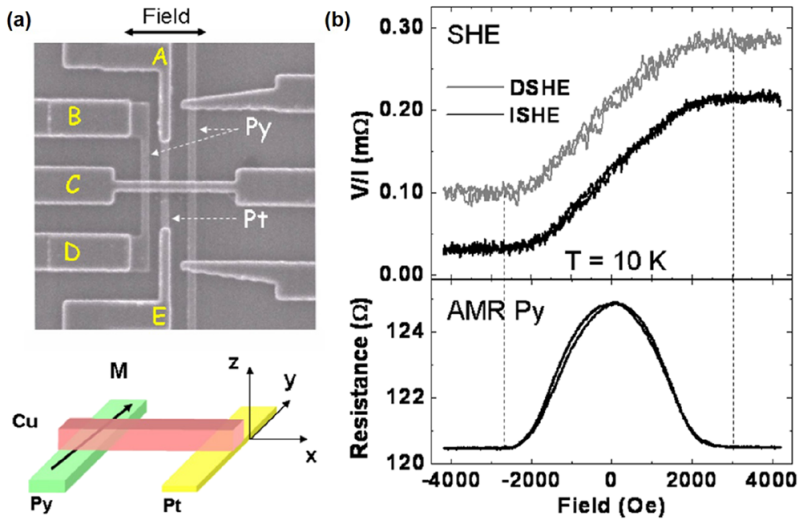

Figure 2.14. (a) SEM image combined with illustration of non-local spin valve mechanism, (b) SHE and ISHE measurements performed with given device.

2.2.6.2. DC Current Switching. Considering the main goal of research on spintronic devices, which is to build a reliable commercial SOT-MRAM device [9], DC induced magnetization switching by using SOT is an exciting achievement. This method includes a magnetic tunnel junction (MTJ) placed on a bulk SH material. Nano-pillar structure is preferred to minimize the micro magnetic effects to create magnetization with uniform fashion. There are also cases depending on FM layer magnetic easy axis, which makes this method even challenging. Not only the magnetic anisotropy of easy axis remains challenging for this method, but also nano-fabrication of perfect ellipse nano-pillar process. Similar to NLSV method, it remains challenging to perform this method for exotic materials, which requires advanced deposition and fabrication methods [29]. By using DC current switching method, analyzing resistance of MTJ device against applied DC current pulses and applied field by performing a two-way scan, it is possible to observe switching trends and optimize the switching parameters.

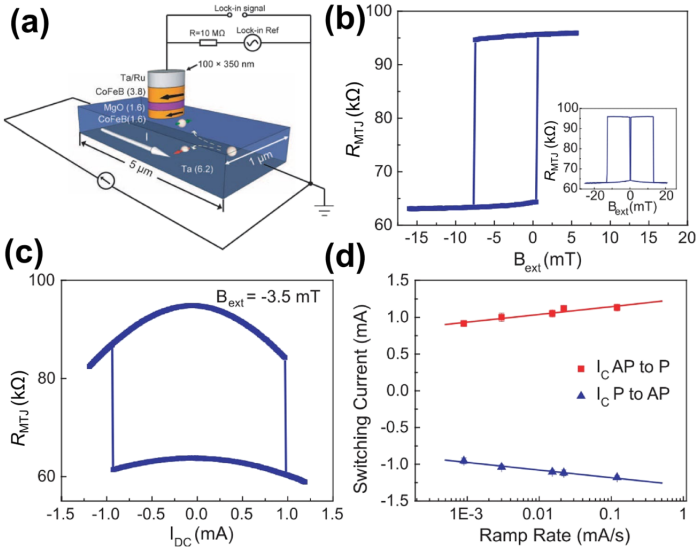

Figure 2.15. (a) Schematic of the DC current switching device. (b) Resistance against field in long axis. Inset data belongs to magnetic major loop of device. (c) Resistance behaviour against applied current to MTJ. (d) Switching currents as a function of ramping rates.

SOT effect is claimed as observable with applied current and resistance measurements. Regarding it's solid theoretical and experimental foundation, it was even possible to observe SOT in HM/AFM bilayers by using electroresistance measurements with field cooling protocols [24]. Instead of using a nano-pillar, we aim probing the effects of SOT in electroresistance with a simpler mechanism. Regarding multiple parameters effecting conductivity, dominance of SOT will be questioned as magnetic interactions will be the weaker perturbations in a two prope electroresistance measurement.

3. FABRICATION TECHNIQUES

Before diving into the steps taken for the project, it is crucial to digest and understand the pathway of each step. Therefore, each step is described in the order of sample fabrication and electronic transport measurements. For the electronic transport experiments, resistivity and Hall bar devices were fabricated as shown in Figure 3.2. Here, the resistivity samples can be used to understand how the resistivity of a material depends on temperature (20K to 300K) and its thickness (10 nm and 50 nm). Additionally, the Hall bar samples can be used to investigate the spin-orbit torque (SOT) induced effects as a function of magnitude of applied current. The resistivity and Hall bar geometries have been patterned on Si/SiO_2 substrates by using photolithography technique with several steps including thin film deposition and lift-off processes.

After the sample fabrication, electrical contacts have been bonded to the chip by using wirebonder. In order to check for bond health, an ohmmeter can be used to check if contact points have the desired resistance value. It is important to mention here that, do not use an ohmmeter if the sample contains nano-device. It can destroy your sample. If the bonds have a problem at the very beginning of measurement, your effort, time and sources will be wasted. After completing each step,a follow up table has been updated.

3.1. Photolithography

3.1.1. Hall Bar Fabrication

Fabricating the bars for both Hall and resistivity samples starts with design of photo-masks. All the designs of photo-masks have been done by using "Layout Editor" software. A screen shot taken from the software (Figure 3.1) shows the design of Hall bar geometry with different widths ranging from 2 µm to 80 µm. The main property here is the width dependence of Hall bar structures. Since the width will determine the current density injected into the material, adjusting width will be crucial for various transport measurements. Two different masks designs have been prepared for the contact pads of Hall bars as given in Figure 3.1. The design shown at the left side can be used for wirebonder. The other one can be used for probing.

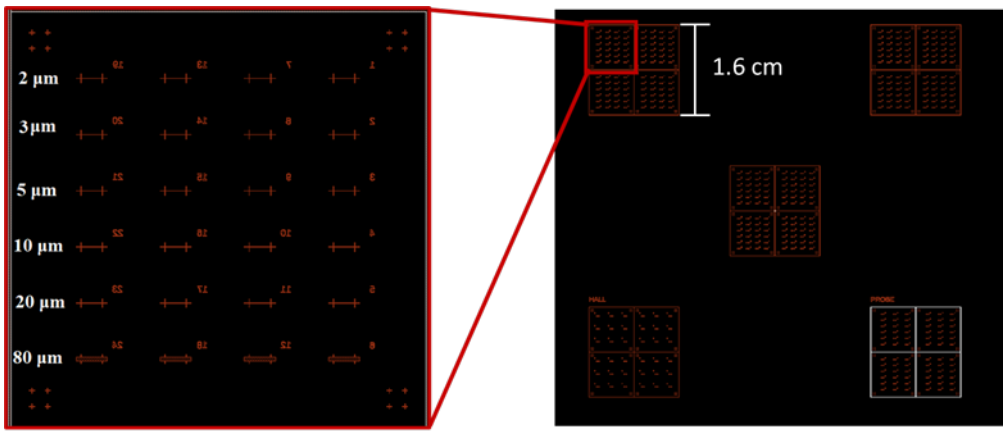

Figure 3.1. Hall Bar mask design in Layout Editor. First picture shows bars with different widths, second picture shows arrays of bars.

The designed photo-masks have been fabricated in National Nanotechnology Research Center (UNAM) at Bilkent University and all the photo lithography steps have been performed in a clean room environment at Sabancı University Nanotechnology Research and Application Center (SUNUM). It is important to mention here, during the transportation of samples between SUNUM and Boğaziçi Universities, isolating the samples in a vacuum pack is a priority to avoid them form dust. If this process is not performed by extensive sensitivity, it can be resulted with unexpected electrical and profiling measurements, since there will be dust inside the Hall bar cavities even before it is filled with desired material. Steps for Hall bar fabrications are:

(i) Spin Coating: Si/SiO_2 substrates (500 nm thickness) are coated with AZ5214 photo resist material by spin coater in 4000 rpm. Coated for 45 seconds, resulted 1.4 μm.

(ii) Soft Bake: After covering the substrates with photo resist material, samples are left to bake for 1 minute at 115.

(iii) Exposure: Baked substrates are cooled down to room temperature and followed by exposure to 365 nm wavelength UV lights over the pre-designed mask. This process enables the Hall bar structures to be penetrated into substrate with given parameters on mask.

(iv) Development: Processed substrates are put into AZ726 MIF developer for 45 seconds and rinsed with splashing DI water followed by blowing N_2.

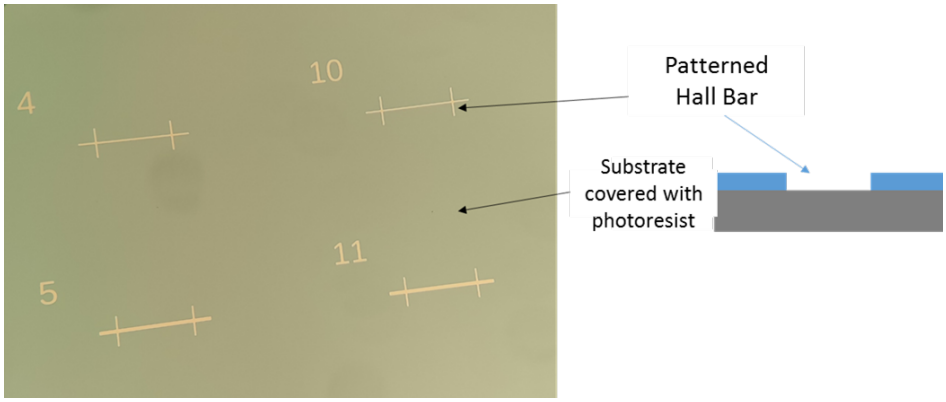

Figure 3.2. Illustration of Hall bar patterns after first lithography step.

3.1.2. Contact Fabrication

After lifting off the residual photo resist material from surface of the sample, it is time for fabricating the contact pads on both resistivity and hall bar structures. These pads will be the particular area where the bonds will be wired to chip's legs' contact points and run electrical measurements. Fabrication process requires another round of photo lithography process. This time photo-lithography will be aligned, since contact pads require a sharp alignment with edges of bars. Steps for this process are:

(i) Spin Coating: Once again wafers with Hall bars patterned had put into photo-resist material AZ5214 coating speed of 4000 rpm, 45 seconds of coating resulting 1.4 μm thickness photo-resist.

(ii) Soft Bake: Similar to first lithography step, before UV exposure substrates are left to bake for 2 minutes at 90.

(iii) First Exposure: Different from first lithography step, by using mask aligner, only the contact masks are aligned to the edges of Hall bars and exposed to UV light for 2.5 seconds.

(iv) Post Exposure Bake: Before second exposure, samples are left to bake for second time for 2 minutes in 90.

(v) Second Exposure: In this step, all parts of sample is exposed to UV light for 12 seconds. This way, all areas exposed to UV light gets tougher and leaves electrical contact pads with 2.5 seconds less from exposing UV.

(vi) Developing: Same developing procedure is applied for second time. This way areas exposed to UV lesser than other parts (electrical contact pads) are expected to dissolve faster, due to lack of toughness.

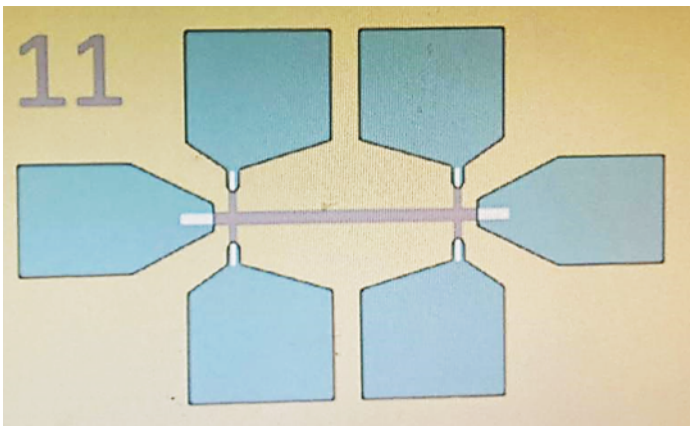

Figure 3.3. Result of contact lithography.

3.2. Chemical Procedures

During device fabrication process, we require some chemical procedures for furnishing our device perfectly. These procedures are lift-off and varnishing procedures.

3.2.1. Lift-Off

Extracting photo-resist remains from surface by chemical compounds is called lift off. After each photo-lithography step, there will be photo-resist residues. These residues can be dissolved by using acetone. When acetone is evaporated, it leaves permanent damage on a sample, which can be avoided by instant isopropanol splash. Regarding this, on to the second step, we use the sonic vibration and put beaker inside the sonic vibrator for 5 minutes to increase the effect of acetone solving photo-resist by constant oscillation enhanced quick dissolution of remained photo-resist. This step can also be replaced by leaving sample overnight inside acetone and rinse it with isopropanol right after. At the third step, beaker is extracted from sonic vibrator and sample inside the beaker is taken out immediately out of beaker to avoid air contact, put into another beaker prepared beforehand which is filled with isopropanol. As the fourth step, second step is repeated for isopropanol filled beaker. At the very end, sample is taken out of beaker and splashed dried with N_2 gas with some pressure, to get rid of remaining liquid on the surface. We perform this procedure twice in fabrication process.

3.2.1.1. First Lift-Off. After first sputtering step, Hall bar is filled with desired material and the whole surface of the wafer. Beneath the sputtered material, whole surface but inside the Hall bars is covered with photo-resist. Aim of the first lift-off is to lift the photo-resist beneath the sputtered film and leaving Hall bars as the only areas deposited. Schematic description of the process is given in Figure 3.4.

3.2.1.2. Second Lift-Off. After deposition of Hall bars, contact fabrication takes place. Once again after deposition of contacts, another round of lift-off is performed in order to get rid of photo-resist remains around the surface. Important note here is to perform oxygen plasma (descum) for one minute and ion milling right after.

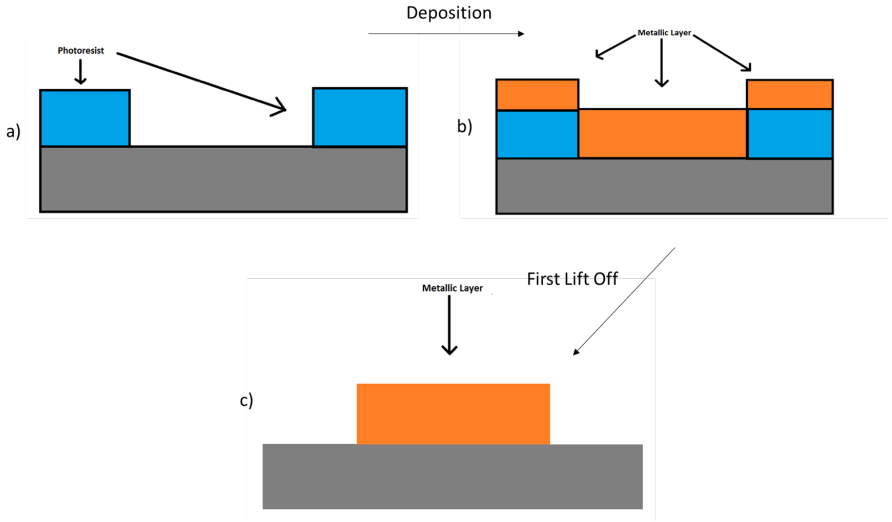

Figure 3.4. First Lift off process (a) before deposition of metallic films, (b) after deposition of metallic films, (c) after first lift-off.

Oxygen plasma process helps getting rid of the photo-resist lying in depths on contacts and ion milling procedure cleans the area from oxides. Right after this sequence, sample is ready for contact sputtering, which concludes with second lift-off.

3.2.2. GeVarnish Procedure

GeVarnish is a chemical compound used for sticking our Hall bar samples to printed circuit boards (PCB). It can be thinned by using fifty percent ethanol/toluene mixture and can be applied to desired material. Key point about this compound are, it may lose it's sticky nature and it's viscosity may increase when the sample is heated may cause sample to be moved.

3.3. Magnetron Sputtering

Physics we are after in this study requires layers of metallic thin films with clean interfaces. Fabrication of these films are crucial as it can be assumed. There are several methods that can be used for fabrication of such thin film metallic structures. Magnetron sputtering is one of the most efficient and well-structured methods to perform deposition of ultra-thin metallic films on substrates.

Its working principle is based on characterizing target and substrate as cathode and anode, respectively. Supplying the conditions in ultra-high vacuum environment filled with an inert gas, preferably Ar, in our deposition strategy. Considering the target (bulk material that we want to sputter our thin film with) and substrate (sample to be sputtered) are two elements as cathode and anode, what we want to achieve is extracting atoms from top of the cathode and move them to surface of our substrate. For this mechanism, DC voltage is applied to cathode with magnets beneath, which generates an Ar plasma.This plasma is a consequence of the glow discharge and this effect accelerates the free electrons with required energy, thus they can ionize Ar atoms. As the small percentage of Ar atoms are ionized to Ar^+ , these ions strike the surface of the target material extract the neutral atoms and initiate their route towards the substrate. This makes our sample covered with atoms of the desired target. Schematic for magnetron sputtering can be seen in Figure 3.5 [30].

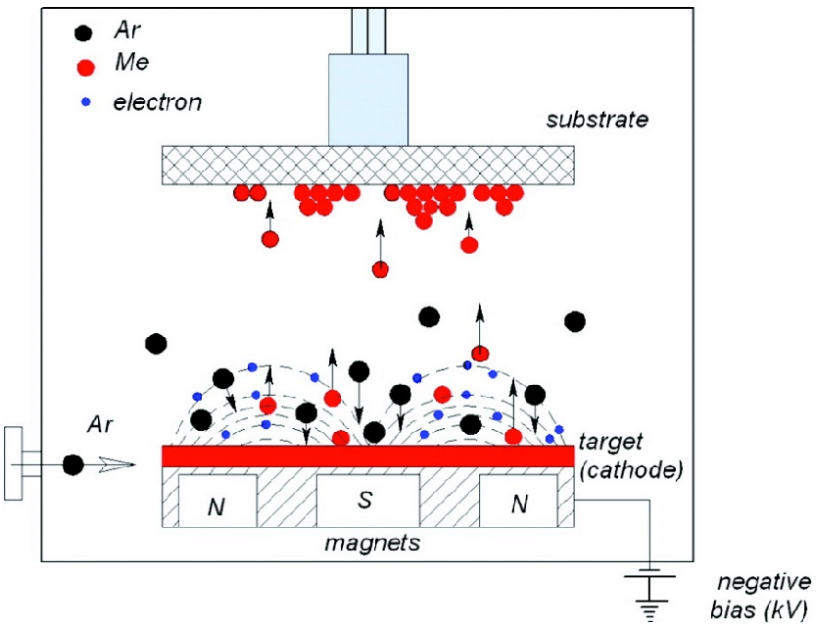

Figure 3.5. Magnetron sputtering mechanism. Black dots represent Ar atoms, red dots present metallic atoms, small blue dots present electrons.

3.4. E-Beam Evaporation

Thermal evaporation is another thin film deposition method, performed by electron beams falling on the target and extracting the atoms on the target surface by thermally evaporating them. Mechanism is triggered by a filament as electron beam source, focusing the beam on the ingot for heating , which makes the ingot material to evaporate and deposit on the sample ,is located on top of the ingot material (Figure 3.6 [31]). This process requires high vacuum conditions, considering our setup is set to have 10^{-7} mTorrs.

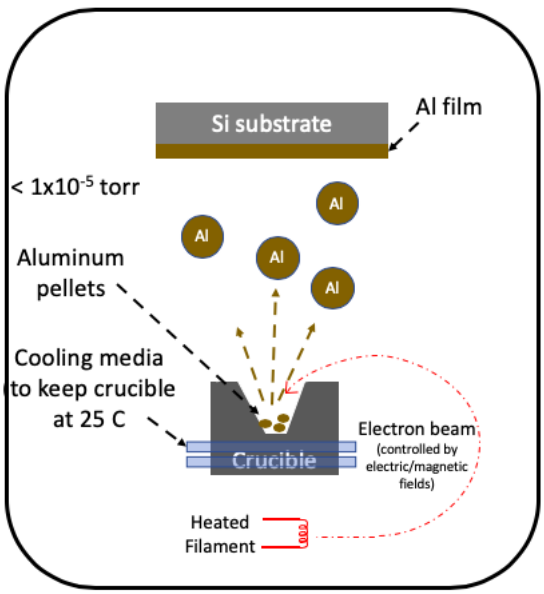

Figure 3.6. Schematic for an example usage of e-beam evaporation technique.

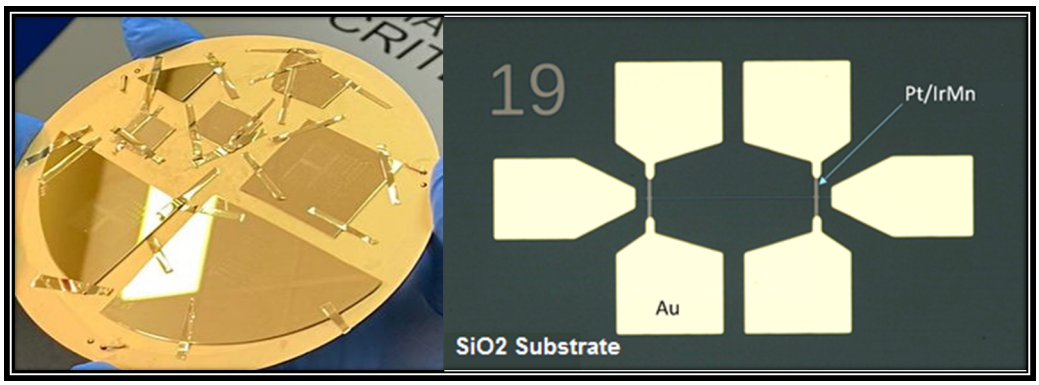

Figure 3.7. Picture and microscope image of samples after Cr & Au evaporation.

E-beam evaporation is performed exclusively for contact sputtering (Figure 3.7). After second photo-lithography, samples are delivered to descum process and ion milling, hence contact pads will be filled with 2 nm of Ti at the bottom and 3 nm of Pt layer on top of it. After we make sure possible oxidization on contact pads is prevented, we deposit 10 nm of Cr and 100 nm of Au in order to make perfect adhesion.

4. MATERIAL CHARACTERIZATIONS

4.1. Deposition Rate Calibrations

Calibrating the deposition is quite crucial for obtaining exact amount of thickness electroresistance experiments. Physical mechanisms expected to occur in these experiments heavily rely on high quality sputtering and very specific thicknesses that maximizes the effects.

Calibration process is performed with calibration gratings on Si/SiO_2 substrate for deposition calibrations. Metallic films are sputtered directly on substrate, AFM films are sputtered on 0.5 nm Ti adhesion layer on the bottom. After lift-off, calibration gratings are measured by using profiler. Mechanism of profiler can be described as a needle moving around the surface, sensitive to heights around 10 nm minimum. For our sputtering rate measurements, nearly 50 nm height calibration gratings were sputtered and calibrated.

4.1.1. Thickness Calibrations

Thickness calibrations hold a crucial importance for deposition process.Thickness calibrations are performed for achieving a reliable sputtering rate from each gun and calculating the required sputtering time for depositions. Obtaining a reliable calibration rate makes the required thicknesses easily achievable with magnetron sputtering. Regarding this, before starting the deposition process, thickness calibration steps must be performed for each gun, which will be used during the deposition process.

Thickness calibrations are performed with profiler, which is sensitive to nearly 10 nm height structures. Even it is possible to obtain smaller heights with profiler, preferred amount of height for calibration samples is slightly around 50 nm, in order to prevent noise contributions and achieving reliable results.

Figure 4.1. Sputtering rate measurement procedure. From left to right, one single calibration grating, and partial images of gratings to be measured.

One should mention an important factor here, fastest deposition is not always the preferred way. For example, in our studies we aim to use 2 nm of Pt layers, which is quite thin regarding the height. When the Pt plasma is triggered by using 30W, it is expected to be deposited faster, which may cause partial discontinuities on film. Regarding this, it has been decided to lower the plasma power and perform Pt sputtering 20 W to make it more reliable. Here in Table 4.1, it is shown how relationship between DC power (W) and deposition rate (A/s) changes.

Table 4.1. Deposition Calibration Measurements.

Material	Pressure (mTorrs)	Power (W)	Sputtering Rate (A/s)
FeMn	2	100	0.55 ± 0.02
FeMn	2	30	0.16 ± 0.02
$IrMn_4$	2	100	1.01 ± 0.01
$IrMn_4$	2	50	0.41 ± 0.01
$IrMn_4$	2	30	0.28 ± 0.01
$IrMn_3$	2	30	0.33 ± 0.01
Ta	2	100	0.70 ± 0.01
Ta	2	30	0.17 ± 0.01
Pt	2	100	1.24 ± 0.05
Pt	2	30	0.31 ± 0.03
Ti	2	50	0.17 ± 0.01

4.1.2. Roughnes Characterizations

As mentioned in previous sections, deposition of thin films and their roughness parameters holds a crucial place in experiment phase. Achieving the necessary torque depends heavily on how atoms are oriented on surface. Regarding this, atomic force microscopy measurements have been performed for observing roughness of sputtered films on substrates.

During deposition, magnetron sputtering might not be enough for perfect alignment of atoms. Physical mechanisms to be occurred in these sputtered samples heavily depend on symmetries and defects of surfaces. Roughness measurements hold very important place in detecting these defects and characterizing them with other measurements. Electrical fields, magnetic and topographic impurities and lattice mismatches may also cause experimental errors is electrical measurements.

Table 4.2. Atomic Force Microscopy measurements.

Material	R_q (nm)	R_a (nm)
Ta	0.35	0.26
Pt	0.34	0.24
FeMn	0.67	0.5
IrMn	0.81	0.59

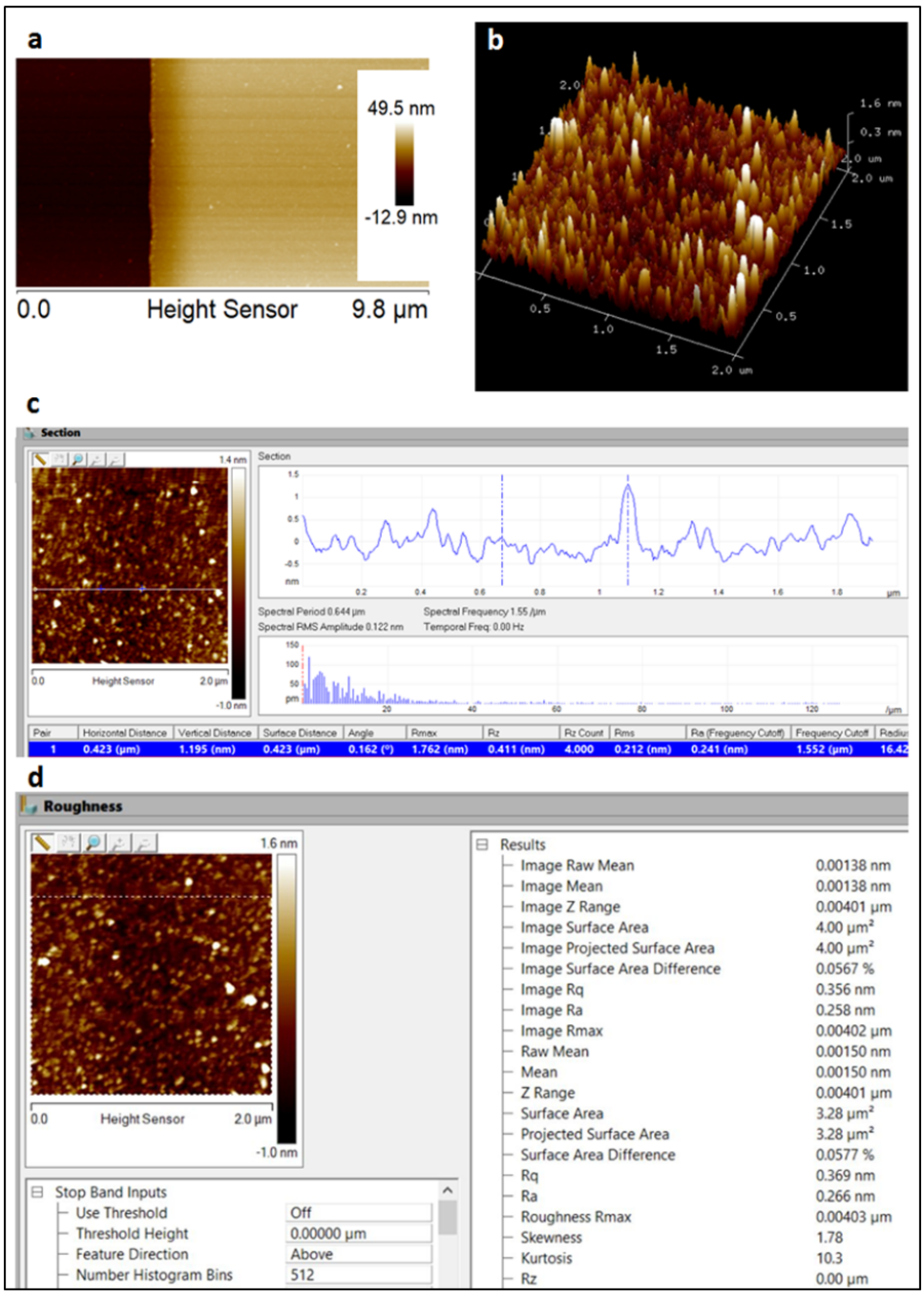

Figure 4.2. Atomic force microscopy data from Pt thin film roughness measurements.

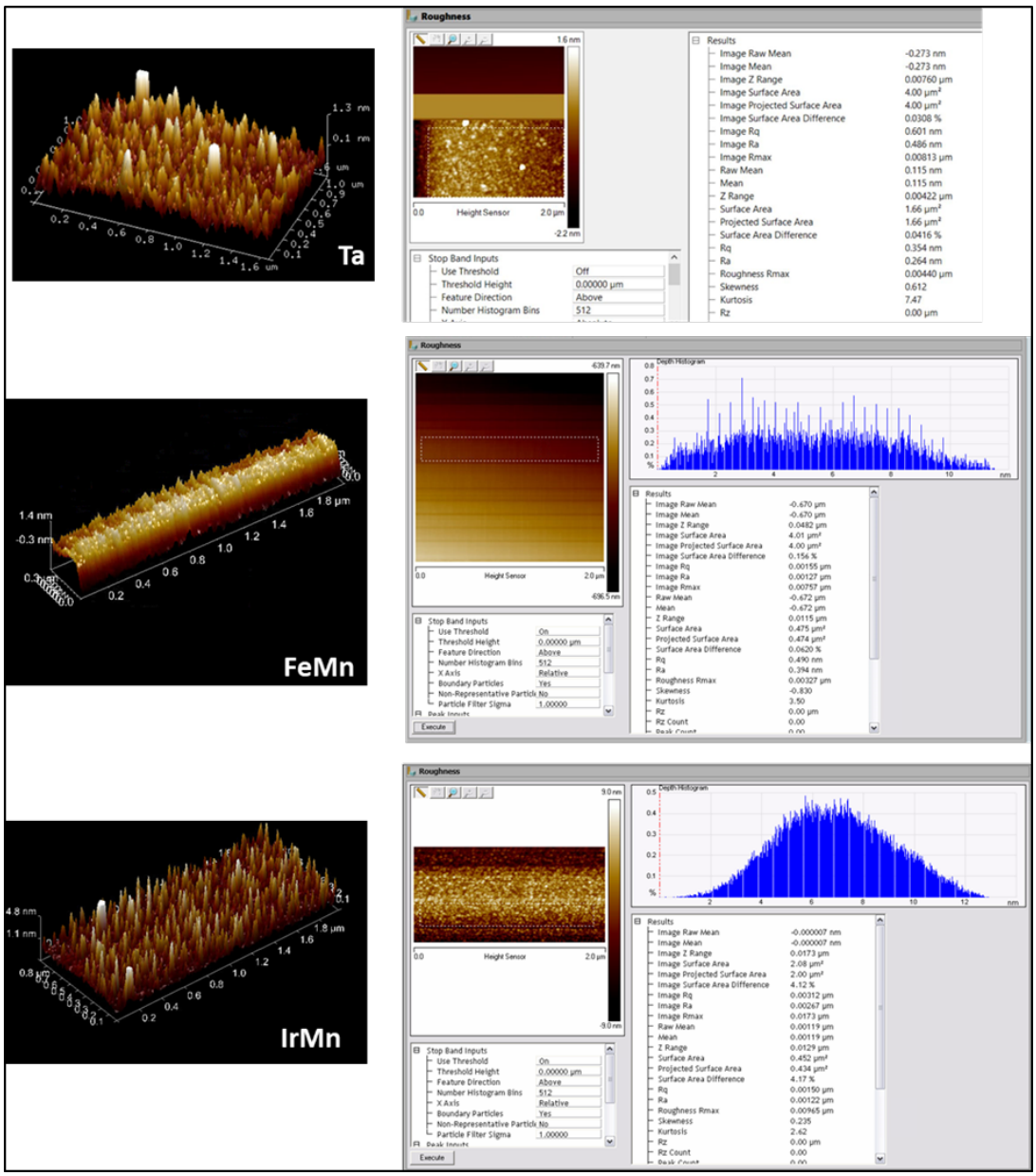

Figure 4.3. Atomic force microscopy data for roughness measurements from top to bottom; Ta, FeMn, IrMn.

For sensitive cases, $2 \times 2\ \mu m^2$ area for measurement in 0.2-0.3 Hz velocity of scan is advised for a definition of 512×512 pixels. Introduction for one of the samples to elaborate on procedure, Pt sample scan is started with 10x10 μm^2 area to obtain the calibration gratings. After this, sensitive measurement in $2 \times 2\ \mu m^2$ area scan is performed and an actual area of 3.28 μm^2 is taken into scanning. Result shows that a highest peak of 4 nm occured with 0.369 R_q and 0.266 nm of R_a values. Image of this measurements and other deposited films are given below in Table 4.2, with the of roughness data for each material(Figure 4.2 and 4.3).

4.1.3. XRD Measurements

X-ray diffraction (XRD) is a method used for analyzing crystal orientation of a certain structure. Considering Bragg's law, diffraction of x-rays through the lattices gives peaks in certain crystal directions, which results as the crystal orientation (Figure 4.4 [32]). Using this method, one can comment on the structure of the deposited material whether it is single crystal, poly-crystal or crystal structure is aligned in a certain direction or not.

It has been shown that crystal orientation of $IrMn_4$ has a direct effect on spin Hall angle [33]. Since $IrMn_4$is one of the AFM layers to be investigated in this study, it was crucial to observe the effects of different orientation leads to $IrMn_3$ structure by using different substrates. Analyzing how IrMn structure is located on different substrates have been performed by XRD measurements. For the XRD study of $IrMn_3$, different types of samples was prepared. Question to be answered in this experiment was to identify crystal orientation of $IrMn_3$ on different substrates, hence use this in SOT experiments. In order to achieve ¡100¿ and ¡111¿ oriented $IrMn_3$ samples, SiO_2, MgO (100), M-cut and R-cut Al_2O_3 substrates and Pt layer as adhesive layer was used.

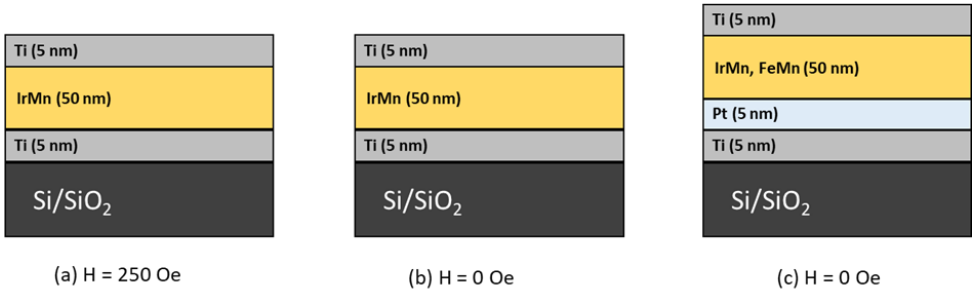

Figure 4.4. Si/SiO_2 substrate samples for XRD investigation.

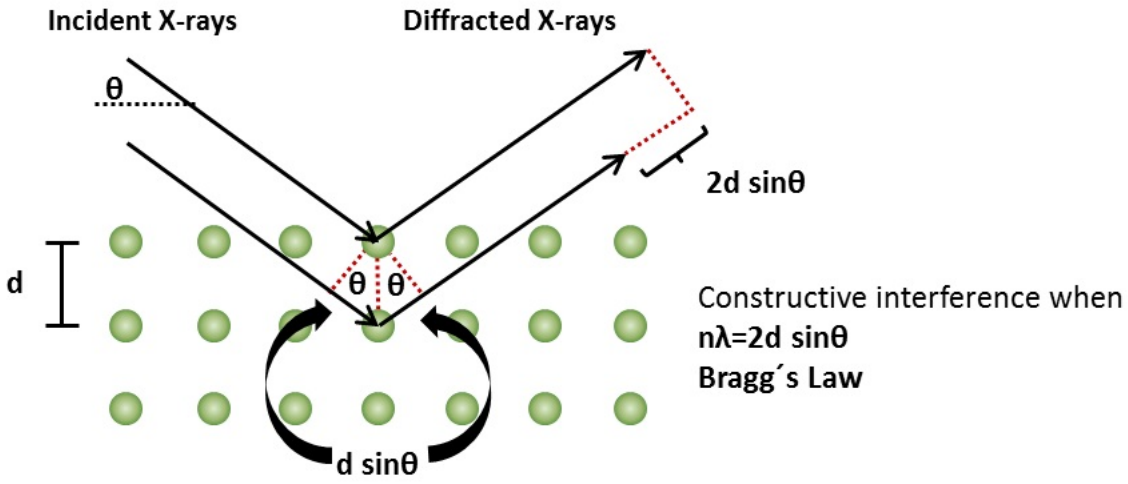

Figure 4.5. Bragg rule and the working principle of XRD. X-rays create constructive interference only when Bragg law is satisfied,where n is the number of atoms, d is the lattice constant and θ is the incoming angle.

In the first study, amorphous SiO_2 used as substrate and as adhesion layer, Pt, Ti was used. For an additional sample, effect of applied magnetic field of 250 Oe during sputtering is also investigated. Magnetic field is induced by magnetic stage inserted to AJA sputtering system. Figure 4.6 shows that in given cases, only the Pt layer with magnetic stage gives rise to (111) $IrMn_4$ orientation. Other two cases gives similar intensity peaks while Pt case gives very strong peak for (111) $IrMn_4$ orientation. Following investigation is conducted for MgO (100) substrate.

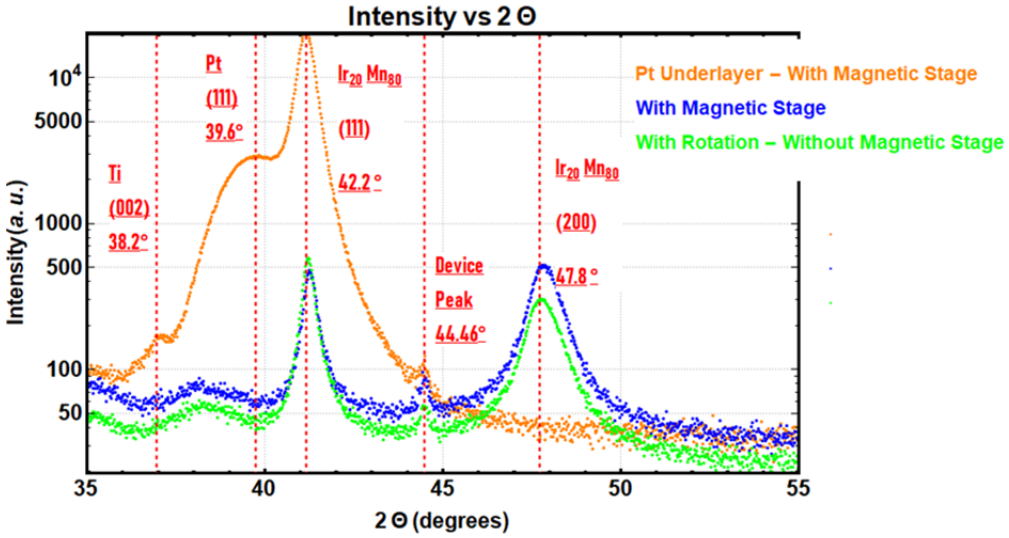

Figure 4.6. Si/SiO_2 substrate samples XRD results; orange data belongs to sample prepared with magnetic stage, on Pt layer. Blue data shows IrMn sputtered on 5 nm Ti layer with magnetic stage. Green data shows IrMn sputtered on 5 nm Ti layer without magnetic field.

Crystal orientation and peak strength of epitaxially deposited $IrMn_3$ is investigated. Results shows, when compared to lone MgO (100) substrate, epitaxially deposited $IrMn_3$, enhanced the magnitude of MgO peaks, while increasing width of signal. When the orientation of $IrMn_3$ is discussed, a strong (200) peak with a hidden (111) peak shadowed by dominant MgO signal is observed. An additional peak occurred due to humidity during deposition, even if it was epitaxial and heated up to 825 during process.

Next investigation was to understand the crystal orientation on various substrates such as M-cut and R-cut Al_2O_3 and Si/SiO_2. Figure 4.9 shows the XRD data for $IrMn_3$ on R-Cut Al_2O_3 substrate. Data shows no peaks on (111) direction, but a strong peak at (200). This means R-Cut Al_2O_3 substrate is feasible for fabricating (200) aligned $IrMn_3$ sample. Another XRD data on M-Cut Al_2O_3 is shown in Figure 4.10. Data shows a peak in (200) direction for $IrMn_3$, featured with other weak signals coming from device, Ti and (111) direction. Main property of this two data separated from amorphous Si/SiO_2, when sputtering is performed on a amorphous substrate, it is impossible to obtain a single crystal $IrMn_3$.

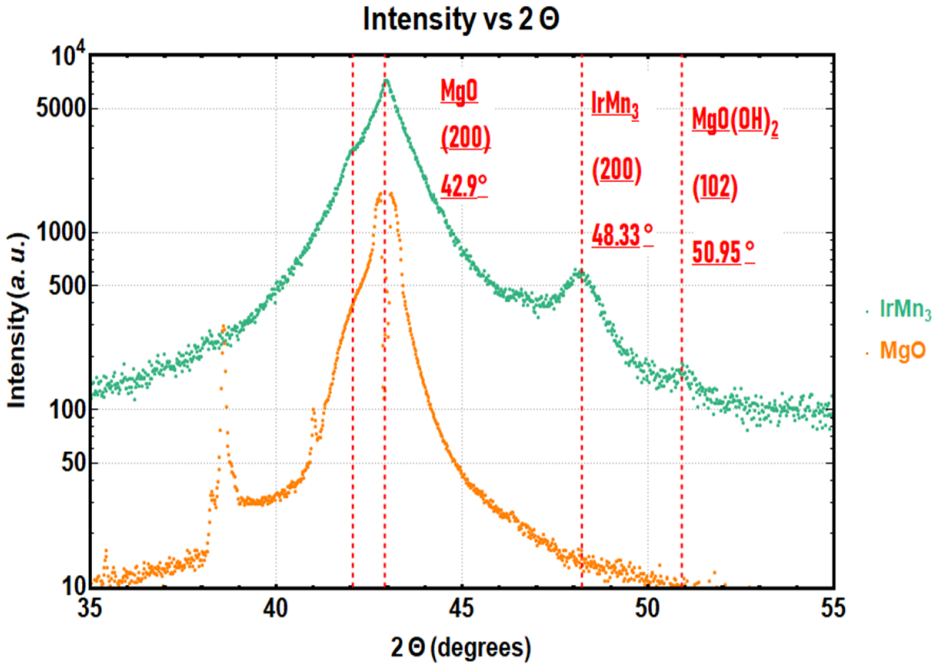

Figure 4.7. MgO substrate samples XRD results; green data shows MgO/$IrMn_3$ sample, orange data shows only MgO(100) XRD measurements.

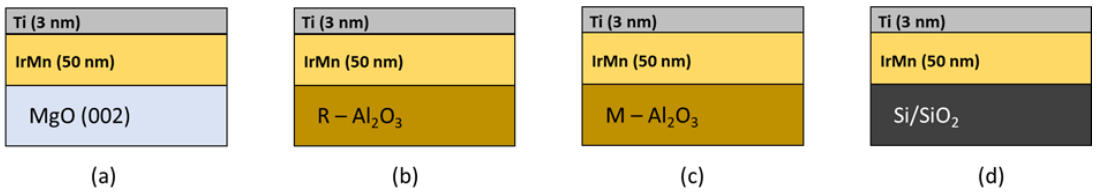

Figure 4.8. $IrMn_3$ deposition on different substrates. (a) MgO (002), (b) R cut Al_2O_3, (c) M cut Al_2O_3, (d) Si/SiO_2

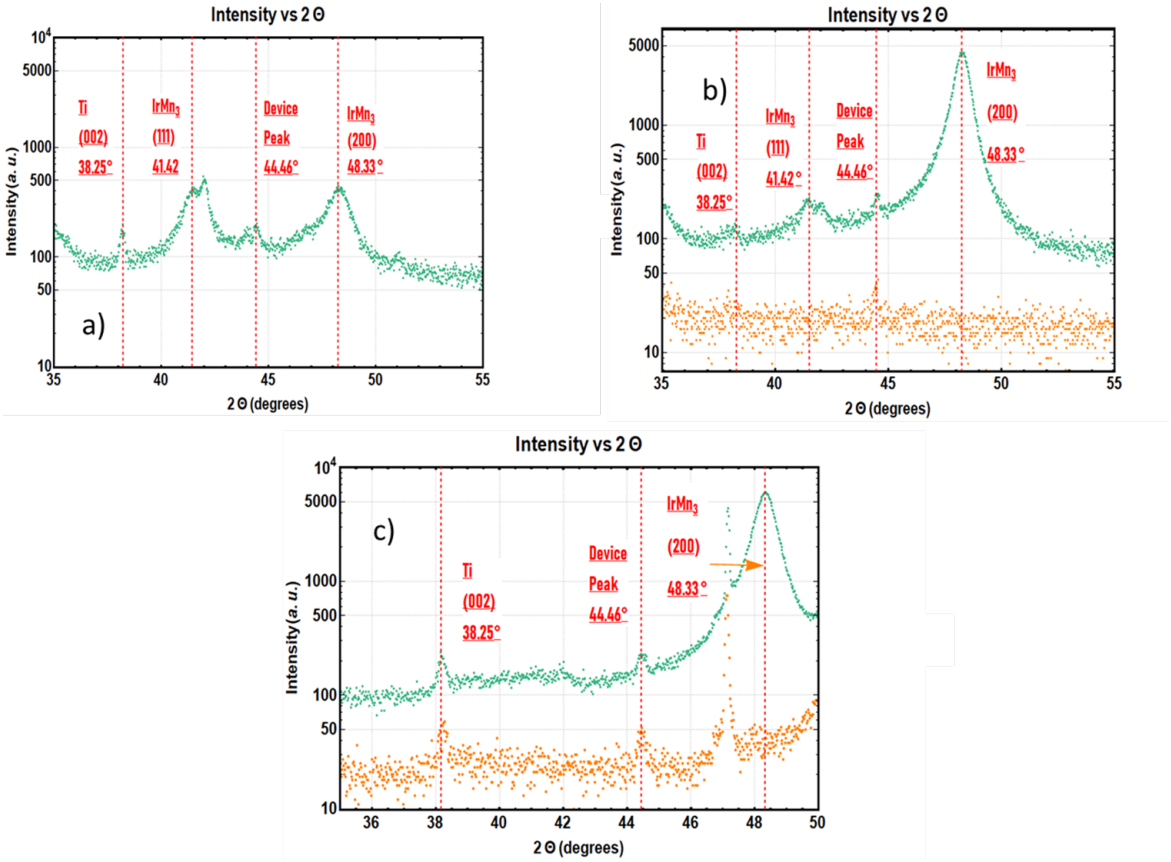

Figure 4.9. $IrMn_3$ XRD data on different substrates. (a) Amorphous Si/SiO_2, (b) M-cut Al_2O_3, (c) R cut Al_2O_3

4.2. Magnetic Characterizations

Measuring magnetic interactions requires decent knowledge on regular magnetic behaviour of the material being investigated. For this purpose, magnetic characterizations on FeMn and $IrMn_4$ were performed. This characterization gives clues on how strong and dominant AFM behaviour is on different thicknesses and temperatures. Vibrating Sample Magnetometer (VSM) technique is used for this task.

VSM measurement starts with mounting sample on mechanical system for vibrating, which is in vacuum and connected to PPMS system. Sample with magnetization creates a change in magnetic flux when performs an oscillation, which leads to electromotive force (EMF) when gathered up with coils. In VSM system, EMF induced current enhanced with a lock-in amplifier measured. This current is directly proportional to the magnetization of the sample, hence the more magnetized the sample is, more current it is obtained.

VSM measurement requires a magnetic layer for characterization of AFM materials.Coupling the AFM material with a FM material induces exchange bias,which leads to change in coercive field. In this work, magnetic calibrations are performed with a 5 nm $Ni_{81}Fe_{19}$ layer on top of AFM layer. For thickness depending VSM measurements, 5 nm NiFe layer is combined with various thicknesses of $IrMn_4$ and FeMn layers.

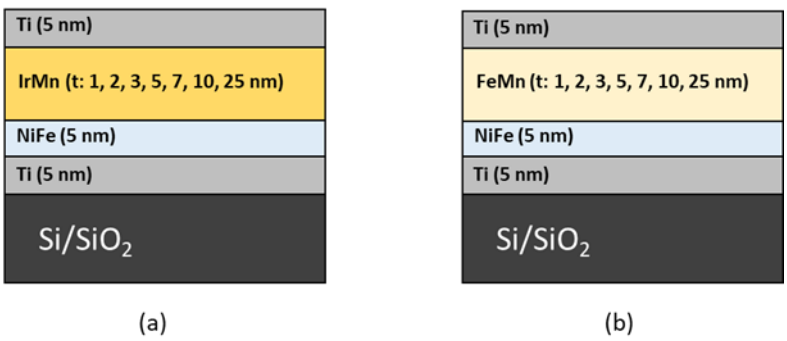

Figure 4.10. Samples prepared for VSM measurements.

What VSM measurements tell us about the magnetic behaviour depending on thickness and temperature of samples is based on important magnetic parameters, such as coercive field (H_C), exchange field (H_{Ex}) and blocking temperature. Before discussing the VSM data, it requires a decent understanding of these factors and their physical meanings. Exchange bias is an interfacial interaction between FM and AFM layer. Bilayer of FM/AFM invokes shift in magnetic hysteresis and this phenomena gives hints on many aspects. According to Meiklejohn-Bean Model [34], ideal exchange bias occurs when; FM layer rotates rigidly but AFM layer is magnetically tough and unresponsive, both of layers are in single domain state, FM/AFM interface is atomically smooth and AFM layer has in-plane uni-axial anisotropy. When all these factors are provided, it is expected to obtain an exchange interaction between uncompensated spins on AFM layer and FM layer interface, which alters the magnetic hysteresis behaviour of FM layer. As a result, observing the exchange bias behaviour is expected to show us how our AFM material behaves in various thicknesses and temperatures.

Temperature behaviour of AFM layers is another crucial step, since our field cooling experiments depend on reaching the required temperature for paramagnetic phase of AFM layer (Néel Temperature). While it is quite difficult to obtain (T_N) for all thicknesses, another important parameter blocking temperature (T_B) is also capable of giving us hints about this behaviour. Physically, uncompensated spins which provides the exchange interaction with FM layer, is affected by temperature as well. After reaching the T_B, no more exchange interaction thus H_C is expected to be observed. Due to this, it doesn't clearly show what T_N is for a given material, but makes an obvious statement about it should be higher than the T_B value.

H_C is the coercive field, which describes the extension in hysteresis behaviour of a magnetic material. Change in coercive field states how strong FM/AFM interaction is in given conditions. By using this parameter, it is possible to comment on how AFM behaviour trends change among different thicknesses and temperatures.As mentioned above, 5 nm $Ni_{81}Fe_{19}$ FM layer is used for this characterization. In order to understand the effect of AFM layer, first measurement should be a single 5 nm $Ni_{81}Fe_{19}$ layer measurement. By using this data, it can be obtained how temperature effects a constant reference layer of $Ni_{81}Fe_{19}$.

As it can be seen from Figure 4.11, temperature has negligible effects on $Ni_{81}Fe_{19}$ reference layer H_C behaviour. This statement show us any changes observed in temperature dependent VSM data for FM/AFM bilayers will be directly caused by trending AFM behaviour. As an introduction to other measurements for bilayers, here a detailed data for $IrMn_4$ and FeMn bilayers with 5 nm $Ni_{81}Fe_{19}$ is given below.

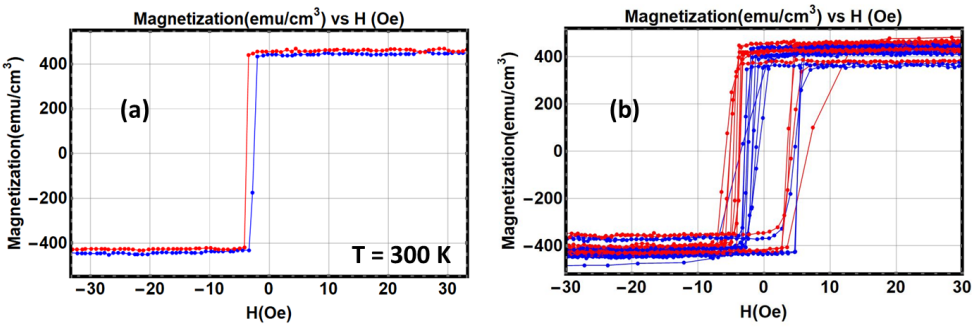

Figure 4.11. VSM measurements with reference 5 nm $Ni_{81}Fe_{19}$ layer. (a)Hysteresis in room temperature, (b)hysteresis behaviours in different temperatures.

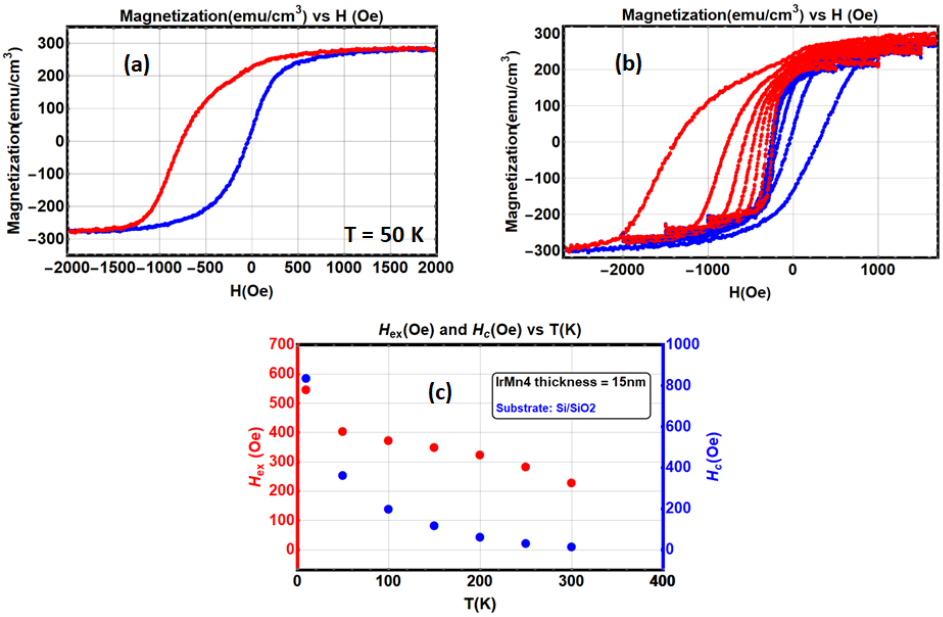

Figure 4.12. VSM measurement for $Ni_{81}Fe_{19}/IrMn_4$ stack. (a) Magnetization versus applied field hysteresis at 50 K (b) The same data for changing temperature (c) H_C and H_{Ex} values for each temperature for $Ni_{81}Fe_{19}(5)/IrMn_4(15)$.

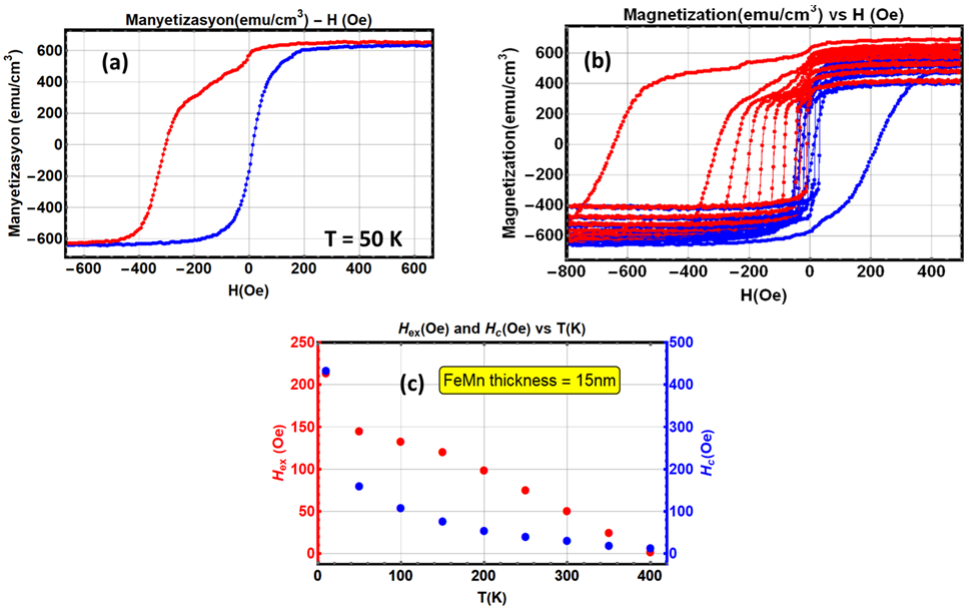

Figure 4.13. VSM measurement for $Ni_{81}Fe_{19}$ (5)/FeMn stack. (a) Magnetization versus applied field hysteresis at 50 K (b) The same data for with changing temperature (c)H_C and H_{Ex} values for each temperature for $Ni_{81}Fe_{19}(5)/FeMn$ (15).

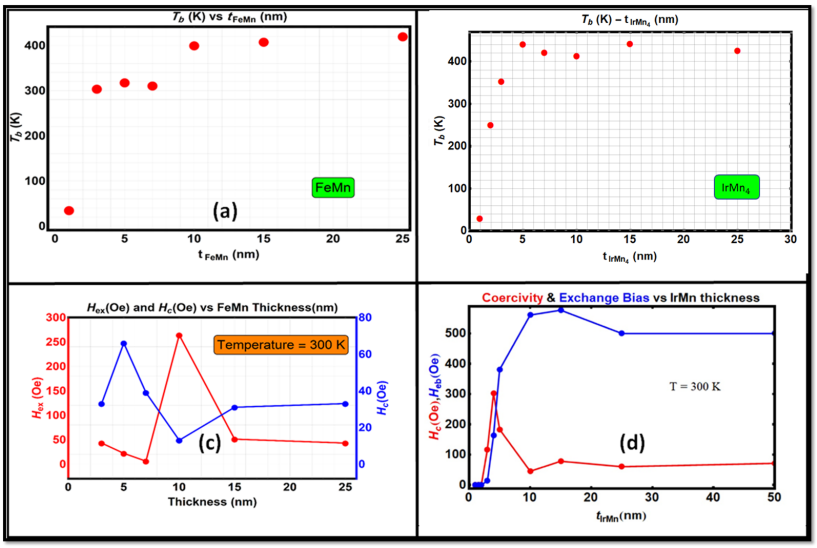

Figure 4.14. VSM results overview. (a) blocking temperatures for different thicknesses of FeMn (b) blocking temperatures for different thicknesses of $IrMn_4$ (c) changes in H_C and H_{Ex} of FeMn samples (d) H_C and H_{Ex} of $IrMn_4$ samples in an alternative representation.

4.3. Resistivity Measurements

Our study involves heavy investigations of resistance behaviour of various stacks of multiple material. It is expected to read resistance data and comment on changes with current injection and temperature alone with multiple influences such as magnetic field, field cooling and artifacts. Regarding this, before starting the bilayer and stack experiments, it is crucial to understand how materials conductivity behave under usual circumstances. Aiming this, all materials are put into regular electrical resistivity measurements with constant current but changing temperature, in order to figure out what to expect when each layer of device in introduced with current, which eventually creates an additional heating. These experiments help not only in this context but also give us hints about critical points that changes the trend of resistivity of each material. This way, it makes more sense to interpret the data we will have from field cooling experiments. Materials which will be used in structures are measured for their resistivity against increasing temperature. Figure 4.15 and 4.16 show the temperature behaviour for each individual material in two different thicknesses.

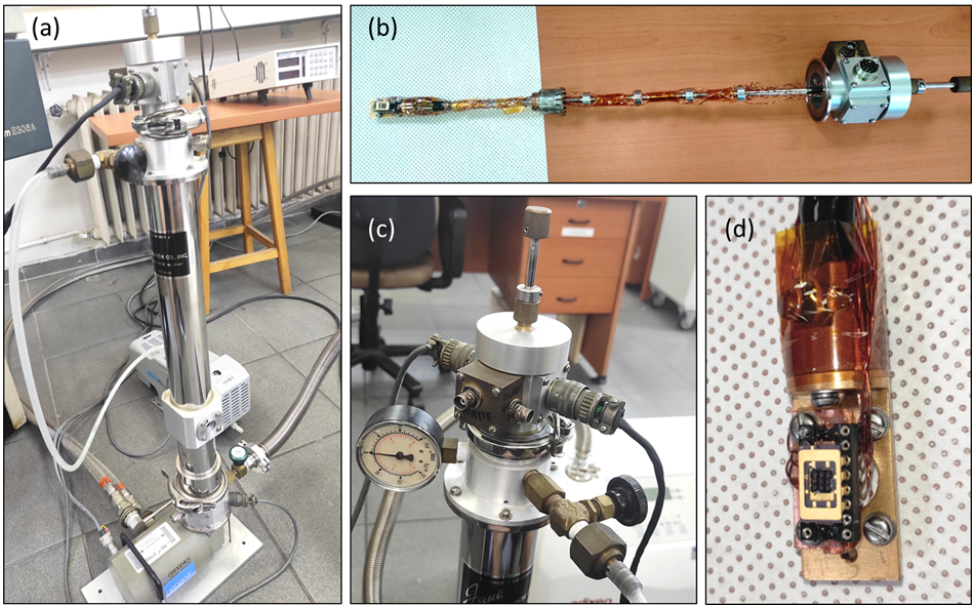

Figure 4.15. JANIS low temperature measurement system from different views; (a) JANIS cryostat. (b) Holder for inserting sample inside. (c) Electrical connections and pressure screen. (d) PCB insertion for measurements.

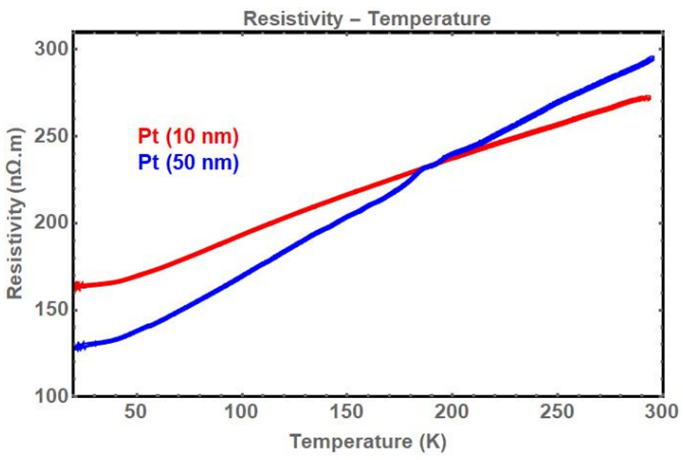

Figure 4.16. Resistivity measurement for Pt, red data for 10 nm and blue data for 50 nm.

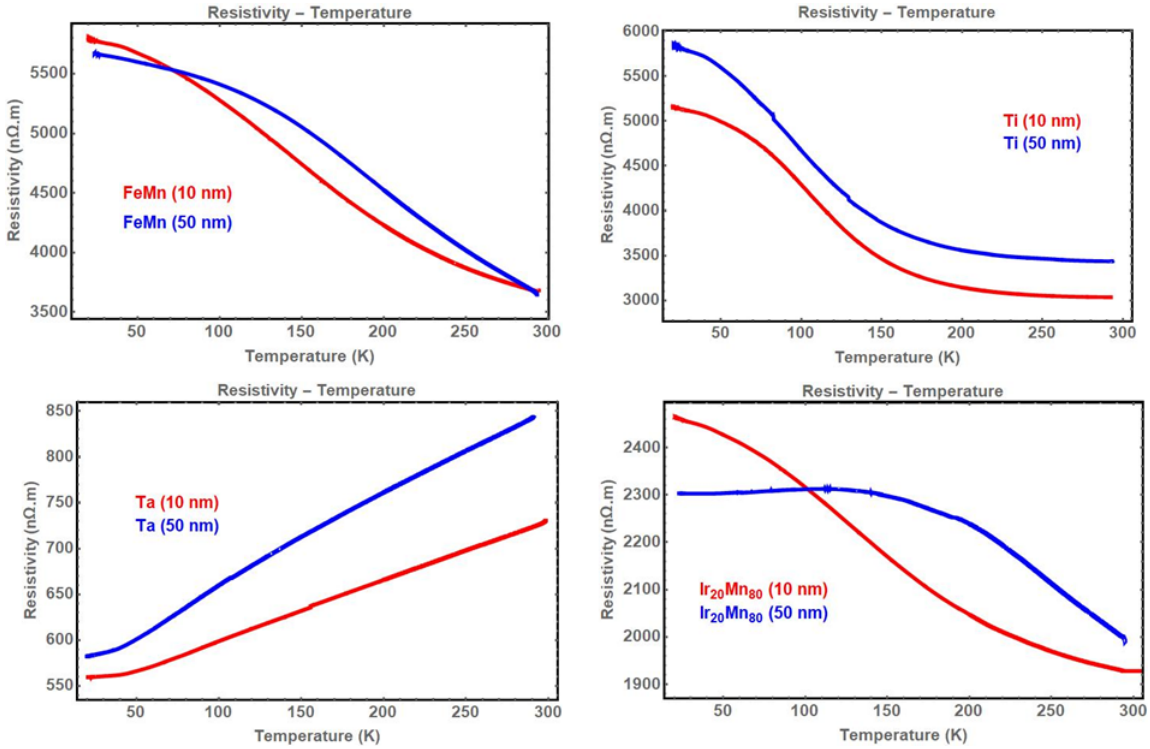

Figure 4.17. Resistivity measurement for Ta,Ti,FeMn and $IrMn_4$ red data for 10 nm and blue data for 50 nm.

4.4. Electro-Resistance Measurements

The aim of this project is to observe the SOT effect by using electroresistance measurements. These measurements are performed at 10K in order to enhance the torques applied to magnetic moments and decrease the overpowering thermal fluctuations. Electro-resistance measurement procedure starts with loading sample at 300 K to system. After that in order to make sure transforming magnetic phase of the sample to paramagnetic, system is heated up to 400K. 400 K is the limit for our experiment setup PPMS QD Dynacool system and presumably covers most of the sample's Néel temperature. Following the paramagnetic transition, 1 T of magnetic field in three different cases for each experiment is applied to sample while it is being cooled down to 10 K, where the current scan experiments are performed. During each case, it is expected to have an AFM material with a Néel order parameter influenced by applied external field. Magnitude of 1 T is qualified for this experiment, after performing same process with higher orders and observing that outcomes are same.

When the current scan for a single case in 10K is concluded, system is left to warm up until 300K and sample is measured for it's resistance versus temperature behaviour with 1 mA constant current. This move helps us to understand how the trends in current scan data related to samples' resistance behaviour influenced only with increasing temperature. During current scan at 10K, it is expected to observe heating effects on resistance. Having a resistance vs temperature data helps us to segregate that behaviour from only-magnetic fluctuations.

Another important data analysis is preparing a offset graph, which shows only the trend of current scan data. This analysis helps us to figure out amount of decrement and trend, instead of current scan data, since initial values of resistance may change depending on various reasons during experiment, such as artifacts, contact damage, current and heating damage. Considering the full scope of experiment consists measuring the same sample in three different cases with three different field cooling, this method is crucial to understand trend of resistance instead of focusing only the amount of resistance change from start to end value.

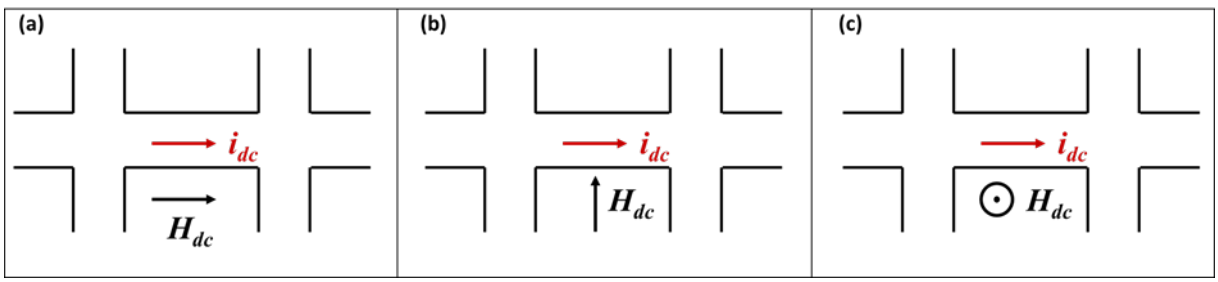

Figure 4.18. Three different cases of field cooling the Hall bars. (a) Parallel to the injected current. (b) In-plane perpendicular to injected current. (c) Out-of-plane perpendicular to injected current.

After completion of measurement for one case, Hall bar structures are rotated by either using the rotator bar (from first case to second case) or by extracting sample from in-plane PCB and assembling it to out-of-plane PCB.

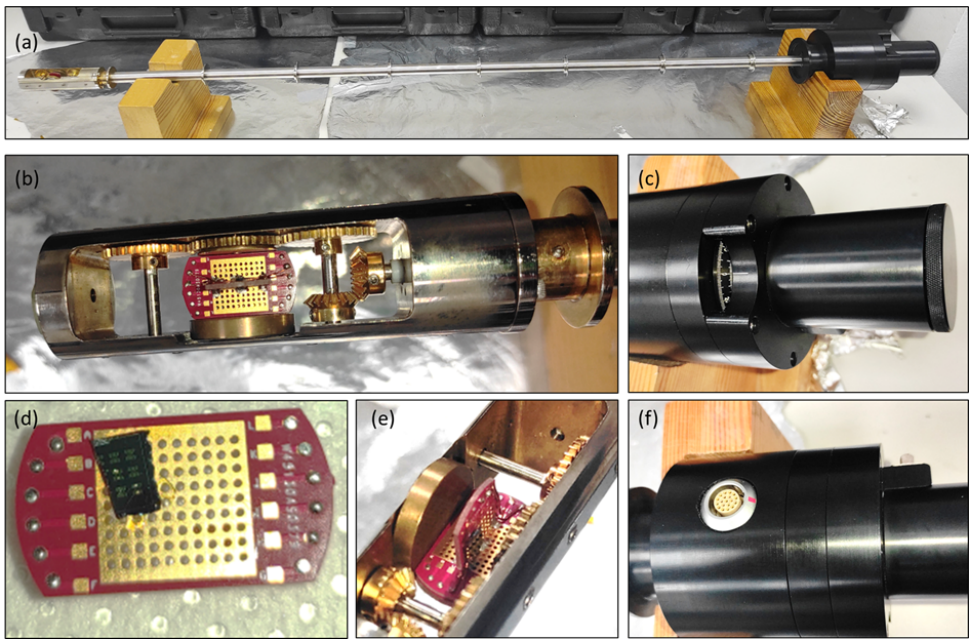

Figure 4.19. Rotator system elements. (a) Rotator bar. b)Mounting in-plane PCB on rotator. (c) Controlling head of rotator with rotating angle adjustment. (d) Sample on out-of-plane PCB. (e) In-plane sample mounted on rotator. (f) LEMO power plugs.

4.4.1. Important Points of Electro-resistance Measurements

4.4.1.1. Compliance Problem. Compliance describes the Voltage limit for the current source. In our experiment setup, our power source is limited with 40 V of applied volts. From very basic ohms law we know,

$$V = I \cdot R. \tag{4.1}$$

This compliance limit can be reached by applying high amount of current into a highly resistive sample. When $I \cdot R$ value reaches the 40V level, system breaks down the measurement and reduces current as an electrical fusing mechanism. This is another important factor for optimizing the applied current to samples.

4.4.1.2. Exact Current Applied from Source. Curren source should be set up correctly with predestined parameters. Keithley 2440 power source is used both as source and measurement device. In this study, we perform two-probe measurements with 40 V compliance limit. Arranging the parameters is crucial, when the current is injected from source it can vary in extended digits. As an example, when it is set as 1 mA applied current, in the power source screen it might be seen as 0.9999 mA. This is not a big issue in measurement, but with the increasing volume of applied current, there might be spikes and misconducted experiments.

4.4.1.3. Heating of Sample. Electro-resistance measurements involve injecting current with a maximum possible current density in order to enhance SOT effect. In the sample array, 9 Hall bars with different widths are located. Considering their base resistance, which has the parameters of resistivity (ρ), area normal to injected surface (A) and length of the Hall bar (L). All Hall bars have the same longitudinal length, hence we won't be discussing this parameter on heating effects. What makes the difference is the A value, which is basically multiplication of width of Hall bar (w) and height of the sputtered sample (h).

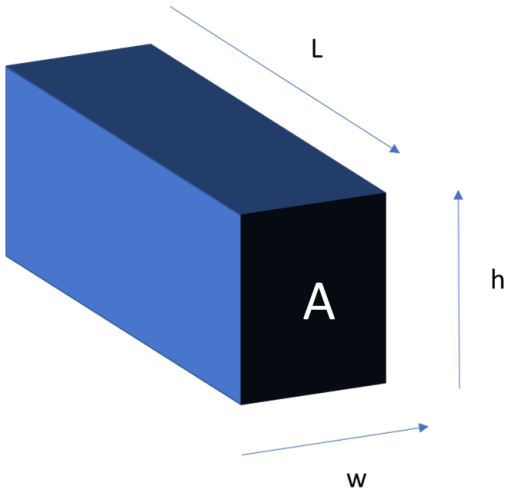

Figure 4.20. Schematic drawings of a cut prism to inject current. h is the height, L is the longitudinal length and w is the width. A is the area of surface that a current to be injected into.

We know the very primitive resistance relationship

$$R = \rho \frac{L}{w.h}, \tag{4.2}$$

where the R is the resistance and ρ is the resistivity of sample, it is safe to say narrowing the width of Hall bar will gradually increase the resistance. Another fundamental physical law, law of Joule heating states that the more resistance material have,the more heat will occur in system as the dissipation,which changes the transport properties of material. In the equation below, heating of a resisting sample by current injection is given

$$P = I \cdot R^2. \tag{4.3}$$

Depending on the Joule heating relationships given in Equation 4.3 and 4.4,where P is the power generated, I is current, R is resistance and Δt is change in temperature. As can be seen from mathematical relationship, heating of the sample increases by the square of resistance value. Considering this, optimizing these parameters for reliable measurement and data is crucial;

$$Q = P \cdot \Delta t. \tag{4.4}$$

4.4.1.4. Preventing Electrical Spikes. Experiment setup consists a power source (Keithley 2440) connected to measurement rod through make-before-break switches. This mechanism prevents an instant voltage peak to damage the sample during the start of the measurement. This mechanism consist of two switches placed in a box. One switch is for voltage drop and other one for current drop. At the initial condition, both of the switches should be turned off. This means neither voltage nor current will be able to be induced or pass through the primitive circuit. When the power supply is activated, voltage switch is turned on while current switch remains of. This means inducing voltage in a short-circuit to absorb a potential instant voltage peak from source. After few seconds of turning on voltage switch, now it is safe to send current to the sample measurement system, with instant-peak-free fashion.

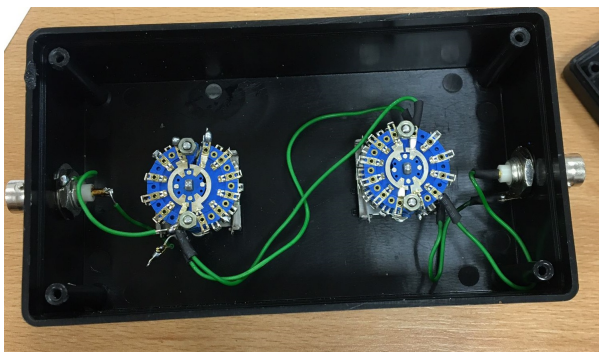

Figure 4.21. Make-before-break switch. Two rotary switches are used, first one is for voltage drop, second one is for creating short and disabling the current.

5. EXPERIMENTS AND RESULTS

Final stage of our studies are experiments and discussion of outcomes. In the section 4.4, electro-resistance experiments are fundamentally explained and analyzed. In this section, each set of sample groups with their theoretical expectations are covered. For each set, many parameters are taken into account for analyzing results, such as current density, initial sample resistance, correlation with calibrations and simulations and experiment conditions.

Field cooled electro-resistance measurements are started with [AFM/HM] bi-layer structures. In the first section, measurements of [HM/$Fe_{50}Mn_{50}$] and [HM/$IrMn_4$] is given. Samples are deposited on Si/SiO_2 substrate. Before the AFM layer, 0.5 nm of Ti layer is sputtered as adhesive layer. On top of HM layer, another 3 nm of Ti layer is sputtered for avoiding oxidation of HM layer. During bi-layer experiments, main goal was to observe the signs of SOT in different thicknesses to decide which thicknesses of AFM layers to be used in further experiments. Previous works on SOT detection by electro-resistance [24] show there is a different R vs I behaviour in three different FC scenarios when current scan is performed.

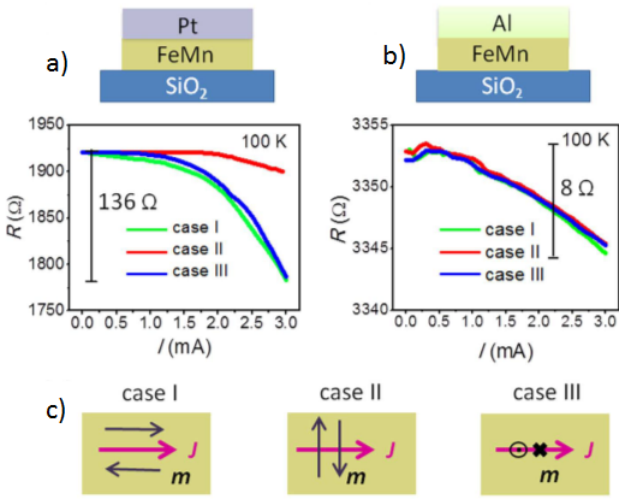

Figure 5.1. Comparative study on HM/AFM bilayer for (a) Pt as HM layer with high-SOC, (b) Al as HM layer with low-SOC on $Fe_{50}Mn_{50}$. AFM layer shows the differences in current scan trends. (c) Schematics for field cooling process.

In Figure 5.1 , electro-resistance measurements at 100K points the difference of two structures, FeMn coupled with a high-SOC layer Pt, and FeMn coupled with a low-SOC material Al. This study shows that, expected pure spin current accumulation from HM layer induces SOT and creates differences when current scan is performed. Data from Figure 5.1a) section show the current scan for three different field cooling cases. As it can be seen, when the injected pure spin current aligns somehow perpendicular with AFM layer, change in electroresistance increases dramatically. When the pure spin current aligns parallel to Néel order, there will be no torque applied on magnetic moments and change in resistance will be lower.

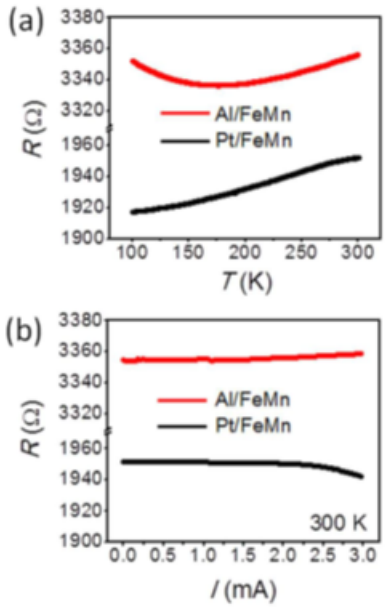

Figure 5.2. (a) Resistance versus temperature behaviour of two samples in the interval of field cooling process. (b) Current scan at the upper limit of field cooling process, in order to compare the trend to low temperature field cooling trends.

In order to address the thermal effects, it is also important to include resistance behaviour on increasing temperature, to understand how sample will behave under the condition of increasing temperature with current injection. Differences in resistance trends can be identified as magnetic effects. Yet another important parameter is the temperature of current scan process. Comparing current scan data in two different temperatures gives hint about magnetic nature and another aspect for temperature behaviour comparison.

In Figure 5.2, temperature and current scan data is given. By using this, it is possible to understand how a current scan would look like for both experiments in 300 K and how samples behave on increasing temperature between the limits of field cooling.We aim a similar approach, where we compare the differences between 10 K current scan data and trends in temperature scan for identification of magnetic events.

5.1. Experiments on Bilayer Structures

Electro-resistance measurements were started with bi-layer structures. First goal to achieve was to obtain the correct thickness for SOT measurements and optimize the current injection parameters. Field cooling process has been discussed in Section 4.4. The main strategy is to understand thickness dependence of of AFM layer in SOT detection. In previous studies [24], a similar structure has been investigated with their thickness dependence of HM layer, hence in this study it is preferred to use 2 nm of Pt and 4 nm of Ta as HM layers. Regarding magnetic characterizations, it is also shown that for $Fe_{50}Mn_{50}$ thickness values will be 3, 5 7 and 10 nm, for $IrMn_4$ samples, thicknesses will be 1,1.5,2 and 3 nm. By using data from bi-layer experiments, it will be investigated for each thickness if it is possible to observe signs of SOT in current scan data.

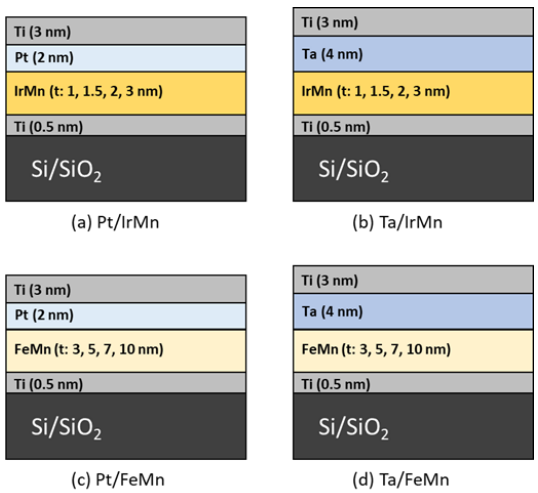

Figure 5.3. Schematic of bilayer structures of (a) and (b) $IrMn_4$, (c) and (d) $Fe_{50}Mn_{50}$.

5.1.1. $Fe_{50}Mn_{50}$ Bilayer Experiments

First set of experiments are FeMn bilayer experiments. First data from different thicknesses of FeMn bilayers have taken with our previous experiment setup. After progressing our set up, we have repeated our prospect measurements from first experiments and achieve similar results with two samples.In Ta(4)/FeMn(5) sample, it is possible to observe SOT-like behaviour of offset-current scan with the increasing current density. Using this fact, further studies on FeMn structures are performed with 5 nm of FeMn AFM layer.

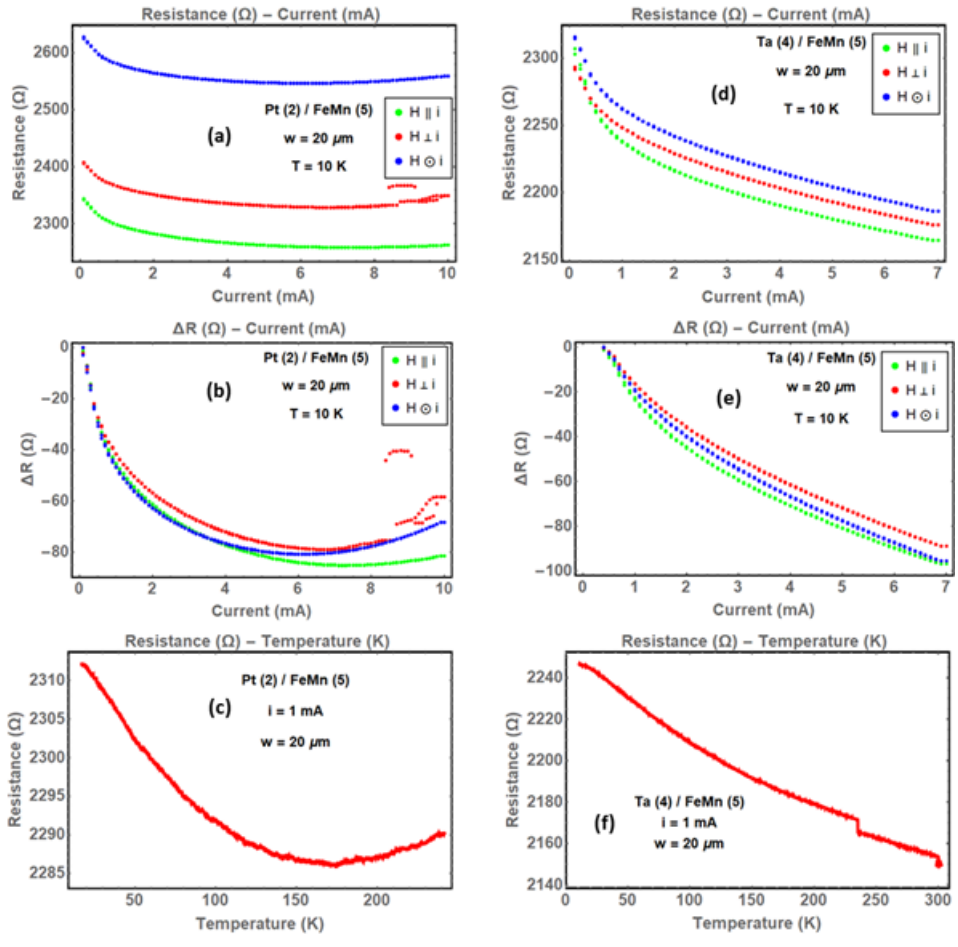

Figure 5.4. Current scan data from FeMn bilayer samples with different HM layers with $t_{FeMn} = 5$ nm. .

Green data shows field cooling parallel to applied current (case I), red data shows field cooling in-plane perpendicular to applied current (case II) and blue data shows field cooling out-of-plane applied current (case III).

5.1.2. $IrMn_4$ Bilayer Experiments

In this section, $IrMn_4$ AFM layer is investigated for two HM layers with different spin Hall angles and different signs. Studies show Pt has positive spin Hall angle and $IrMn_4$ and Ta has negative spin Hall angle [35–37]. Considering this, one should expect differences in magnetic interactions. These interactions may not be visible enough in bilayer experiments, but it is safe to say there will be hints to lead investigation for further multi-stack structures.

5.1.2.1. Pt/$IrMn_4$ Experiments. $IrMn_4$ bilayer studies started with Pt HM layer. Pt layer is known with its high and positive spin Hall angle [35] which is opposite to the $IrMn_4$ with negative spin Hall angle [36]. Expected polarization scenario and data for 10 K current scan, offset va lues of current scan trends and resistance vs temperature data is given below. Data from this set of experiments has shown that when the $IrMn_4$ layer is 1.5 nm, electro-resistance behaviour of sample shown signs of SOT effect. Regarding this, further investigation for tri-layer and multi-stack structures have been performed with $IrMn_4$ 1.5 nm AFM layer. In the Figure 5.5, lean current scan data is given for $IrMn_4$ samples. When the changes in resistance values plotted in Figure 5.6, very promising result for 1.5 nm $IrMn_4$ samples is achieved.

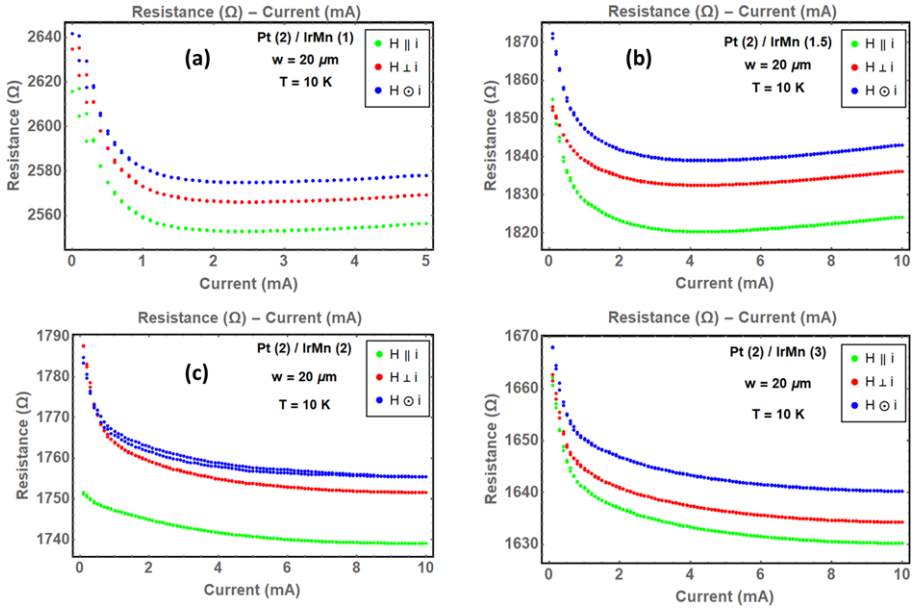

Figure 5.5. Current scan data from Pt/IrMn samples with (a) AFM Thickness is t_{IrMn_4} = 1 nm, (b) 1.5 nm, (c) 2 nm, (d) 3 nm green data shows field cooling parallel to current (case I), red data in-plane perpendicular (case II) and blue data out-of-plane to current (case III).

As it has been expected, first and third case acts similar while second case resistance drop is way more smaller than other two. Considering this achievement, thickness for $IrMn_4$ stack experiments is decided as 1.5 nm. When compared to resistance versus temperature data, it can be seen the lowest point of current scans is lower than temperature data, which means there is an effect which drops resistance more than temperature related effects, which is an addition to them.

Another important sign of magnetic effects is the change of temperature trend in current scan data, which gives hint about these two mechanisms' effect on resistance don't alter the behaviour similar. A sharp dip behaviour is in contrast with curvature trend occured increasing current in current scan. Clarification of this effect can be solidified by performing an another current scan in resistance dip value and check if the signs of the SOT effect is compatible with physical properties. When the temperature is increased, it is expected to observe current scan to shift in going forward and back data points, with smaller amount of resistance drop in same sample. As it can be seen in Figure 5.8, required behaviours are observed in given parameters.

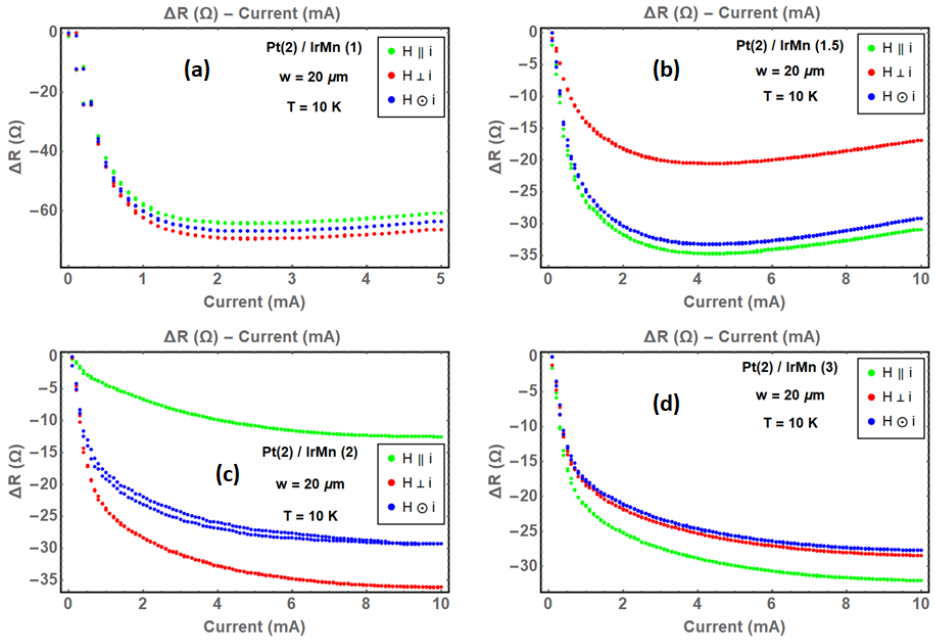

Figure 5.6. Change in resistance fit for (a) AFM Thickness is t_{IrMn_4} = 1 nm, (b) 1.5 nm, (c) 2 nm, (d) 3 nm green data shows field cooling parallel to current (case I), red data in-plane perpendicular (case II) and blue data out-of-plane to current (case III).

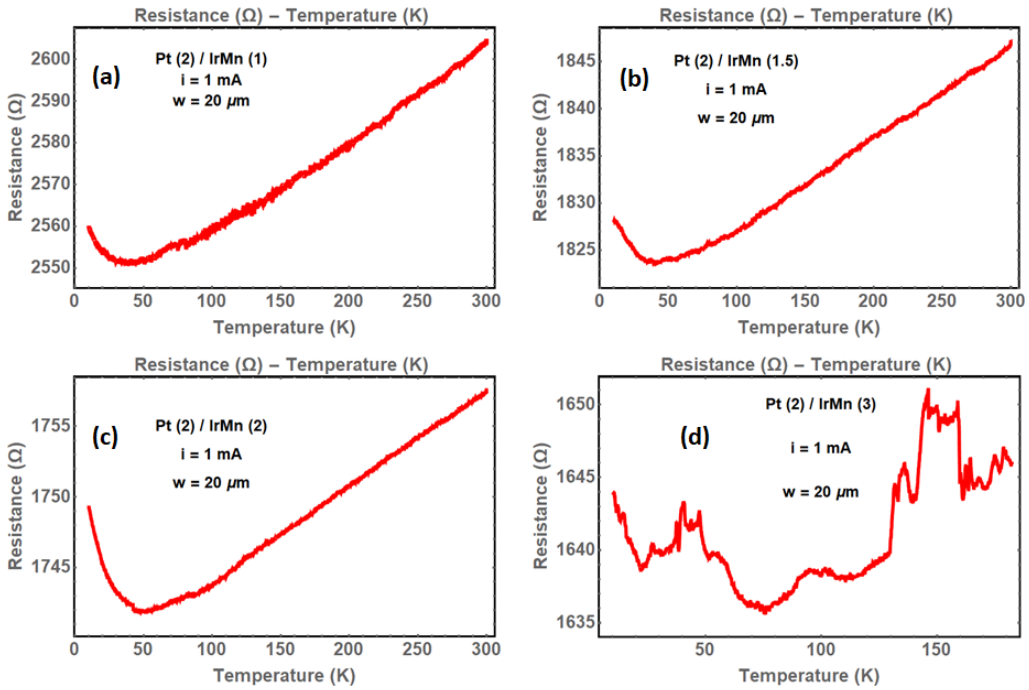

Figure 5.7. Change in resistance with rising temperature for each thickness of t_{IrMn_4} samples. (a) t_{IrMn_4}=1 nm (b) 1.5 nm (c) 2 nm (d) 3 nm.

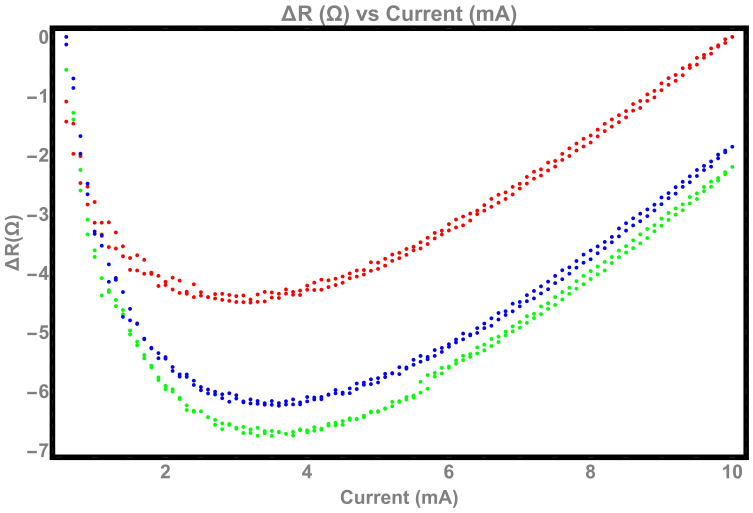

Figure 5.8. Cases fitted and offset depending on their amount of resistance drop for Pt(2)/$IrMn_4$(1.5) sample at 40 K where resistance makes a dip at temperature scan.

5.1.2.2. Ta/$IrMn_4$ Experiments. Following the studies [35, 37], Ta has a remarkably smaller spin Hall angle compared to Pt with opposite sign. When used as HM layer with $IrMn_4$ it is expected to observe smaller magnetic effects compared to Pt layer, due to both having same spin Hall angle with $IrMn_4$ and considerably weaker charge to spin conversion.

When the data in Figure 5.9 and 5.10 is analyzed, no significant effect related to SOT can be observed. This is the actual case to be expected, since no interaction between AFM spin lattice and pure spin current is assumed to occur.Figure 5.10 shows AFM thickness effects the initial resistance value of samples, so do change in resistance. When Figure 5.10a and 5.10b is considered, 1 nm of $IrMn_4$ may not be capable of forming a reliable conduction environment as a AFM heavy metal. Hence, neglecting the 1 nm case, change in resistance decreases while $IrMn_4$ thickness increases.

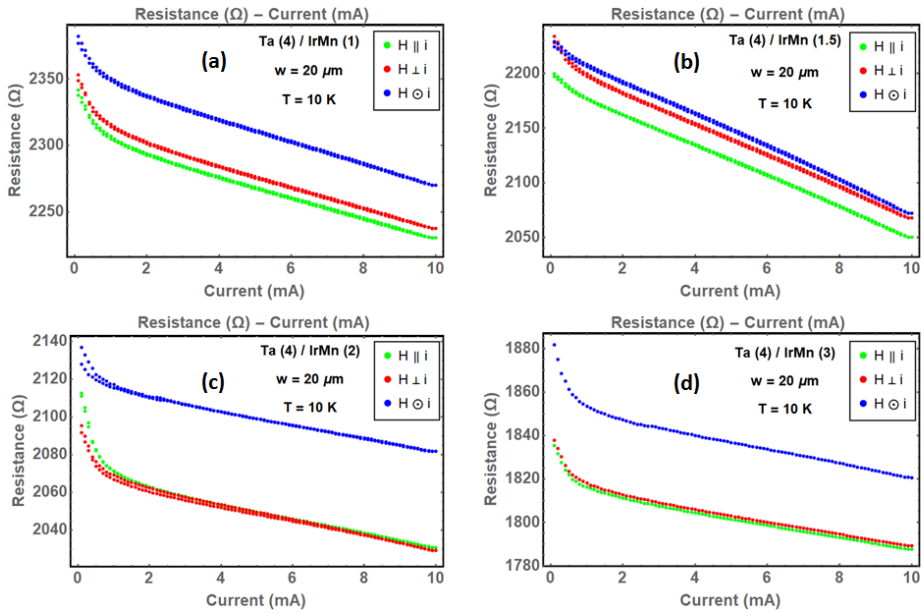

Figure 5.9. Current scan data from Ta/$IrMn_4$ samples with (a) AFM Thickness is t_{IrMn_4} = 1 nm (b) 1.5 nm (c) 2 nm, (d) 3 nm.

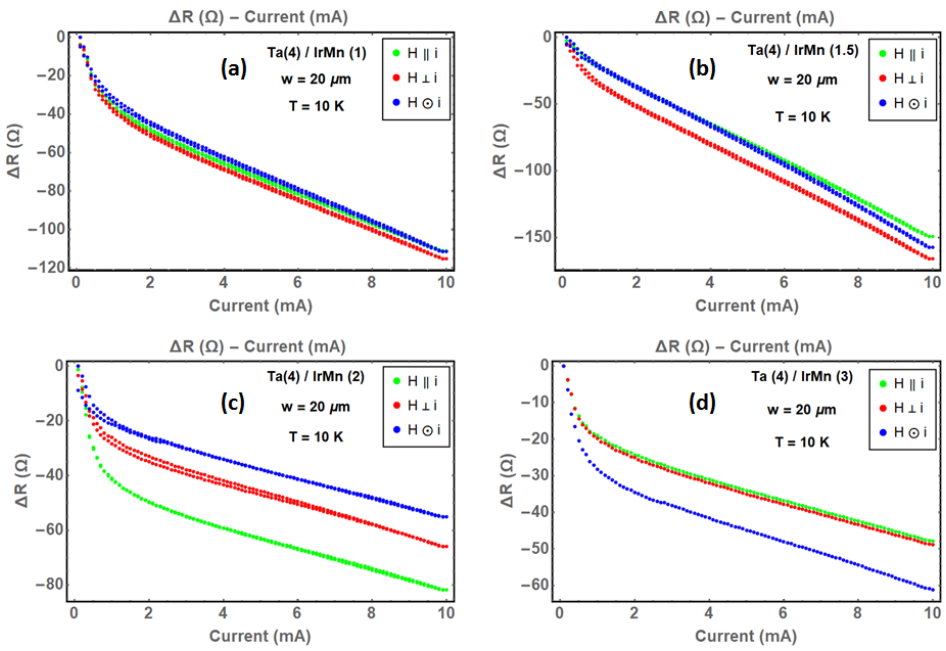

Figure 5.10. Change in resistance fitted for (a) AFM Thickness is t_{IrMn_4} = 1 nm (b) 1.5 nm (c) 2 nm , (d) 3 nm.

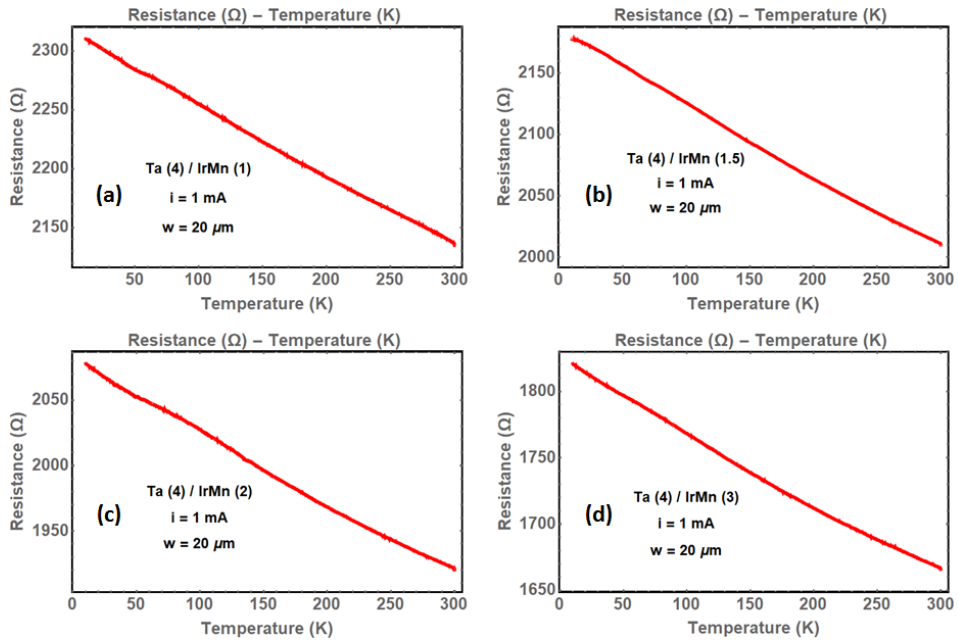

Figure 5.11. Change in resistance with rising temperature for each thickness ofTa/$IrMn_4$ samples. (a) t_{IrMn_4}=1, (b) 1.5 (c) 2 (d) 3 nm.

5.2. Experiments on Trilayer Structures

In this phase of our study, our aim is to investigate the idea of overlapping the pure spin currents injected into AFM layer from top and bottom HM layers. Here, promising physics offers enhancing the SOT effect by two layers of HM, one at the top and one at the bottom of AFM layer, by engineering a structure as injected pure spin currents to be having the same polarization and increase the torque on AFM layer. If occurred, change in magnetization of AFM layer would expected to be greater when compared to bi-layers, thus greater change in resistance could be realized.

This would require three different so called " Sandwich layers" for each AFM material, sandwiched of two HM layers. Layers on top and bottom will be changed, in order to observe the effect of spin Hall angle magnitude and sign of HM layers. Given in Figure 2.14, correct sandwich structure would induce a magnetization on AFM layer as collection of two pure spin currents in the same direction, which would enhance the change in resistance. This magnetization would invoke a greater torque on AFM layer which leads to a greater change in resistance measurement. In tri-layer samples, t_{IrMn_4} is chosen to be 1.5 nm and t_{FeMn} is chosen to be 5 nm.

5.2.1. $Fe_{50}Mn_{50}$ Trilayer Experiments

In this section, discussion of current scan experiments with AFM layer 5 nm $Fe_{50}Mn_{50}$ between two HM layers is given. In the bi-layer section, it can be seen that for Ta(4)/$Fe_{50}Mn_{50}$(5) data is a good prospect for SOT signs. Since self torque mechanism in $Fe_{50}Mn_{50}$(5) is negligible, assumption of interface magnetization of layers overlaps and increase the torque oh AFM layer, since spin currents injected from top and bottom suppose to cancel each other out. Not only the self torque mechanism, but also spin relaxation and spin diffusion length in FeMn layers makes it even more difficult to obtain magnetization manipulation in AFM layers by magnetization induced by spin-orbit torque.

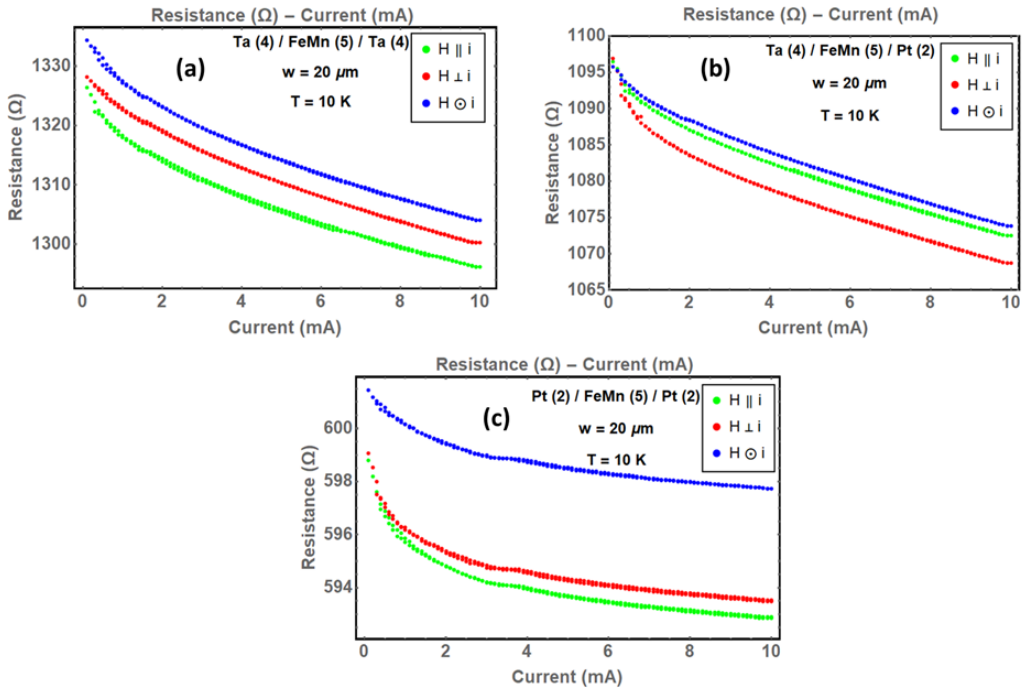

Figure 5.12. Current scan data from $Fe_{50}Mn_{50}$ tri-layers; (a) Ta/$Fe_{50}Mn_{50}$/Ta, (b)Ta/$Fe_{50}Mn_{50}$/ Pt (c) Pt/$Fe_{50}Mn_{50}$/Pt.

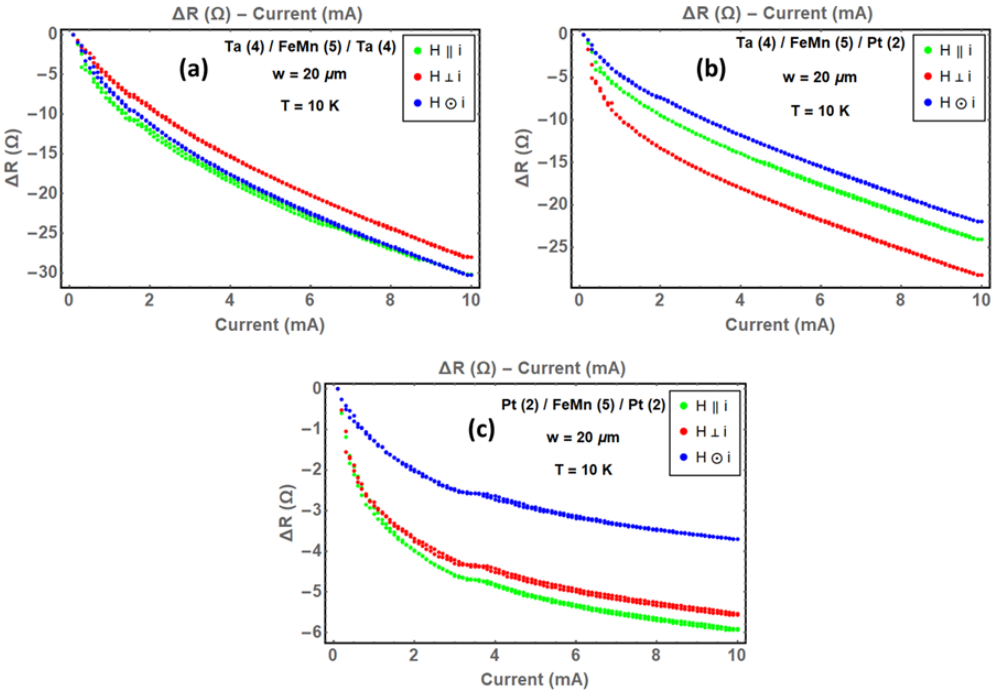

Figure 5.13. Current scan offset data from $Fe_{50}Mn_{50}$ tri-layers; (a) Ta/$Fe_{50}Mn_{50}$/Ta, (b)Ta/$Fe_{50}Mn_{50}$/ Pt (c) Pt/$Fe_{50}Mn_{50}$/Pt.

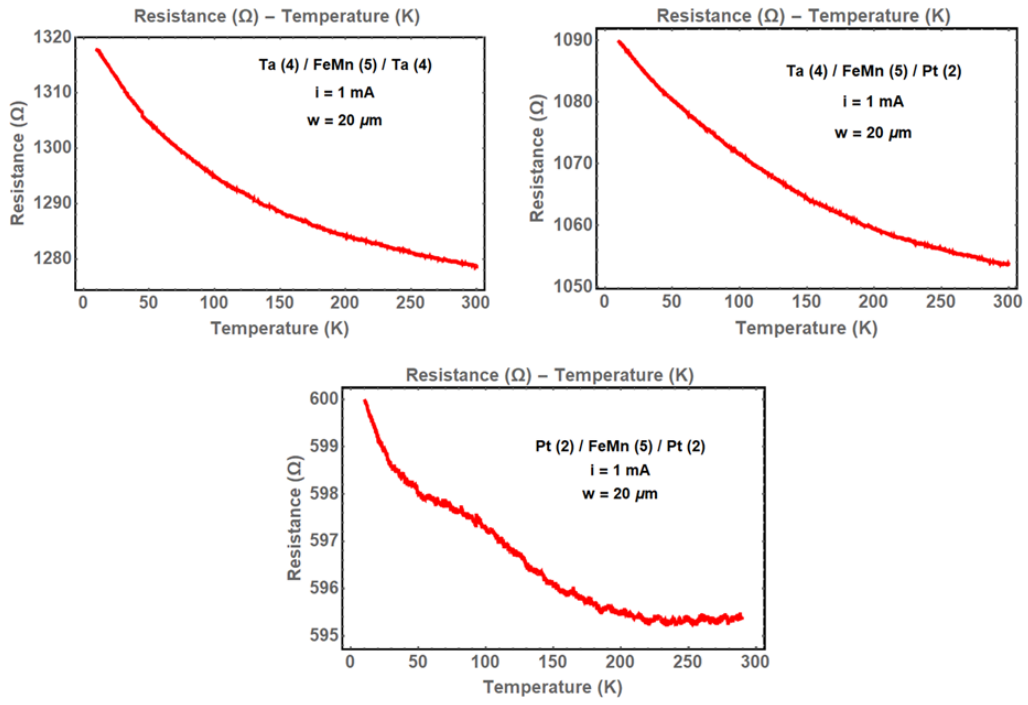

Figure 5.14. Resistance behaviour of samples with increasing temperature (a)Ta sandwich, (b)Ta/Pt,(c)Pt sandwich.

5.2.2. $IrMn_4$ Trilayer Experiments

Second part of tri-layer experiments performed with 1.5 nm $IrMn_4$ layer. Same procedure with $Fe_{50}Mn_{50}$ is applied. An additional sample without a HM layer is also included on this study, in order to observe the self-torque of $IrMn_4$. This way, it would make more sense to compare the additional layers and their effects on resistance change. In Figure 5.15a, it is possible to observe a slightly SOT-like behaviour of Ti(3)/$IrMn_4$ sample when a current scan performed. Layers with different spin Hall angles with different signs makes a more crucial appearance here, since $IrMn_4$ also has it's own torque when current is injected. This effect can manipulate all physical scenario when current is introduced.

Another important notice here can be observed from temperature dependent measurements. As we can wee from previous temperature data, Pt layer is quite dominant in resistant versus temperature behaviour of its bilayer samples. When the data for trilayers taken into account it seems Pt characteristic is no longer dominant in data. This can be caused by both reduction of injected current into Pt layer or exclusive behaviour of the trilayer structure.

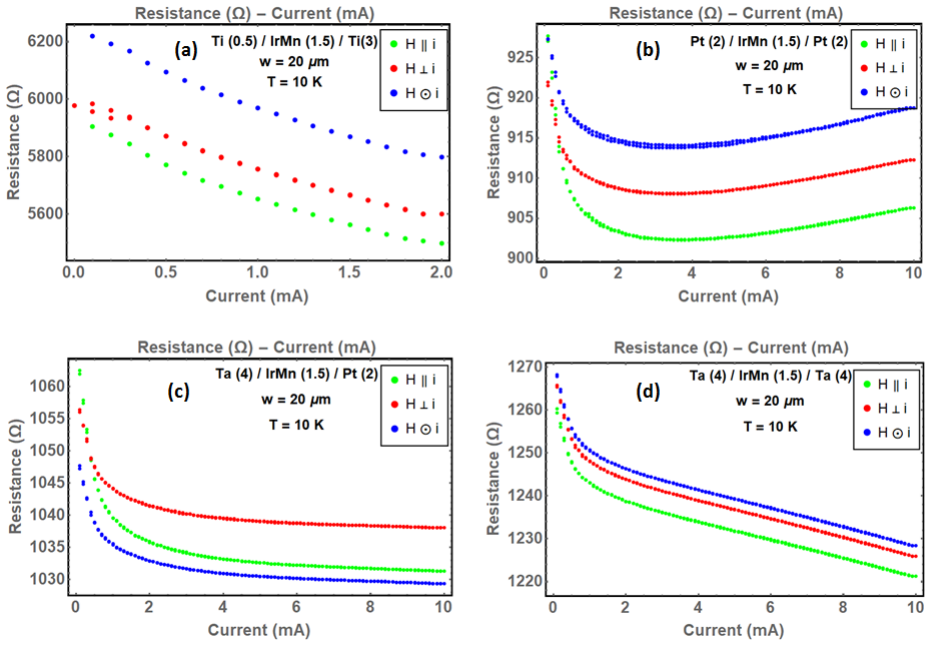

Figure 5.15. Current scan data from $IrMn_4$ tri-layer samples. with different HM combinations. (a) $IrMn_4$ without HM layer (b) Pt/$IrMn_4$/Pt, (c) Ta/$IrMn_4$/Pt , (d) Ta/$IrMn_4$/Ta.

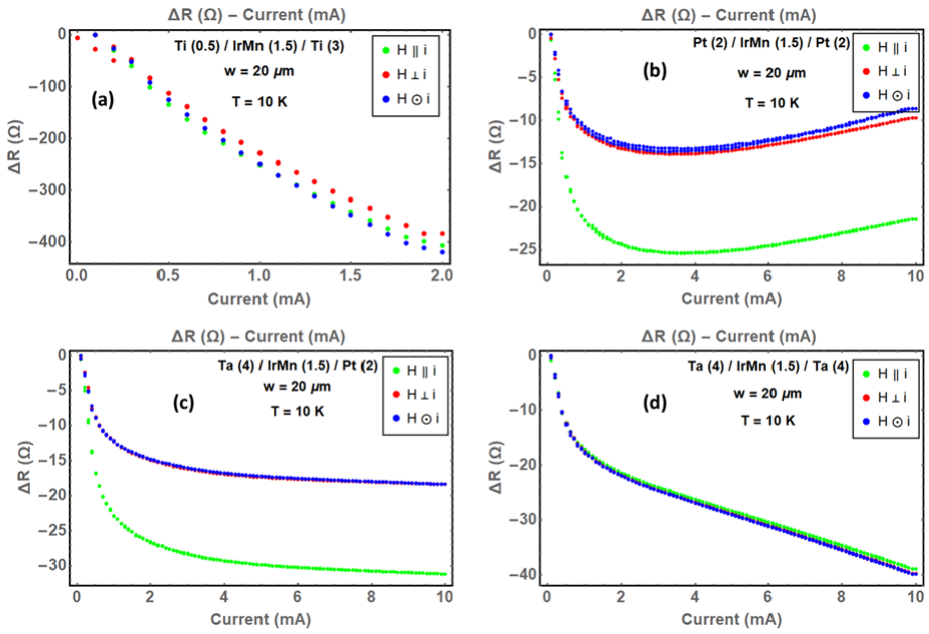

Figure 5.16. Offset current scan data from $IrMn_4$ tri-layer samples. with different HM combinations. (a)$IrMn_4$ without HM layer (b) Pt/$IrMn_4$/Pt, (c) Ta/$IrMn_4$/Pt , (d) Ta/$IrMn_4$/Ta.

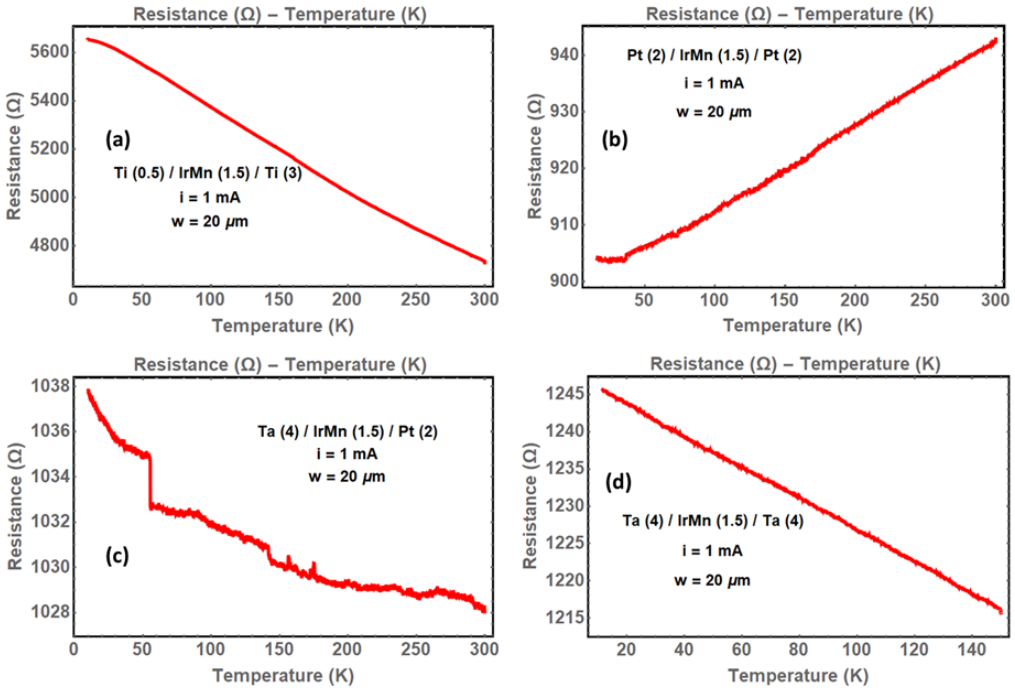

Figure 5.17. Temperature scan data from $IrMn_4$ tri-layer samples. with different HM combinations. (a)$IrMn_4$ without HM layer (b) Pt/$IrMn_4$/Pt, (c) Ta/$IrMn_4$/Pt , (d) Ta/$IrMn_4$/Ta.

5.3. Multistack Experiments

As the third and the final part of our study, number of repeats are increased. In order to test the expected physic of tri-layer structure Ta/AFM/Pt, which is expected to give rise to greatest effect due to HM layer SHE properties, three recursive stacks are investigated. This recursion in the stack is denoted to keeping each AFM layer between Pt and Ta layers, with an alternating fashion.

5.3.1. FeMn **Multistack Experiments**

We have studied the electroresistance behaviour of multistacks with Ta/FeMn/Pt repeats.As it can be seen below, the more repeat we add, lesser resistance sample will have, thus it will be even harder to identify magnetic effects. When we look a at the last stack, the triple repeat sample, it can be easily seen that current scan causes only a few ohms of difference in resistance. However, it is still promising to observe the trends of resistance in rising temperature still not the same with current scan data, which is a prospect of an additional effects caused my magnetic manipulation.

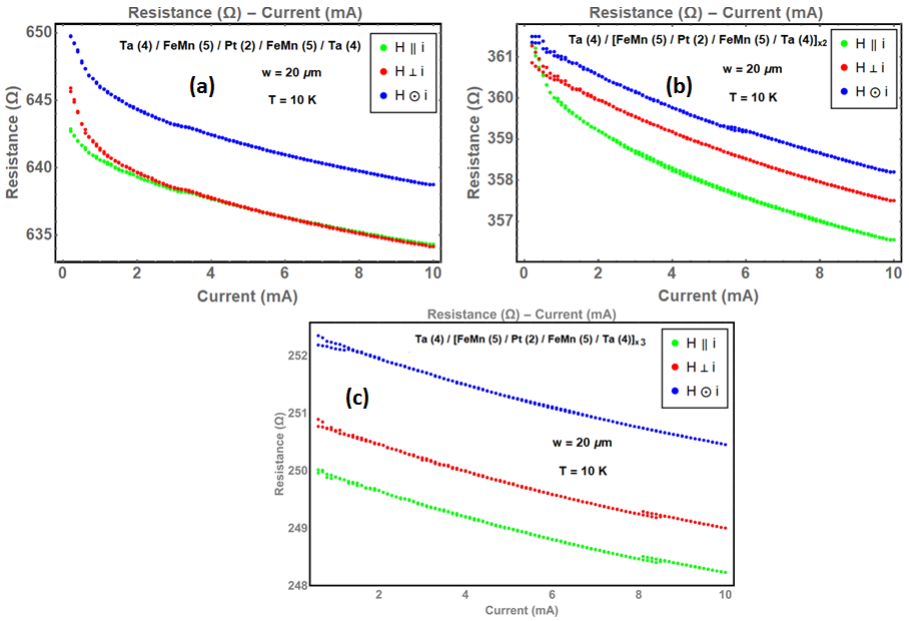

Figure 5.18. Current scan data from FeMn multi-stack samples. (a) Single repeat of Ta/FeMn/Pt stack (b) Double repeat of Ta/FeMn/Pt stack (c)Triple repeat of Ta/FeMn/Pt stack.

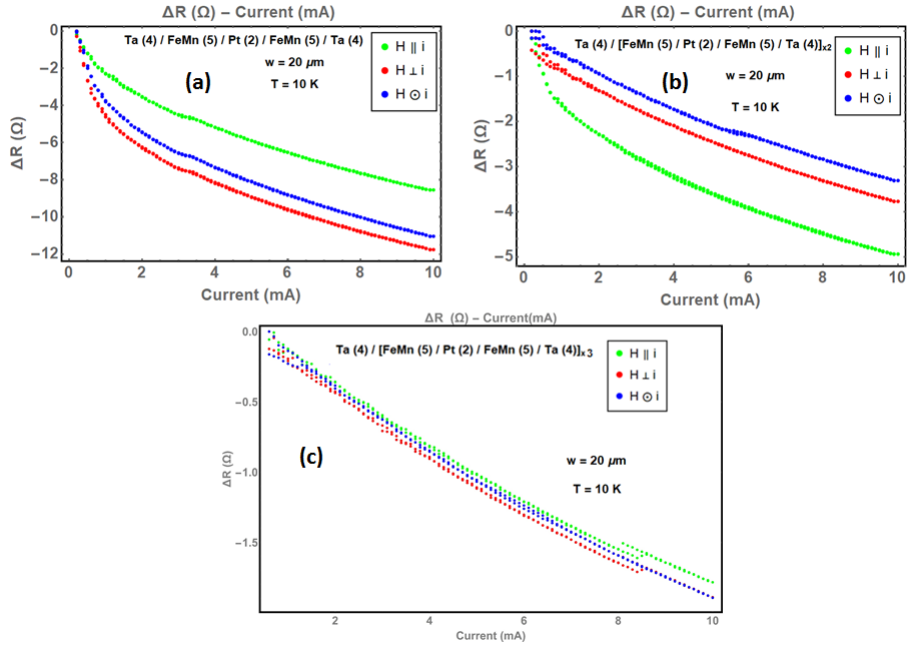

Figure 5.19. Current scan data fit from FeMn multi-stack samples. (a) Single repeat of Ta/FeMn/Pt stack (b) Double repeat of Ta/FeMn/Pt stack (c)Triple repeat of Ta/FeMn/Pt stack.

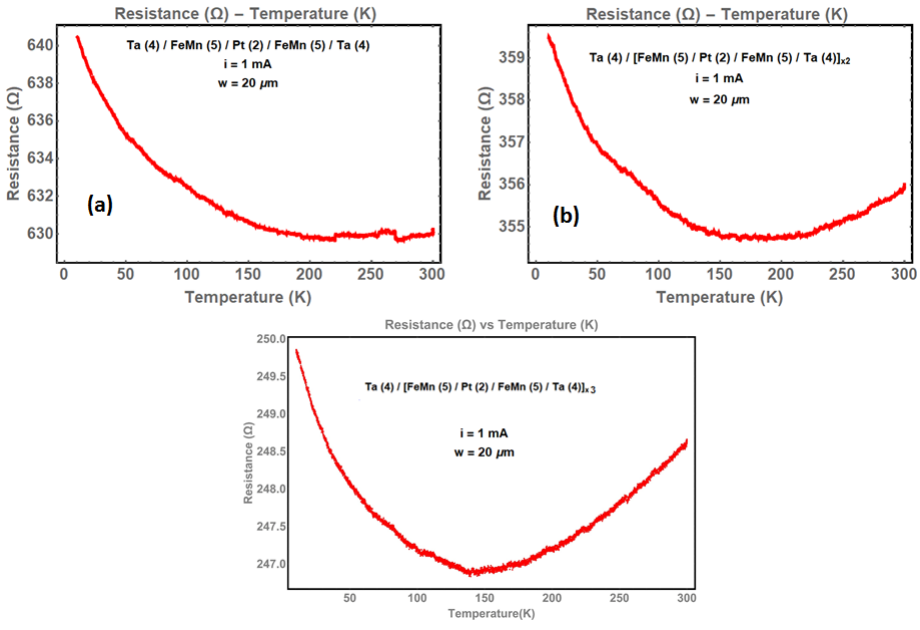

Figure 5.20. Temperature scan data from FeMn multi-stack samples.(a) Single repeat of Ta/FeMn/Pt stack (b) Double repeat Ta/FeMn/Pt stack (c) Triple repeat of Ta/FeMn/Pt stack.

5.3.2. $IrMn_4$ Multistack Experiments

We have studied the electroresistance behaviour of multistacks with $Ta/IrMn_4/Pt$ repeats. Similar to FeMn multistack experiments, increasing number of stacks made it more difficult to identify magnetic interactions. Additionally, SOC nature of $IrMn_4$ makes it even more comlicated to analyze the pure spin current generation and spin transfer through layers. As it can be seen in Figure 6.4, this multi-stack structure promises an extensive spin accumulation between layers and magnification of magnetization in each layer caused by SOT. However, similar reasons to FeMn devices, contrast in conductivities of layers makes it quite difficult to probe this enhancement.

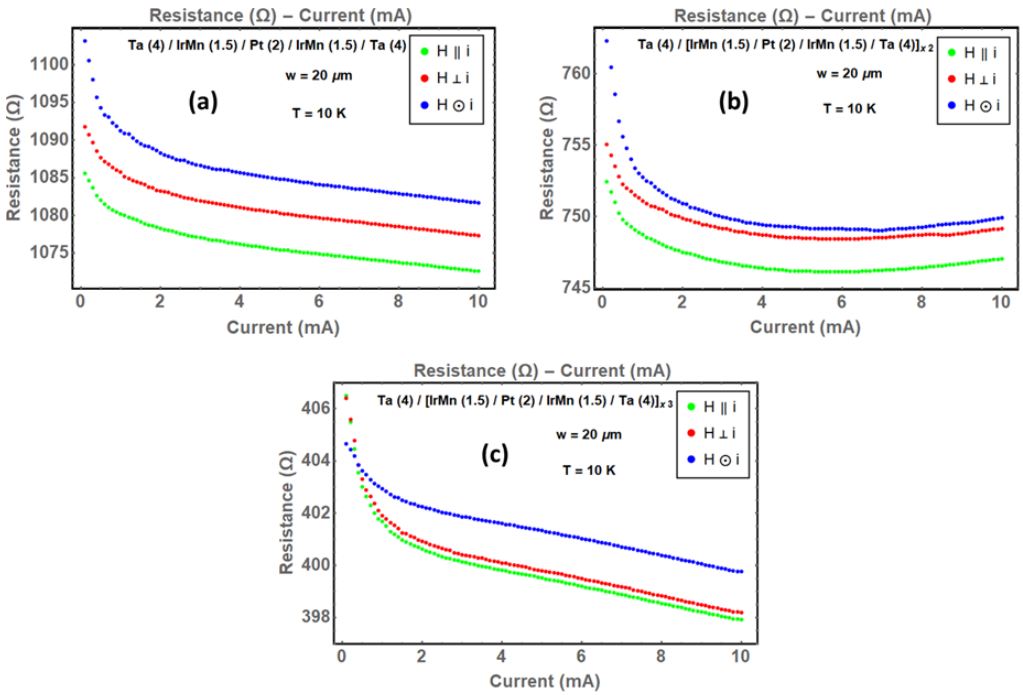

Figure 5.21. Current scan data from $IrMn_4$ multi-stack samples. (a) Single repeat of $Ta/IrMn_4/Pt$ stack (b) Double repeat of $Ta/IrMn_4/Pt$ stack (c)Triple repeat of$Ta/IrMn_4/Pt$ stack.

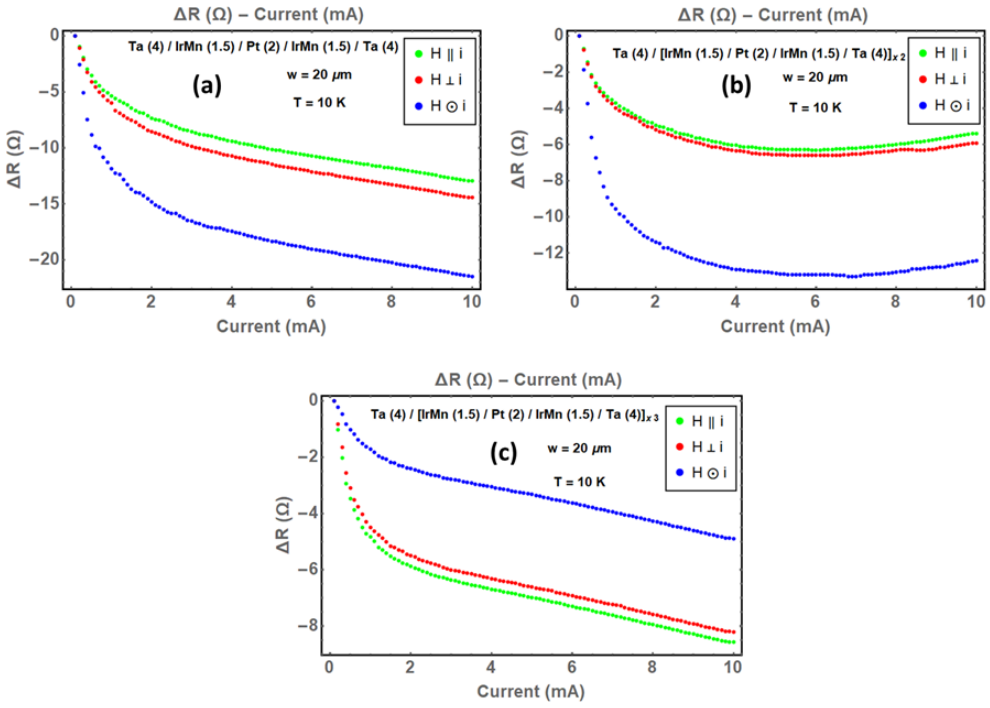

Figure 5.22. Current scan data fit from $IrMn_4$ multi-stack samples. (a) Single (b) Double (c) Triple repeat of Ta/$IrMn_4$/Pt stack.

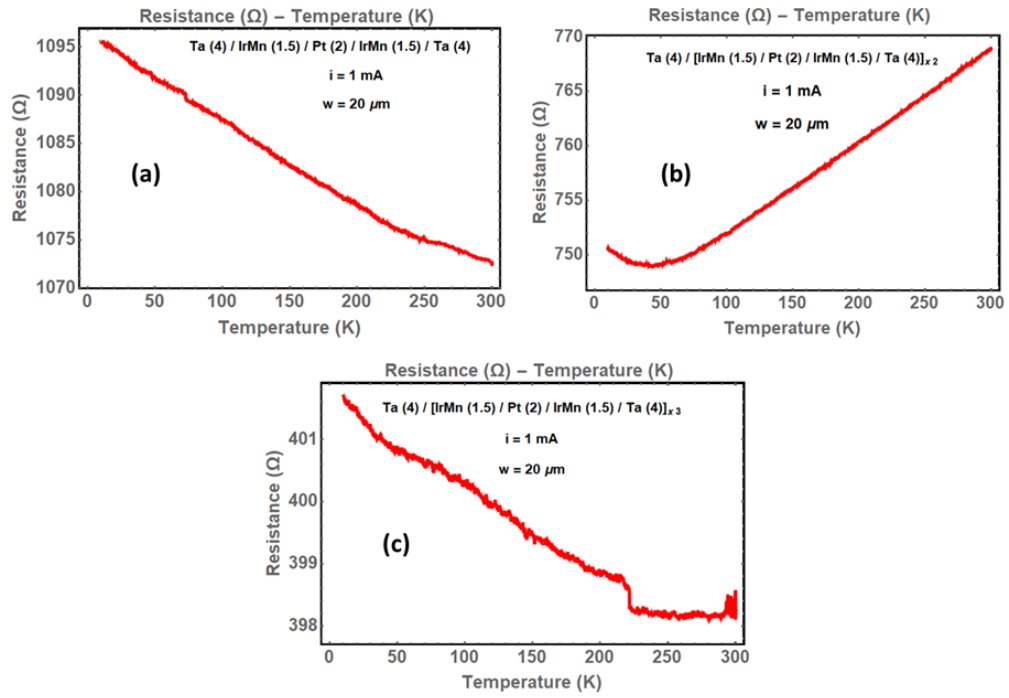

Figure 5.23. Temperature scan data from Ta/$IrMn_4$/Pt multi-stack samples.(a) Single (b) Double (c) Triple repeat of Ta/$IrMn_4$/Pt stack.

6. CONCLUSION AND DISCUSSION

After performing series of low temperature current scan and resistance versus temperature measurements, our data reveals that we have obtained strong signs of SOT influenced resistance change in our Ta(4)/FeMn(5) and Pt(2)/$IrMn_4$(1.5) bilayer samples, as evidenced by the changes in electroresistance behaviour. Other samples with thicker AFM layer thickness presumably have Néel temperatures greater than 400 K making our field cooling process not functional. On the other hand, our data suggest thinner layers do not yet have the proper exchange interaction set up for AFM behaviour.

Starting from FeMn(5) bilayer experiments, Figure 5.4e shows that Ta(4)/FeMn(5) sample first and third case behaviours overlap after the injected current reaches 6 mA. While a similar behaviour can be observed in Pt(2)/FeMn(5) (Figure 5.4b) sample after 2 mA, after 8 mA of current injection, the sample displays signs of irreversible sample and /or electrical contact damage as suggested by resistance jumps.

When the signs in SOT influence are investigated by including resistance versus temperature measurements for Ta(4)/FeMn(5) sample, it can be observed that from 10K to 300K resistance of sample drops around 100 ohms (Figure 5.4f). Same amount of resistance drop is achieved by a 7 mA current scan, with no signs of irreversible damage caused by heating effects(Figure 5.4e).

When it comes to Pt(2)/$IrMn_4$, in Figure 5.6b, it can be seen that rates of change in resistance values are quite consistent with previous findings [24], mentioned in Section 4.4. More specifically, rate of change in resistance of Pt(2)/$IrMn_4$(1.5) sample imply that Case I (green) and III (blue) act different from Case II (red) where change in resistance of Case II is obviously smaller than the other two. This result suggests that it may caused by the torque applied in cases where pure spin current is perpendicular to the AFM order induced by field cooling process. In order to make SOT characterization more reliable, we performed an additional current scan at the temperature value where the resistance of the sample gives a dip at 40 K (Figure 5.7b). Each data in Figure 5.8 is taken after regular field cooling process (400K to 10K). After reaching 10K with applied field, field is turned off and the sample is heated up to 40K.

Since SOT effect is more efficient at lower temperatures, for a measurement performed at 40 K one would expect to see less change in electro resistance compared to 10 K measurement. If this were purely due to Joule heating, one would expect to see the same dip value in resistance followed by a significant increase in resistance. To the contrary, the current scan (Figure 5.8) taken at 40 K, displays decreasing behaviour until 4 mA, followed by a slower increase compared to temperature scan. This evidence shows strong signs of SOT influenced change in electroresistance in sample Pt(2)/$IrMn_4$(1.5). As a result we have decided to use $IrMn_4$(1.5) as the base unit for further multilayer studies.

After bilayer structures, trilayer measurements were performed. Different pure spin current injection scenarios were investigated. 2D schematics of possible scenarios for combination of effects are given below (Figure 6.1 and 6.2). Here our aim is to investigate the effect of third layer added to bilayer structures. The mechanism shown in Figure 6.1 suggests that, selecting two HM layers which have spin Hall angles with opposite signs, at the bottom and the top of AFM layer, should add up the amount of magnetization induced by SOT (M_{SO}) and enhance the change in electroresistance. The results may vary depending on the choice of AFM layer, being FeMn(5) or $IrMn_4$(1.5), since the latter has an additional self-torque effect due to the presence of Ir.

When the layers at the top and the bottom have opposite signs of spin Hall angles as in Pt(2)/$IrMn_4$(1.5)/Ta(4) and Pt(2)/FeMn(5)/Ta(4) SOT effect is expected to be enhanced, where as when the layers at the top and the bottom have same sign in their spin Hall angles, it is expected to observe injection of pure spin current in opposite direction through the AFM layer, which will make the observed effect weaker.

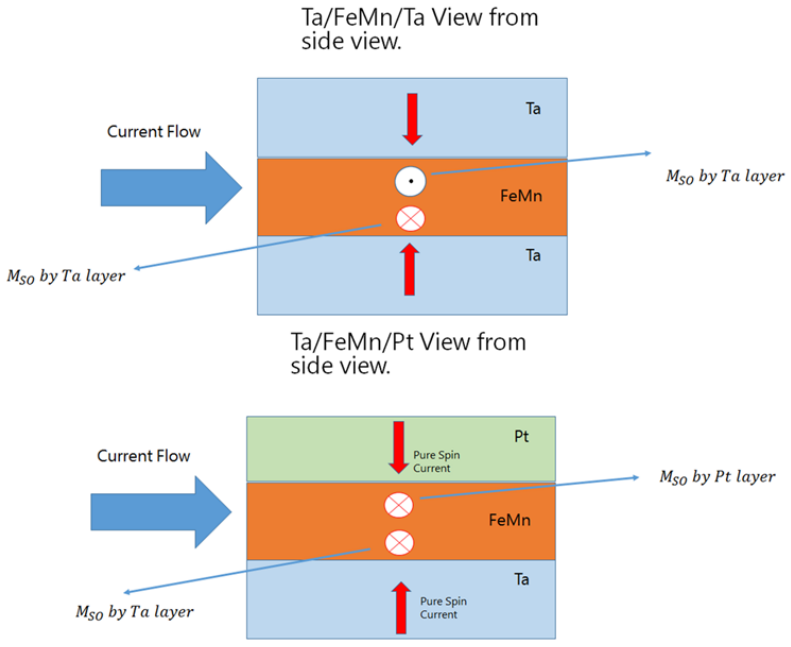

Figure 6.1. Expected effect on FeMn trilayer measurements.

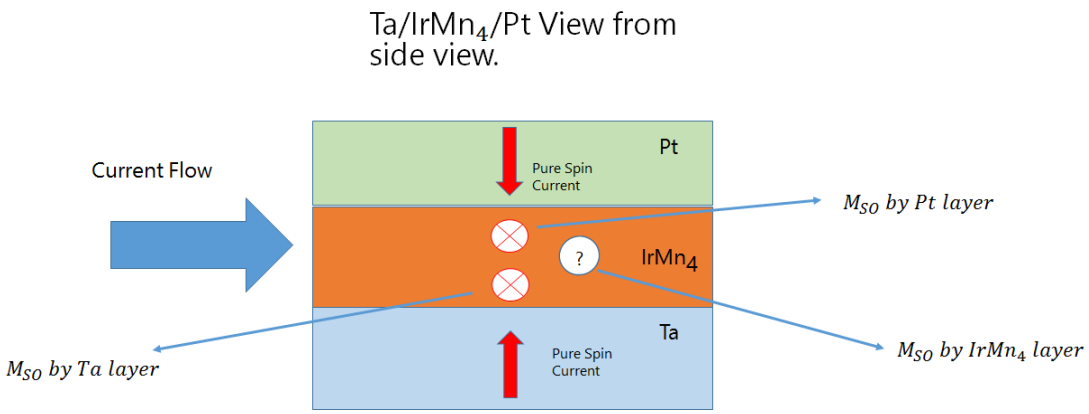

Figure 6.2. Expected effect on $IrMn_4$ trilayer measurements.

Very interesting result on Ta(4)/FeMn(5)/Ta(4) (Figure 5.13a) sandwich sample shows instead of canceling spin currents, there might be an interfacial effect that occurs symmetrically at interfaces. Trilayer measurements of given sample appears to be quite similar with bilayer measurement of Ta(4)/FeMn(5) while second case data seem to be changing less compared to other two cases. Amount of resistance drop decreased as expected, since all measurements were performed on Hall bars with same width, which is 20 microns. As expected, adding an additional HM layer will likely decrease the initial resistance, which makes detection of few ohms of change in resistance more difficult. Leaving the absolute resistance values aside, change in resistance behaviour in Ta(4)/FeMn(5)/Ta(4) sample fits right into SOT induced resistance change scenario and seems even more prominent than it's bilayer counterpart Ta(4)/FeMn(5).

Another important parameter to consider here is the spin diffusion length of AFM layer. For FeMn, previous study shows that estimated spin diffusion length is around 1-2 nm [38]. This implies that injected pure spin currents from both sides won't be penetrating through the whole layer. The behaviour of Ta(4)/FeMn(5)/Ta(4) can be interpreted as the combined effect of two Ta(4)/FeMn(5) structures acting independently. When it comes to $IrMn_4$ trilayer measurements, first experiment was performed on Ti/$IrMn_4$. Figure 5.15a suggests that the actual sample resistance is quite sensitive to the presence or absence of HM layers, giving this sample quite high resistance value (6 k). We can see in Figure 5.16a Case I and III act nearly the same, while Case II has a slightly lower rate of change. This behaviour is a direct proof to self-torque properties of AFM heavy metal $IrMn_4$ being significant.

Another interesting outcome of $IrMn_4$ trilayers is experiments of Pt(2)/$IrMn_4$/Pt(2) and Ta(4)/$IrMn_4$/Pt(2). Unlike other repetitive similarities, there is an interesting common behaviour in these two experiments. As you can see in Figure 5.16b and c, Cases II and III for both samples behave quite similar, while Case I for both of them has a way higher rate of resistance change. The fact that not only the rate of resistance change in Case I in both measurements, but also how Case II and III act alike is quite interesting.

When the current scan is compared to temperature scan, one should realize another interesting detail. When the Pt(2)/$IrMn_4$/Pt(2) sample is investigated, Figure 5.17b shows that the sample resistance acts proportional to increasing temperature.

When the current scan is performed at 10K, it is expected to heat the sample up and show signs of temperature dependent changes in resistance. If we compare this relationship for Pt(2)/$IrMn_4$/Pt(2), it can be easily seen that the drop in resistance during current scan is directly opposite to increasing temperature behaviour of the sample. It is not wrong to separate this effect from thermal boosts, however, the bigger picture is not completely compatible with SOT influence on electroresistance.

Ta(4)/$IrMn_4$/Pt(2) is the sample with the expectation of highest rate in change of electroresistance. Obvious reason for this is the combination of one positive (Pt) and one negative (Ta) spin Hall material (Figure 6.1). Even though the change in resistance values are not what we desire to see, it carries odd questions to be answered. Like Pt(2)/$IrMn_4$/Pt(2) sample, Case I stands separated from other two cases, where Case II and Case III are nearly have the same behaviour. Since the chronological order of the measurements starts from Case I and ends with Case III, it is quite unlikely that this type of behaviour to be an experimental coincidence.

Another important point is comparison with their resistance versus temperature behaviour. Where the sample Ta(4)/$IrMn_4$/Pt(2) has a decreasing resistance trend with increasing temperature, amount of resistance change is nearly same with Case II and Case III. If we look at the Case I data, it is three times larger than it's resistance change until room temperature. When the XRD data from Section 4.1.3 is reviewed, it can be seen that the interesting behaviour of change in the electroresistance in Ta(4)/$IrMn_4$/Pt(2) and Pt(2)/$IrMn_4$/Pt(2) can be directly related to crystal structure of $IrMn_4$. Deposition of $IrMn_4$ on Ta and Pt layers will give material a ¡111¿ textured orientation, which increases the magnetic anisotropy and make it more stable. This property may cause Néel temperature of AFM layer to increase over 400 K and make field cooling process fail.

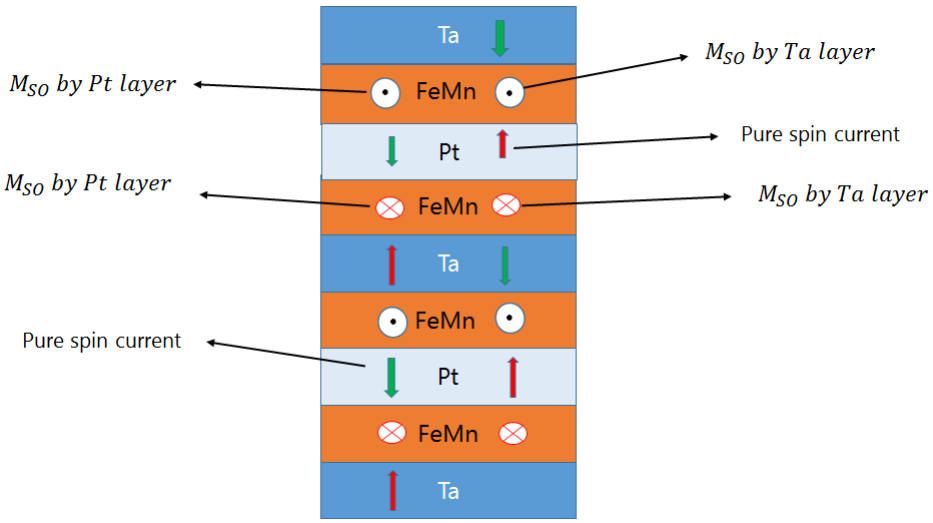

Figure 6.3. Expected effect on FeMn multistack measurements.

Final stage of the study is the multistack experiments. Common issue for both set of samples ($IrMn_4$ and FeMn) is reduced device resistance (hundreds of) values. Stack full of repetitive HM layers will cause resistance of the sample to drop remarkably, as expected. This effect makes detection of magnetic interactions very difficult. Expected mechanism for these experiments are given in Figure 6.3 and Figure 6.4.

When the current scan offset data from Figure 5.19 is considered for FeMn stacks, few ohms of differences between cases becomes hard to interpret. Especially when the highest stack data is reviewed, small hysteresis loops can be observed during current scan, indications of thermal damage on the sample. One thing to extract from combination of data from Figure 5.18 and 5.20, current scan experiments suggest that we can reach slightly lower resistance values than the resistance values at room temperature. Second and third stacks behave as metallic after passing 150 K, and behave as a semiconductor before heating up to 150 K due to the trade off between the individual FeMn layer and HM resistance versus temperature behaviours. Even though current scan doesn't show any sign of increasing resistance, by using current scan it is possible to achieve the lowest resistance value of temperature scan. Differences in trends in resistance versus temperature of before and after 150 K shows no similarity to the trends in current scan.

Apart from FeMn data, $IrMn_4$ measurements show interesting results. Similar to trilayer measurements, stack measurements separate one case from others. Trilayer stacks provided a similar approach for Case I behaviour, while stack measurements show a similar fashion for Case III. When Figure 5.22a and 5.22b is reviewed, trends shows the explained mechanism. Just like trilayer experiments, deposition of $IrMn_4$ on metallic surfaces has a strong influence on electroresistance measurements. Unlike others, third stack measurement can be directly related to change of PCB, first two cases acting same before changing PCB, than artifacts and insertion process of sample effect the sample and changes it's behaviour. Regarding these findings, samples with higher resistance (smaller Hall bar widths) should be studied well for the future applications.

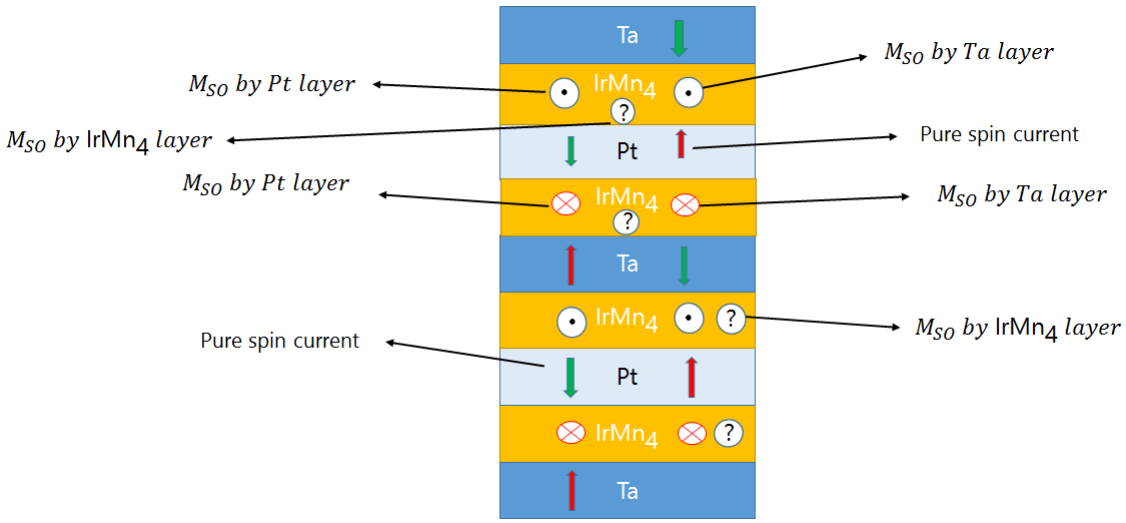

Figure 6.4. Expected effect on $IrMn_4$ multistack measurements.

We briefly explained our claims and comments from our experimental findings. While results shows some clear evidences at some point, there are also several conditions that may have an effect on the data, which needed to be pointed out while reviewing the results. These conditions are the down sides and questionable factors that may effect on our results.

First condition we need to consider is the current density distribution. Previous study shows [39] SOT effect is directly proportional to the current density. In our heterostructures, bilayer experiments for example, one HM layer with very low resistance is combined with an AFM material. Materials we use as HM layers (Ta, Pt) create a great difference in terms of resistance, as it can be understood with the schematic

circuitry (Figure 6.5). When the current is injected to sample, HM layer recruits the majority of the current with a very high density. Even though it is a promising condition for generating high density spin current, it also means that the current injected into AFM layer will be too low for a reliable measurement of resistance change due to AFM layer alone. This condition makes measuring any kind of resistance change in AFM layers hard to detect. Any kind of changes in resistance measurements (magnetic, thermal) will be strongly dominated by HM layers, especially Pt. Resistivity experiments show how each layer's resistivity behaviour behave for two thicknesses (10 and 50 nm). Thickness dependent resistivity measurements of Pt shows how Pt layer effectively acts as a short when combined with other materials. When these parameters are taken into account, a simple circuitry calculation for one set of samples shows nearly % 95 of the current in bi-layer experiments is passing through Pt layer. In this case, contribution of AFM layer to electroresistance measurements may remain insufficient for valuable considerations.

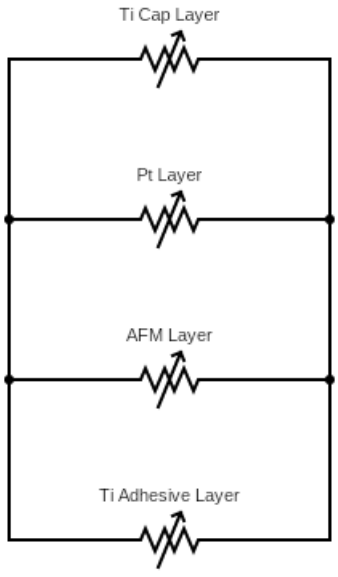

Figure 6.5. Circuitry scheme of a bilayer structure. Each element of circuit is given as variable resistances, since by thermal and magnetic effects alter the resistance values for each one.

For comparison, our resistance versus temperature measurements are performed by applying 1 mA constant current for obtaining reliable resistance values. According to our calculation, when a 10 mA current scan performed on a bilayer structure, % 2.4 of the current, which results as 0.24 mA of current is injected to AFM layer, an amount of current we consider as " dead current" (0.5 mA) in our current scan experiments. As one of the important findings belong to the sample Pt(2)/$IrMn_4$(1.5), an example calculation for current density analysis is performed and values are given below.

Table 6.1. Percentage of Injected current into each layer.

Layer	Thickness (nm)	Percentage (%)
Ti Cap Layer	3	2.91
Pt Layer	2	94.56
$IrMn_4$	1.5	2.02
Ti Adhesion Layer	0.5	0.48

Reliability of our experimental data is not only affected by current density but also the electrical connection deformations of samples as well (Figure 6.6). Characterization of SOT requires a dense process where each sample is subjected to many rounds of transport measurements and field cooling processes, resulting in a possible wear out. As it is mentioned in Section 4.4, each change in initial resistance values holds a crucial place for detection mechanism. Investigating signs of SOT with our experiment setup relies on changes in order of few ohms, due to same factor explained in current density analysis. Thus, chronological order of current scan data of each case has a crucial effect in initial resistance values. This makes a lot of sense , since each transport measurement, field cooling protocol, temperature dependent measurement and re-bonding process for out-of-plane measurements disturb the electrical contacts and connections which may slightly alter the initial resistance values.

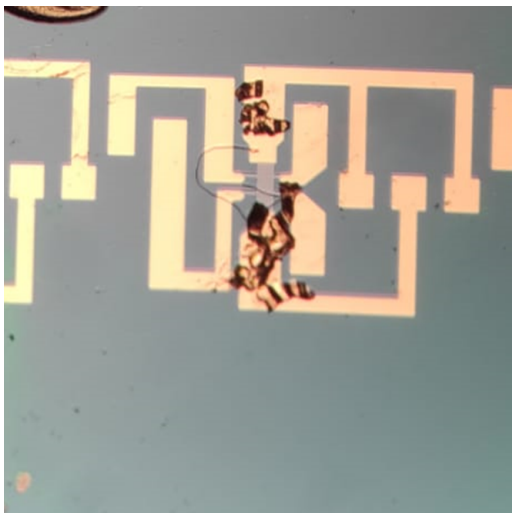

Figure 6.6. Effect of contact damages on a sample after two wirebonding process in a row.

In our study, crucial part of the data we get depends heavily on field cooling protocols. If the field cooling procedure for each sample doesn't work properly, magnetic orientation won't be created in AFM layer and manipulation effort will fail. There are few main reasons that may cause field cooling procedure to fail. There may be inhomogenieties in the distribution of anisotropy causing local variation of Néel temperatures from grain to grain. Furthermore, impurities or edge domains may have an additional effect leading to changes in the local response to thermal effects.

Thickness of AFM layer is another important parameter for reliability of field cooling process. We already performed magnetic characterization on AFM materials depending on their thickness values. However, in some cases if the layer thickness is above an ideal value for optimized exchange interaction , field cooling process may not be enough for paramagnetic phase, since the more thickness brings more interactions hence more energy to manipulate moments. On the other hand, if the AFM layer is too thin, it is very unlikely to form a perfect AFM structure due to lack of exchange interactions. When the required thickness was achieved with 1.5 nm, SOT effect becomes visible. Influence of field cooling on this sample was investigated further, performing two low temperature current scans. Blue data shows the sample cooled from 400 K to 10 K without an external magnetic field. Red data shows the current scan data of the same sample, field cooled under 1 T magnetic field. As can be seen from Figure 6.7, influence of field cooling can be easily observed in our SOT prospect device.

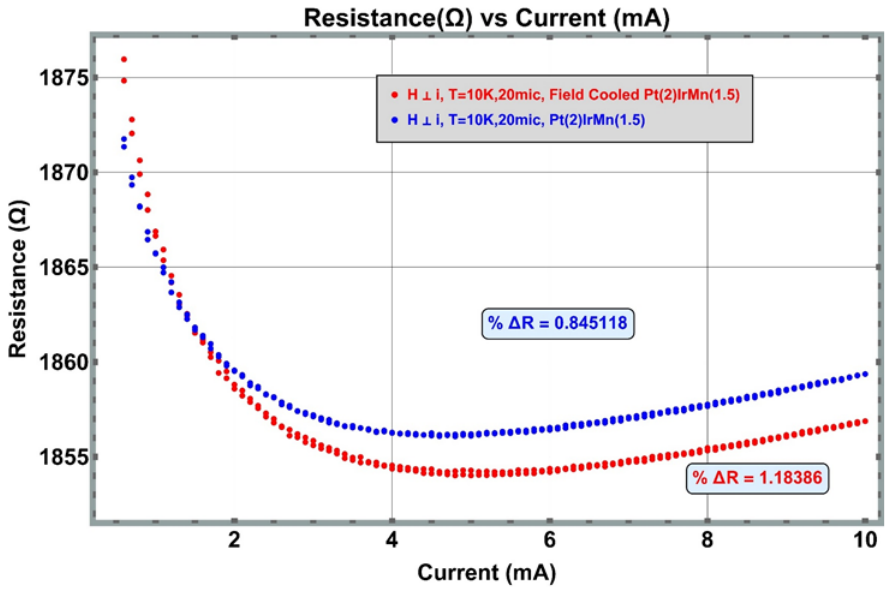

Figure 6.7. An experiment data to test the effectiveness of field cooling procedure. Red data represents the 1 T field cooled sample from second case measurement of Pt(2)/$IrMn_4$(1.5) and blue data represents the current scan after cooling the same sample without a magnetic field.

As the conclusion, our study shows, using electroresistance data obtained by a current scan, strong signs of SOT is obtained in Pt(2)/$IrMn_4$(1.5) and Ta(4)/FeMn(5) samples. As the possible reasons explained above, it is even tougher to identify a magnetic interaction or enhancement of SOT via electroresistance measurements. Considering the current distribution in individual layers will be significantly changed with increasing number of stacks of layers, it will be even more difficult to analyze these results. Further investigations will be performed such as, four-probe measurements for detection of change in magnetization, shifting the order of cases for understanding the effect of experimental artifacts, replacing $IrMn_4$ with single crystal $IrMn_3$ in order to investigate effect of crystal orientation and optimization of Hall bar width for higher order of repeats with taller stacks.

REFERENCES

1. Bhatti, S., R. Sbiaa, A. Hirohata, H. Ohno, S. Fukami and S. Piramanayagam, "Spintronics Based Random Access Memory: A Review", *Materials Today*, Vol. 20, No. 9, pp. 530–548, 2017.

2. Baibich, M. N., J. M. Broto, A. Fert, F. N. Van Dau, F. Petroff, P. Etienne, G. Creuzet, A. Friederich and J. Chazelas, "Giant Magnetoresistance of (001)Fe/(001)Cr Magnetic Superlattices", *Physical Review Letters*, Vol. 61, pp. 2472–2475, 1988.

3. Binasch, G., P. Grünberg, F. Saurenbach and W. Zinn, "Enhanced Magnetoresistance Iin Layered Magnetic Structures with Antiferromagnetic Interlayer Exchange", *Physical Review B*, Vol. 39, pp. 4828–4830, 1989.

4. Hirohata, A., K. Yamada, Y. Nakatani, I.-L. Prejbeanu, B. Diény, P. Pirro and B. Hillebrands, "Review on Spintronics: Principles and Device Applications", *Journal of Magnetism and Magnetic Materials*, Vol. 509, p. 166711, 2020.

5. Ralph, D. and M. Stiles, "Spin Transfer Torques", *Journal of Magnetism and Magnetic Materials*, Vol. 320, No. 7, pp. 1190–1216, 2008.

6. Park, B. G., J. Wunderlich, X. Martí, V. Holý, Y. Kurosaki, M. Yamada, H. Yamamoto, A. Nishide, J. Hayakawa, H. Takahashi, A. B. Shick and T. Jungwirth, "A Spin-Valve-Like Magnetoresistance of an Antiferromagnet-Based Tunnel Junction", *Nature Materials*, Vol. 10, No. 5, pp. 347–351, 2011.

7. Kim, J., A. Chen, B. Behin-Aein, S. Kumar, J.-P. Wang and C. H. Kim, "A Technology-agnostic MTJ SPICE Model with User-defined Dimensions for STT-MRAM Scalability Studies", *2015 IEEE Custom Integrated Circuits Conference (CICC), San Jose, California, USA*, pp. 1–4, 2015.

8. Yakata, S., Y. Ando, T. Miyazaki and S. Mizukami, "Temperature Dependences of Spin-Diffusion Lengths of Cu and Ru Layers", *Japanese Journal of Applied Physics*, Vol. 45, No. 5A, pp. 3892–3895, 2006.

9. Shao, Q., P. Li, L. Liu, H. Yang, S. Fukami, A. Razavi, H. Wu, K. Wang, F. Freimuth, Y. Mokrousov, M. D. Stiles, S. Emori, A. Hoffmann, J. Akerman, K. Roy, J.-P. Wang, S.-H. Yang, K. Garello and W. Zhang, "Roadmap of Spin–Orbit Torques", *IEEE Transactions on Magnetics*, Vol. 57, No. 7, pp. 1–39, 2021.

10. Néel, L., "Antiferromagnetism and Ferrimagnetism", *Proceedings of the Physical Society. Section A*, Vol. 65, No. 11, pp. 869–885, 1952.

11. McCaig, M., *Permanent Magnets in Theory and Practice.*, Pentech press., 1977.

12. Shull, C. G. and J. S. Smart, "Detection of Antiferromagnetism by Neutron Diffraction", *Physical Review Letters*, Vol. 76, pp. 1256–1257, 1949.

13. Spaldin, N. A., *Antiferromagnetism*, p. 96–112, Cambridge University Press, 2 edn., 2010.

14. Fina, I., X. Marti, D. Yi, J. Liu, J. H. Chu, C. Rayan-Serrao, S. Suresha, A. B. Shick, J. Železný, T. Jungwirth, J. Fontcuberta and R. Ramesh, "Anisotropic Magnetoresistance in an Antiferromagnetic Semiconductor", *Nature Communications*, Vol. 5, No. 1, 2014.

15. Marti, X., I. Fina, C. Frontera, J. Liu, P. Wadley, Q. He, R. J. Paull, J. D. Clarkson, J. Kudrnovský, I. Turek, J. Kuneš, D. Yi, J.-H. Chu, C. T. Nelson, L. You, E. Arenholz, S. Salahuddin, J. Fontcuberta, T. Jungwirth and R. Ramesh, "Room-temperature Antiferromagnetic Memory Resistor", *Nature Materials*, Vol. 13, No. 4, pp. 367–374, 2014.

16. Mendes, J. B. S., R. O. Cunha, O. Alves Santos, P. R. T. Ribeiro, F. L. A. Machado, R. L. Rodríguez-Suárez, A. Azevedo and S. M. Rezende, "Large Inverse Spin Hall Effect in the Antiferromagnetic Metal $Ir_{20}Mn_{80}$", *Physical Review Letters B*, Vol. 89, p. 140406, 2014.

17. Brataas, A. and K. M. D. Hals, "Spin–Orbit Torques in Action", *Nature Nanotechnology*, Vol. 9, No. 2, pp. 86–88, 2014.

18. Li, Y., K. W. Edmonds, X. Liu, H. Zheng and K. Wang, "Manipulation of Magnetization by Spin-Orbit Torque", *Advanced Quantum Technologies*, Vol. 2, No. 1-2, p. 1800052, 2018.

19. Ramaswamy, R., J. M. Lee, K. Cai and H. Yang, "Recent Advances in Spin-Orbit Torques: Moving Towards Device Applications", *Applied Physics Reviews*, Vol. 5, No. 3, p. 031107, 2018.

20. Browne, A. J., A. Krajewska and A. S. Gibbs, "Quantum Materials with Strong Spin–Orbit Coupling: Challenges and Opportunities for Materials Chemists", *Journal of Material Chemistry C*, Vol. 9, pp. 11640–11654, 2021.

21. Han, J. and L. Liu, "Topological Insulators for Efficient Spin–Orbit Torques", *APL Materials*, Vol. 9, No. 6, p. 060901, 2021.

22. Amin, V. P. and M. D. Stiles, "Spin Transport at Interfaces with Spin-Orbit Coupling: Phenomenology", *Physical Review B*, Vol. 94, No. 10, 2016.

23. Wadley, P., B. Howells, J. Železný, C. Andrews, V. Hills, R. P. Campion, V. Novák, K. Olejník, F. Maccherozzi, S. S. Dhesi, S. Y. Martin, T. Wagner, J. Wunderlich, F. Freimuth, Y. Mokrousov, J. Kuneš, J. S. Chauhan, M. J. Grzybowski, A. W. Rushforth, K. W. Edmonds, B. L. Gallagher and T. Jungwirth, "Electrical Switching of an Antiferromagnet", *Science*, Vol. 351, No. 6273, pp. 587–590, 2016.

24. Han, J., Y. Wang, F. Pan and C. Song, "Spin-Hall-Effect-Assisted Electroresistance in Antiferromagnets via 10^5 A/cm2 dc Current", *Scientific Reports*, Vol. 6, 2016.

25. Dyakonov, M. and V. Perel, "Current-Induced Spin Orientation of Electrons in Semiconductors", *Physics Letters A*, Vol. 35, No. 6, pp. 459–460, 1971.

26. Valenzuela, S. O. and M. Tinkham, "Direct Electronic Measurement of the Spin Hall Effect", *Nature*, Vol. 442, No. 7099, pp. 176–179, 2006.

27. Niimi, Y. and Y. Otani, "Reciprocal Spin Hall Effects in Conductors with Strong Spin–Orbit Coupling: A Review", *Reports on Progress in Physics*, Vol. 78, No. 12, p. 124501, 2015.

28. Vila, L., T. Kimura and Y. Otani, "Evolution of the Spin Hall Effect in Pt Nanowires: Size and Temperature Effects", *Physical Review Letters*, Vol. 99, p. 226604, 2007.

29. Mambakkam, S. V. and S. Law, "Fabrication of Topological Insulator Nanostructures", *Journal of Vacuum Science & Technology B*, Vol. 38, No. 5, p. 055001, 2020.

30. Moumen, A., G. C. W. Kumarage and E. Comini, "P-Type Metal Oxide Semiconductor Thin Films: Synthesis and Chemical Sensor Applications", *Sensors*, Vol. 22, No. 4, 2022.

31. "Evaporator Working Principle", https://epsc.wustl.edu/imse/, accessed at 2022.

32. Paar, A., "XRD Working Principle", https://wiki.anton-paar.com/tr-tr/x-isini-kirilmasi-xrd/, accessed at 2022.

33. Zhang, W., W. Han, S.-H. Yang, Y. Sun, Y. Zhang, B. Yan and S. S. P. Parkin, "Giant Facet-dependent Spin-Orbit Torque and Spin Hall Conductivity in the Triangular Antiferromagnet $IrMn_3$", *Science Advances*, Vol. 2, No. 9, p. e1600759, 2016.

34. Radu, F. and H. Zabel, "Exchange Bias Effect of Ferro-/Antiferromagnetic Heterostructures", *Springer Tracts in Modern Physics*, pp. 97–184, Springer Berlin Heidelberg, 2008.

35. Wang, Y., P. Deorani, X. Qiu, J. H. Kwon and H. Yang, "Determination of Intrinsic Spin Hall Angle in Pt", *Applied Physics Letters*, Vol. 105, No. 15, p. 152412, 2014.

36. Tshitoyan, V., P. Wadley, M. Wang, A. W. Rushforth and A. J. Ferguson, "Negative Spin-Hall Angle and Anisotropic Spin-Orbit Torques in Epitaxial IrMn", *arXiv*, 2018.

37. Yu, R., B. F. Miao, L. Sun, Q. Liu, J. Du, P. Omelchenko, B. Heinrich, M. Wu and H. F. Ding, "Determination of Spin Hall Angle and Spin Diffusion Length in β-Phase-Dominated Tantalum", *Physical Review Materials*, Vol. 2, p. 074406,

2018.

38. Zhang, W., M. B. Jungfleisch, W. Jiang, J. E. Pearson, A. Hoffmann, F. Freimuth and Y. Mokrousov, "Spin Hall Effects in Metallic Antiferromagnets", *Physical Review Letters*, Vol. 113, p. 196602, 2014.

39. Meng, K., J. Miao, X. Xu, Y. Wu, J. Xiao, J. Zhao and Y. Jiang, "Modulated Switching Current Density and Spin-Orbit Torques in MnGa/Ta Films with Inserting Ferromagnetic Layers", *Scientific Reports*, Vol. 6, No. 1, p. 38375, 2016.